NOVA SCHOOL OF SCIENCE & TECHNOLOGY

DEPARTMENT OF COMPUTER SCIENCE

INÊS CARDOSO LEITÃO BARATA DE OLIVEIRA

Bachelor in ⟨Design e Multimédia⟩

REMOTE SENSING FOR LAND USE/LAND COVER MAPPING IN ALMADA

MASTER IN ANALYSIS AND ENGINEERING OF BIG DATA

NOVA University Lisbon
⟨July⟩, ⟨2022⟩

DEPARTMENT OF
COMPUTER SCIENCE

REMOTE SENSING FOR LAND USE/LAND COVER MAPPING IN ALMADA

INÊS CARDOSO LEITÃO BARATA DE OLIVEIRA

Bachelor in ⟨Design e Multimédia⟩

Adviser: Carlos Augusto Isaac Piló Viegas Damásio
Associate Professor, NOVA University Lisbon

Co-adviser: João Carlos Gomes Moura Pires
Associate Professor, NOVA University Lisbon

Examination Committee:

Chair: Paula Alexandra da Costa Amaral
Associate Professor, NOVA School of Science and Technology | FCT NOVA

Rapporteur: Ana Cláudia Moreira Teodoro
Associate Professor with Habilitation, Faculty of Sciences of the University of Porto | FCUP

Adviser: Carlos Augusto Isaac Piló Viegas Damásio
Associate Professor, NOVA School of Science and Technology | FCT NOVA

MASTER IN ANALYSIS AND ENGINEERING OF BIG DATA

NOVA University Lisbon
⟨July⟩, ⟨2022⟩

Remote sensing for Land use/Land cover mapping in Almada

To my family.

Acknowledgements

First, I would like to express my gratitude to my dissertation supervisors, Professor Carlos Viegas Damásio and Professor João Moura Pires, who had an essential role in the development of this work, providing guidance, feedback and support during the whole process.

I would also like to extend a thank you to the Almada city council for providing the opportunity for this dissertation, and for their availability to answer all my questions.

Thanks to my lifelong friends, Bruno, Helena, Pedro and Mariana, for all these years of amazing memories and for always being there. Thank you to Beatriz and Francisca, for the frequent check-ins, unwavering support and true friendship.

A special thank you to António for all the help and patience, for the pep talks, and for being a constant source of happiness and encouragement.

Finally, I would like to acknowledge and thank my parents for making me who I am and providing me with all the tools to excel in life, along with the assurance that they will be there to catch me if I stumble. A huge thank you as well to my brother, José, for his continuous support and late night conversations, often accompanied by pancakes.

Abstract

Monitoring land use and land cover is an extremely important task which, if properly carried out, can assist in decision making about urban and territorial planning, thus providing an improvement in the citizens' quality of life. In Portugal, and more specifically in the Almada municipality , the main tool used in this task is Carta de Ocupação de Solo (COS), a map which represents 83 classes of land use and land cover. Despite its usefulness, COS has certain limitations, such as low spatial resolution, due to the minimum mapping unit of 1 hectare, and low temporal resolution, as it is developed through the analysis of orthophotos and released every 3 to 5 years. These constraints lead to a map which is not adequate to continuously track land-use and land-cover changes, especially with the increasingly fast pace of urbanization.

This research work investigated the application of machine learning classification algorithms with Sentinel-1 and Sentinel-2 imagery, and derived products, to LULC mapping in Almada. As such, maps were developed for 2018 using the two most common approaches to LULC classification: pixel-based (PBIA) and object-based (OBIA). Multiple combinations of satellite data and derived products, as well as two classifiers were tested for each approach. A comparison of two methods of collecting ground truth data, manual and semi-automatic, was also produced.

The best results were obtained in the PBIA approach, using the manually collected ground truth and the Extreme Gradient Boosting (XGBoost) classifier with the combination of Sentinel-1 and Sentinel-2 imagery and textural features obtained through Sentinel-2 data. The classification model obtained a kappa score of 0.994, and produced an accurate LULC map, which has some limitations in separating **Agriculture** and **Other Vegetation**, but is able to identify with great precision **Artificial Territories**, **Forests** and **Bare and sparsely vegetated areas**.

Keywords: Remote sensing, Sentinel-1, Sentinel-2, Machine Learning,
LULC Mapping, Object-based LULC Classification, Pixel-based LULC Classification

Resumo

A monitorização da utilização e ocupação do solo (LULC) é uma tarefa de extrema importância que, sendo adequadamente realizada, pode auxiliar na tomada de decisões de ordenamento do território, providenciando assim uma melhoria na qualidade de vida dos cidadãos. Em Portugal, e mais especificamente no concelho de Almada, a principal ferramenta utilizada nesta tarefa é a Carta de Uso e Ocupação do Solo (COS), um mapa que divide o solo em 83 classes. Embora notavelmente útil, a COS possui determinadas limitações, entre as quais baixa resolução espacial, devido á unidade mínima cartográfica de 1 hectare, e baixa resolução espacial, sendo desenvolvida através da análise de ortofotos e disponibilizada a cada 3 a 5 anos. Estas limitações levam a que este mapa não seja adequado para a monitorização contínua de alterações ao nível da utilização e ocupação do solo, especialmente com o ritmo cada vez mais acelerado do crescimento urbano.

Este trabalho de investigação estudou a aplicação de algoritmos de classificação de *machine learning* com imagens de Sentinel-1 e Sentinel-2 e produtos derivados, para a cartografia de uso e ocupação de solo em Almada. Assim, foram desenvolvidos mapas para o ano 2018 explorando duas metodologias frequentemente utilizadas em problemas de classificação de uso e ocupação do solo: baseada em píxeis (PBIA) e baseada em objetos (OBIA). Para cada abordagem foram testadas várias combinações de imagens de satélite e produtos derivados, assim como dois classificadores automáticos. Foi também produzida uma comparação entre dois tipos de ground truth: obtida manualmente, e de uma forma semi-automática.

Os melhores resultados foram obtidos na abordagem baseada em pixeis, utilizando a ground truth manual e o classificador Extreme Gradient Boosting (XGBoost) com a combinação de imagens de Sentinel-1, Sentinel-2 e atributos de textura calculados através de imagens de Sentinel-2. Este modelo de classificação obteve um coeficiente kappa de 0.994 e produziu um mapa de uso e ocupação do solo com boa precisão e que, embora tenha algumas limitações ao nível de separação das classes **2. Agricultura** e **3. Outra vegetação**, identifica com exatidão as classes **Territórios Artificializados**, **Florestas** e **Espaços descobertos ou com pouca vegetação**.

Palavras-chave: Deteção remota, Sentinel-1, Sentinel-2, Aprendizagem Automática, Cartografia de Utilização e Ocupação do Solo,
Classificação baseada em objetos, Classificação baseada em pixeis

Contents

List of Figures

List of Tables

Acronyms

BUI Built-Up Index 12, 37

CLC CORINE Land Cover 1, 60

CNN Convolutional Neural Networks 24

COS Carta de Ocupação de Solo xiii, xiv, xv, xvii, 2, 3, 4, 26, 28, 29, 30, 31, 39, 42, 48, 50, 51, 58, 59, 60, 61, 62, 63, 64, 65, 66, 67, 69, 71, 72, 73, 84, 85, 86, 87, 88, 89, 90, 91, 92, 97, 99, 100, 101

COSsim COS simplificada xiii, xiv, xv, xvii, 4, 30, 31, 48, 50, 51, 60, 67, 68, 69, 70, 71, 72, 73, 84, 92, 93, 94, 95, 96, 97, 100, 101

DEM Digital Elevation Model 16

DGT Direção Geral do Território 2, 28, 30, 31, 101

EEA European Environment Agency 2

GBM Gradient Boosting Machines 21

GEE Google Earth Engine 32, 33, 34, 35, 36, 37

GIS Geographic Information System 19, 32

GLCM Gray-Level Co-Occurence Matrix 13, 15, 17, 22, 24, 37, 38

GS Global Score 23, 24

IFAP Instituto de Financiamento da Agricultura e Pescas, I.P 28

kNN k-Nearest Neighbor 6, 15, 16, 17, 18

LULC Land Use Land Cover 1, 2, 3, 4, 6, 9, 10, 13, 15, 16, 17, 18, 19, 20, 21, 22, 24, 26, 28, 30, 31, 34, 48, 50, 72, 74, 97, 98, 99, 100, 101

MI Moran's Index 23, 24, 45, 75, 97
MMU Minimum Mapping Unit 2, 31, 39
MSS Mean Shift Segmentation 10, 74

NASA National Aeronautics and Space Administration 2
NDBI Normalized Built-Up Index 12, 37
NDVI Normalized Difference Vegetation Index 12, 16, 17, 37
NDWI Normalized Difference Water Index 17

OA Overall Accuracy 10, 16, 17, 18, 19, 20
OBIA Object-Based Image Analysis 4, 10, 15, 18, 20, 21, 22, 24, 26, 44, 45, 48, 97, 98, 99, 100
OTB Orfeo ToolBox 10, 32, 37, 38, 44

PBIA Pixel-Based Image Analysis 4, 15, 18, 21, 26, 43, 48, 99, 100
PCA Principal Component Analysis 22, 37, 45

RF Random Forest xvi, xvii, 4, 6, 7, 8, 15, 16, 17, 18, 21, 24, 47, 51, 53, 54, 55, 56, 60, 79, 81, 98, 99, 100

SAR Synthetic Aperture Radar 11, 17
SAVI Soil Adjusted Vegetation Index 17
SVM Support Vector Machine 6, 15, 16, 17, 18, 19, 21, 24

WV Area-Weighted Variance 23, 24, 45, 75, 97

XGB XGBoost xvi, xvii, 4, 7, 8, 15, 21, 24, 47, 51, 52, 53, 55, 56, 57, 58, 60, 72, 79, 80, 81, 82, 83, 84, 98, 99, 100

1

Introduction

Having land cover and land use information is essential for multiple spatial planning decisions made by local and national administration, that can greatly affect the citizens' quality of life [43]. In recent years, several earth observation satellites have been launched that liberalized the access to data: initiatives like the Copernicus Programme provide remotely sensed data free of charge, at the push of a button. Consequently, the monitoring of the Earth's surface has been transformed, with the automatic generation of Land Use Land Cover (LULC) maps being one of the most active research topics in remote sensing applications [58]. Different methods and algorithms have been proposed and evaluated on regions with vastly different characteristics, obtaining varied degrees of accuracy.

1.1 Context

1.1.1 Land Use Land Cover mapping

Even though the expressions land use and land cover are often fused together as LULC, it is critical to define each one separately, as they have distinct meanings. While land cover refers to the physical cover of the surface of the ground, be it natural or man-made (buildings, forest, water...), land use relates to the actual application of the land (agriculture, recreational...). It is worth noting that a specific class of land cover can have various land uses, and vice-versa.

The use of the terms together as LULC is usually in the context of LULC maps. These maps contain spatial information on the coverage or use of the ground, and usually contain classes which distinguish elements such artificial structures, agriculture, natural elements and water.

Monitoring land use and land cover through LULC maps greatly assists in decision-making at the local and national administration levels, as it provides valuable insights to build strategies for managing natural resources and environmental changes, as well as urban growth [40, 70].

A LULC map worthy of mention is CORINE Land Cover (CLC)[1]. CLC is an european

[1] https://land.copernicus.eu/pan-european/corine-land-cover, Accessed on 2022-02-10

project, initially launched by the European Comission, now taken over by the European Environment Agency (EEA). This project is implemented by national teams, with most countries producing maps by visual interpretation of high resolution satellite imagery and a few through the application of semi-automatic solutions. The Minimum Mapping Unit (MMU) is 25 hectare (250000 m^2) and it is composed of 44 different classes, with three hierarquical levels. The first version is dated from 1990, and there are four subsequent updates from 2000, 2006, 2012, and 2018.

1.1.2 Remote sensing

In the most basic sense, remote sensing pertains to the gathering of information at a distance. This information is collected through the entire electromagnetic spectrum [2], about objects at the surface of the Earth by use of sensors based on satellites, manned aircrafts or unmanned aerial vehicles.

This dissertation will focus on remote sensing through the use of satellites, specifically Sentinel-1 and Sentinel-2. Initiatives like the European Commission's Copernicus Programme and the Landsat program, jointly managed by National Aeronautics and Space Administration (NASA) and the U.S. Geological Survey, have led to a democratization of satellite data, making it available to everyone free of cost. This fact makes the study and advancement of techniques that employ these resources extremely important. Obtaining data from other sources is often expensive and laborious, which can prevent the evolution of areas in which remote sensing can be applied.

Satellite data has facilitated LULC monitoring by providing data with increasingly higher spatial resolutions and frequencies, over large areas [58], and has been used for a myriad of applications such as urban planning [23], forest and agricultural monitoring [4], and disaster management of earthquakes [36] or volcanic eruptions [30].

1.2 Motivation

Almada, represented in Figure 1.1, is a Portuguese municipality located in the district of Setúbal, with 174,030 inhabitants (as of 2011)[2] and an area of approximately 70 km^2. In Portugal, and consequently in the city of Almada, the main LULC map utilized is COS.

COS is a national document developed by the Direção Geral do Território (DGT), produced through the analysis of aerial photographs, and readily available to the public. It consists of a polygon map, in which each unit is classified as one of 83 classes, organized into an hierarchical system of four levels. The most recent map is from 2018, with previous versions from 1995, 2007, 2010 and 2015. One especially important characteristic of COS is the MMU of 1 hectare (10000 m^2), which defines the minimum area that an object must have in order to be identified. Smaller elements are subjected to a series of

[2] https://www.m-almada.pt/, Accessed on 2022-02-10

Figure 1.1: Sentinel-2 image of the Almada municipality

generalization rules, which often results in inaccuracies. Additional information on COS 2018 technical specifications can be found in [20].

Analyzing the characteristics and limitations of COS, it is possible to perceive two domains in which the LULC mapping of Almada could be improved: temporal and spatial resolution. A map with higher spatial resolution would lead to a better delineation of objects on the ground, such as small isolated structures or small areas of vegetation surrounded by urban territories. As for the temporal resolution, obtaining regular maps with a better release frequency would allow for more continuous monitoring of changes in the territory. Creating a map with both of these improvements would highly benefit the city council's spatial planning, as more accurate LULC information would be provided, leading to more precise calculations of monitoring indexes such as the number of illegal structures and proportion of territory occupied by forests or agriculture.

Therefore, this research work investigated the applicability of using machine learning classification algorithms with satellite data, in this case Sentinel-1 and Sentinel-2, and derived products, to create functional and precise LULC maps in the region of Almada, with a higher spatial and temporal resolution than COS. Since the last version of COS is from 2018, LULC classification models and maps were produced for this year.

1.3 Goals

The main goal of this research was to create a 2018 LULC map for the Almada region, in order to study whether satellite data and derived products could be used in conjunction with automatic classification algorithms to produce accurate LULC maps. In addition to this goal, several other objectives were accomplished:

- Comparison of two different methodologies for LULC classification, Pixel-Based Image Analysis (PBIA) and Object-Based Image Analysis (OBIA);
- Comparison between sets of input data, created with different combinations of Sentinel-1 and Sentinel-2 imagery and derived products;
- Comparison between two classifiers, XGB and RF;
- Comparison between two methodologies of ground truth acquisition, manual and semi-automatic;
- Examination of the best LULC maps against the main reference map used in Almada, COS, and a recently released reference map, COSsim.

1.4 Document Outline

The present work is divided in 8 different chapters which encompass the following content:

- **Introduction:** Introductory in nature, this chapter establishes the context and motivation for this dissertation, define its objectives and present its structure;
- **Background Theory:** This chapter presents the theoretical background for the thesis. Several machine learning topics are introduced, as well as detailed descriptions of the utilized satellites and its products.
- **State of the Art:** This chapter presents a survey of the existing research and state of the art techniques on supervised LULC classification using remote sensing.
- **General Approach:** The general approach to the research problem is defined, including a description of the execution plan and a detailing of several key components of this problem.
- **Methodology:** This chapter fully details all sections of the proposed approach and the experimental setup is presented;

- **Results - Pixel Based Approach:** This chapter contains the presentation and analysis of the results obtained using the pixel-based approach.
- **Results - Object Based Approach:** This chapter contains the presentation and analysis of the results obtained using the object-based approach.
- **Conclusions:** In this final chapter, the main conclusions achieved across this work are presented, and a reference to future work is made.

2

Background Theory

This chapter presents the theoretical background for the dissertation. It is divided into two main sections, representing the major technologies employed in this dissertation: Machine learning and Remote Sensing. In each section, several related subjects are introduced and detailed.

2.1 Machine Learning

Machine learning is an branch of Artificial Intelligence which creates systems capable of learning from data by identifying patterns [8]. In LULC mapping, machine learning techniques are often applied in the form of supervised and unsupervised classification algorithms [58]. This dissertation will focus on supervised classification.

Supervised Learning describes a class of problems in Machine Learning in which the training data is composed of input examples and their corresponding target variables. The objective of the algorithm is to find an appropriate function F, that correctly maps the input examples, X, to the target variables, Y, such as:

$$F : X \rightarrow Y \tag{2.1}$$

Supervised learning models learn by making successive predictions about the input data, and being corrected by comparing their answer to the real labels. After training they are used to make predictions on a second set of data, the test data. These predictions are then compared to the real target labels in order to produce an estimate of the accuracy or error of the model [8].

2.1.1 Classification Algorithms

Classification problems are one of the main types of supervised learning, and their principal goal is the prediction of a class or category through the input data.

There are a myriad of classification algorithms but RF, Support Vector Machine (SVM) and k-Nearest Neighbor (kNN) are the most widely used in LULC classification [65, 61, 47]. In recent years, the XGB classifier has also been used frequently, delivering good results [66, 33]. In this research, only RF and XGB classifiers were utilized.

2.1.1.1 Random Forest

Random Forest is a supervised machine learning algorithm, widely used in classification and regression problems. This method is composed of a large number of individual decision trees, that operate as an ensemble, and is based on the idea that the combination of multiple uncorrelated models working towards the same goal produces a more overall robust model, which surpasses the individual decision trees [10]. Each tree works individually and the final prediction is obtained by the majority vote of all trees in the forest. An illustration of this type of classifier can be observed in Figure 2.1.

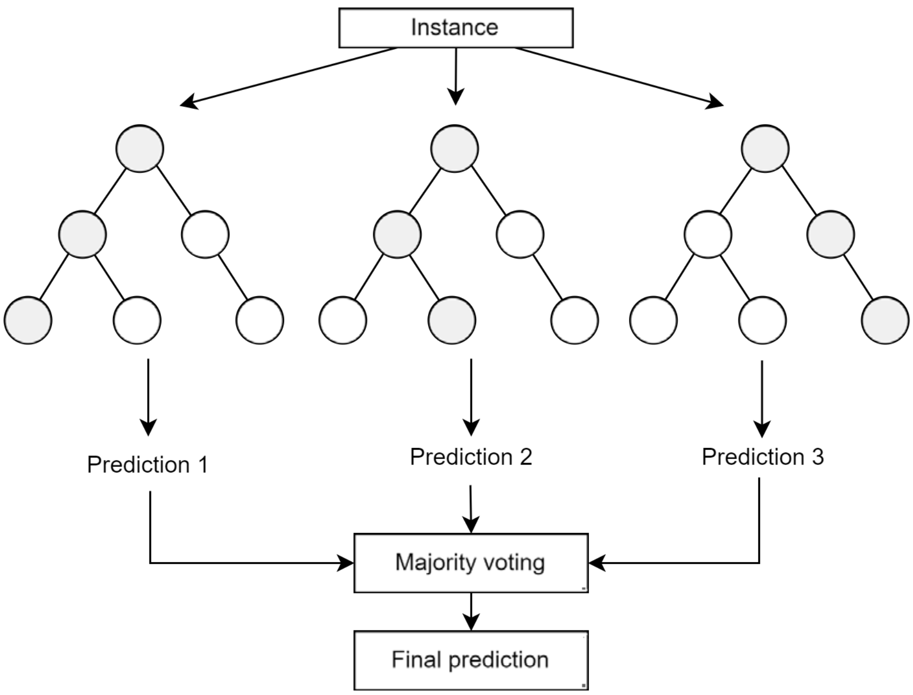

Figure 2.1: Random Forest illustration. Adapted from: `https://www.tibco.com/reference-center/what-is-a-random-forest`

RF use the **Bagging** (**Boostrap Aggregation**) technique, in which each individual decision tree is trained on a training set of the same size of the original, obtained by random sampling it with replacement. Using this method, the training samples of each tree will be slightly different, creating uncorrelated individual models. In addition, each tree is given only a random subset of the original features to choose, resulting in a greater amount of diversity.

This algorithm can handle high dimensional data, is robust to outliers and not particularly computationally intensive, although a great amount of memory is required [27].

2.1.1.2 XGBoost

XGBoost, which stands for e**X**treme **G**radient **Boost**ing, is an implementation of gradient boosted decision trees optimized for speed and performance [12]. Similar to RF, XGB, represented in Figure 2.2, is an ensemble learning method, which uses the results of several individual decision trees to provide the predictions. However, in contrast with RF, it employs the **Boosting** technique.

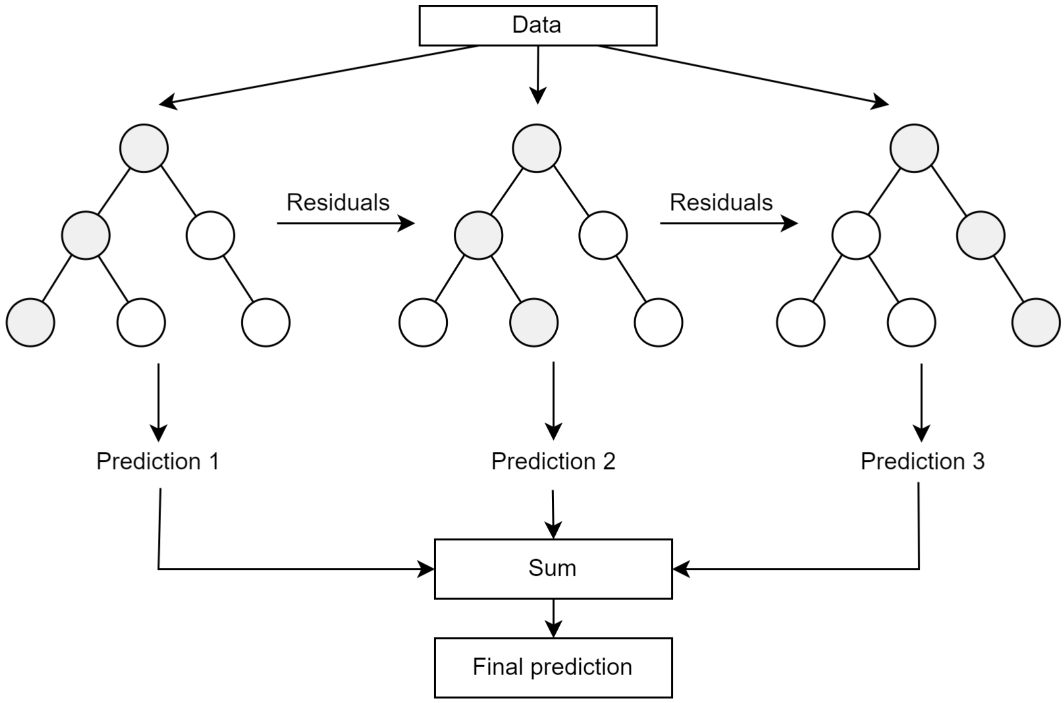

Figure 2.2: XGB illustration. Adapted from: Deng et al. (2021) [18]

The biggest difference between **Bagging** and **Boosting** is that in **Boosting**, the decision trees are built in sequence, and each subsequent tree aims to reduce the errors (in gradient boosting, using the gradient descend algorithm) of the previous one. At each iteration after the first tree, the incorrect classified samples are given heavier weights, forcing the next tree to focus on their performance. The complete classifier is combination of weak learners that result in a stronger and robust model.

2.1.2 Model evaluation

Model evaluation is an essential step in any Machine Learning pipeline since the usefulness of any model relies on its ability to generalise from the training data and provide trustworthy predictions.

In classification problems, the most frequent method for model evaluation is the analysis of confusion matrices, which are tables that provide insight into the predictions obtained by the models.

Table 2.1 represents an example of a confusion matrix for a fictitious classifier with 3 classes. Each row of the table represents the number of instances predicted for each class and each column represents the number of real instances in each class. In the diagonal from the top left corner to the bottom right corner are the instances which were classified correctly, with the remaining being misclassifications.

		True		
		A	B	C
Predicted	A	8	1	2
	B	0	5	1
	C	3	2	10

Table 2.1: Example of a confusion matrix

Through the confusion matrix it is possible to calculate several metrics:

$$\text{overall accuracy (OA)} = \frac{TP + TN}{TP + TN + FP + FN}, \tag{2.2}$$

$$\text{precision} = \frac{TP}{TP + FP}, \tag{2.3}$$

$$\text{recall} = \frac{TP}{TP + FN}, \tag{2.4}$$

$$\text{F1 score} = 2 \cdot \frac{\text{precision} \cdot \text{recall}}{\text{precision} + \text{recall}}, \tag{2.5}$$

in which **TP** represent the true positives, **TN** the true Negatives, **FP** the false positives and **FN** the false negatives of the model.

In LULC classification, when assessing map accuracy, the metrics used are:

- **User's Accuracy:** Proportion of the classes in the map that are in fact correct. Equal to the precision metric and complement of the Comission Error.
- **Producer's Accuracy:** Proportion of true classes on the ground which were predicted accurately. Equal to the recall metric and complement of the Omission Error.
- **Comission Errors:** Proportion of instances that were predicted as a certain class but are not actually part of that class.
- **Omission Errors:** Proportion of instances of a certain class but were not predicted.

One additional metric that can be derived from the confusion matrix is **Kappa**, or Cohen's Kappa. **Kappa** is a statistic that can be used for evaluation of a single model or for the comparison of multiple classifiers, and compares the accuracy of the model to that of a random system. It is calculated with the following formula:

$$\text{kappa} = \frac{p_0 - p_r}{1 - p_r}, \tag{2.6}$$

in which p_0 is the Overall Accuracy (OA) of the model and p_r is the probability of random accuracy.

The probability of random accuracy is calculated with the following formula [29]:

$$p_r = \sum_{k}^{K} p_k \cdot t_k, \tag{2.7}$$

in which p_k is the number times that class k was predicted and t_k the number of actual instances of class k.

Kappa's values can range from 1 to negative values. For a perfect model, the kappa value is 1, for a random model, 0, and for a model whose OA is worse than that of a random model, negative.

Kappa is extensively used in LULC classification [60, 67], and it is a useful metric especially when the class distribution is imbalanced.

2.1.3 Image Segmentation

Image segmentation is the process of partitioning an image into multiple objects (segments), which are created by analysing the pixels values and grouping similar regions. Most of the reviewed OBIA classification papers perform image segmentation using the software eCognition, primarily with the algorithms Mean Shift Segmentation and Multiresolution Segmentation [34]. However, as eCognition is a paid software, the implementation of Mean Shift Segmentation (MSS) on Orfeo ToolBox (OTB) was used. This implementation has been shown to produce good results in land-cover mapping [45].

Mean Shift is a general non-parametric mode finding algorithm, first proposed by Fukunaga et al. (1975) [24] and further developed by Cheng (1995) [14], which has several applications, such as clustering [11] and image segmentation [16].

OTB's MSS implementation is a combination of two main processes: an initial **Mean Shift Filtering** and a subsequent segmentation step. Two parameters, spatial and range radius, highly influence the output of the algorithm.

The **Mean Shift Filtering** process repeats the following steps for each pixel of the image:

1. Determination of the set of neighboring pixels by a spatial (**s**) and range window (**r**): all pixels within radius **s** that have a value difference with the center pixel equal or lower than **r** are included.

2. Calculation of the spatial center and the value mean of the set.

3. Utilization of the new spatial center as the center for the next iteration's spatial and range window.

4. Repeat steps 1, 2 and 3 until convergence.

5. After convergence, attribute to the initial pixel the value of the last obtained value mean.

Subsequently, the segmentation step clusters the pixels by grouping neighbor pixels whose range distance is within the range radius. The full procedure is detailed by Michel et al. (2015) [48].

2.2 Available Remote Sensing data and derived products

The two constellations most relevant to the dissertation topic are Sentinel-1 and Sentinel-2, both due to their high revisit time and spatial resolution. In this section, this satellites are presented, as well as two products that can be derived from their imagery: spectral indices and texture information.

2.2.1 Sentinel-1

Sentinel-1[1] is the first satellite constellation in the Sentinel series of the Copernicus program managed by the Europen Comission, and it consists of two polar-orbiting satellites (1A and 1B), launched in 2014 and 2016 respectively, operating day and night.

The Sentinel-1 mission has an average revisit time of 6 days and the spatial resolution varies across the different operational modes. Interferometric Wide Swath, the main acquisition mode over land, has a spatial resolution of 5 ×20m.

This satellite carries a C-band Synthetic Aperture Radar (SAR) active sensor, which means that it can obtain data regardless of cloud coverage, weather condition or lack of ilumination, which supports operation in single polarisation (HH or VV) and dual polarisation (HH+HV or VV+VH).

In this dissertation, polarizations 'VV' and 'VH' in the Interferometric Wide Swath mode, were used.

2.2.2 Sentinel-2

Sentinel-2[2] is the second mission in the Sentinel series of the Copernicus program, consisting of two polar-orbiting satellites, launched in 2015 and 2017, respectively. These satellites are phased at 180 degrees, and offer a revisit time of 5 days at the Equator and 2-3 days in mid-latitudes.

Sentinel-2's data is high-resolution, wide-swath and multi-spectral, with 13 different bands, presented in Table 2.2. In this dissertation all bands were used, with exception of **B10**.

[1] https://sentinel.esa.int/web/sentinel/missions/sentinel-1, Accessed on 2020-02-20
[2] https://sentinel.esa.int/web/sentinel/missions/sentinel-2, Accessed on 2020-02-20

Table 2.2: Sentinel-2 bands

Band	**Spectral region**	**Wavelength** (nm)	**Spatial Resolution** (m)
B1	Coastal aerosol	443	60
B2	Blue	492	10
B3	Green	560	10
B4	Red	665	10
B5	Red-Edge	704	20
B6	Red-Edge	740	20
B7	Red-Edge	783	20
B8	Near Infrared	833	10
B8A	Near Infrared narrow	865	20
B9	Water vapour	945	60
B10	Shortwave infrared/Cirrus	1374	60
B11	Shortwave infrared	1610	20
B12	Shortwave infrared	2190	20

The multispectral instruments in these satellites are passive sensors, which means that the capturing of data is often disturbed by the weather, since the sensors are not able to penetrate the clouds.

2.2.3 Spectral Indices

Spectral indices are produced through the combination of various spectral bands of an image, and are widely used in classification using remote sensing. In this dissertation, three spectral indices were employed: Normalized Difference Vegetation Index (NDVI) [41], to help identify vegetation, and the Normalized Built-Up Index (NDBI) [73] and Built-Up Index (BUI) [32] to distinguish artificial territories. The formulas of the mentioned indices are:

$$NDVI = \frac{NIR - Red}{NIR + Red}, \tag{2.8}$$

$$NDBI = \frac{SWIR - NIR}{SWIR + NIR}, \tag{2.9}$$

$$BUI = NDVI - NDBI, \tag{2.10}$$

where NIR represents a near-infrared band, Red represents a red band and $SWIR$ represents a short-wave infrared band.

Figure 2.3 presents a comparison between ortophotos and the three indices, calculated using Sentinel-2 images, for a small area in Almada. In Figure 2.3b the highest values (white color) correspond to the vegetation in the orthophotos, while in Figure 2.3d and 2.3c, correspond to the artificial territories. Comparing the two built-up indices, its possible to observe that Figure 2.3c has slightly more contrast and the edges of the objects on the ground seem to be better defined.

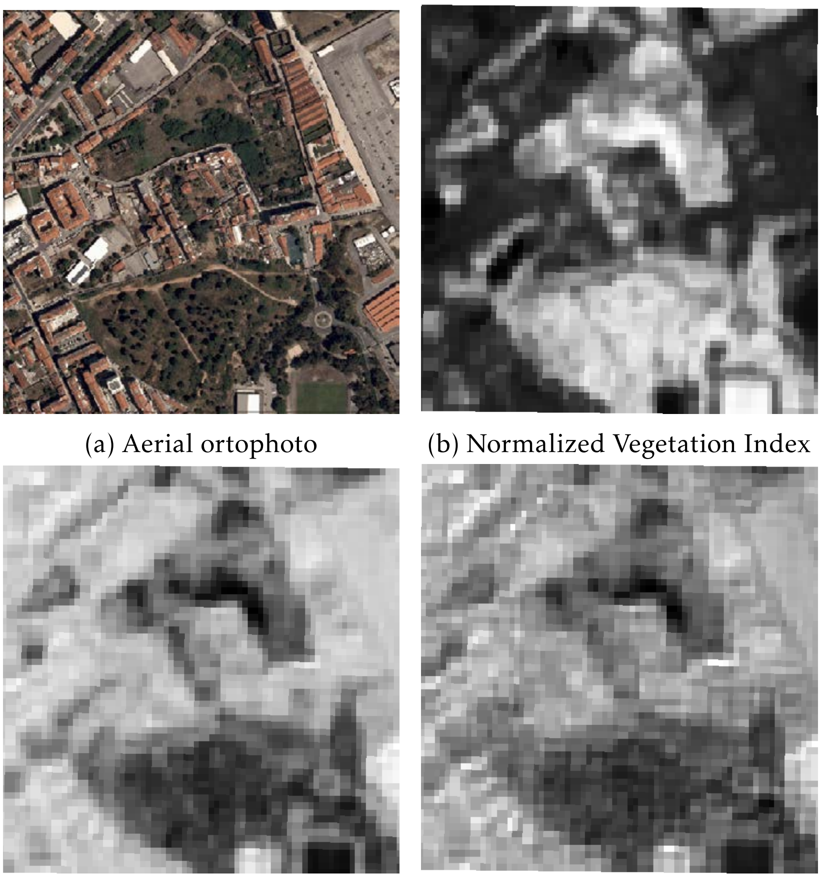

(a) Aerial ortophoto (b) Normalized Vegetation Index

(c) Built-Up Index (d) Normalized Built-Up Index

Figure 2.3: Comparison between orthophots and spectral indices

2.2.4 Texture information - GLCM method

In image processing, texture is characterized by the spatial distribution of the brightness intensity of a region of pixels. Obtaining texture information about the surface of the Earth is an essential process for LULC classification, and it is frequently done by using the Gray-Level Co-Occurence Matrix (GLCM) method [42, 37].

The GLCM method is a statistical process of extracting texture features, initially proposed by Haralick et al. (1973) [31], which consists of creating the GLCM of an image and from it extracting statistical information.

The GLCM of an image indicates how often a pixel with value **i** occurs in a specific spatial relationship with pixels of the value **j**. Figure 2.4 represents this process for a fictitious 3x3 image. In this case, the spatial relationship analyzed was between each pixel and its right neighbor. For example, in the 3x3 image, 0 value pixels appear to the right of 1 value pixels two times, and as such, this will be the value of the (1,0) element in the GLCM.

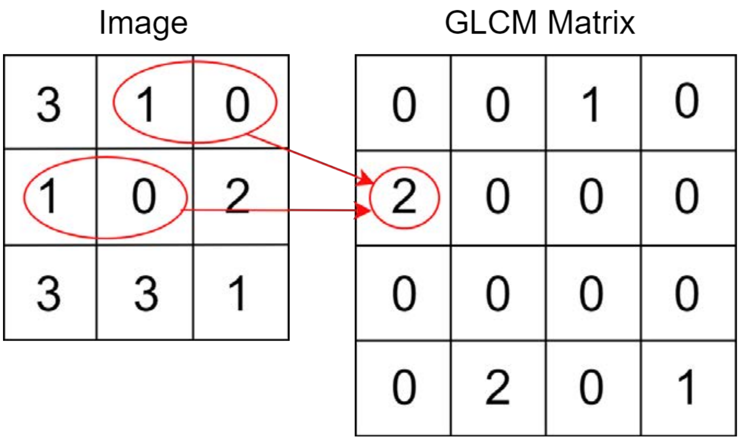

Figure 2.4: GLCM matrix calculation example

From this matrix, several texture features can be extracted, whose formulas are detailed by Haralick et al. (1973) [31]. Figure 2.5 presents three of these features, Energy, Entropy and Haralick Correlation, calculated using Sentinel-2 images, as well as an ortophoto of the same area.

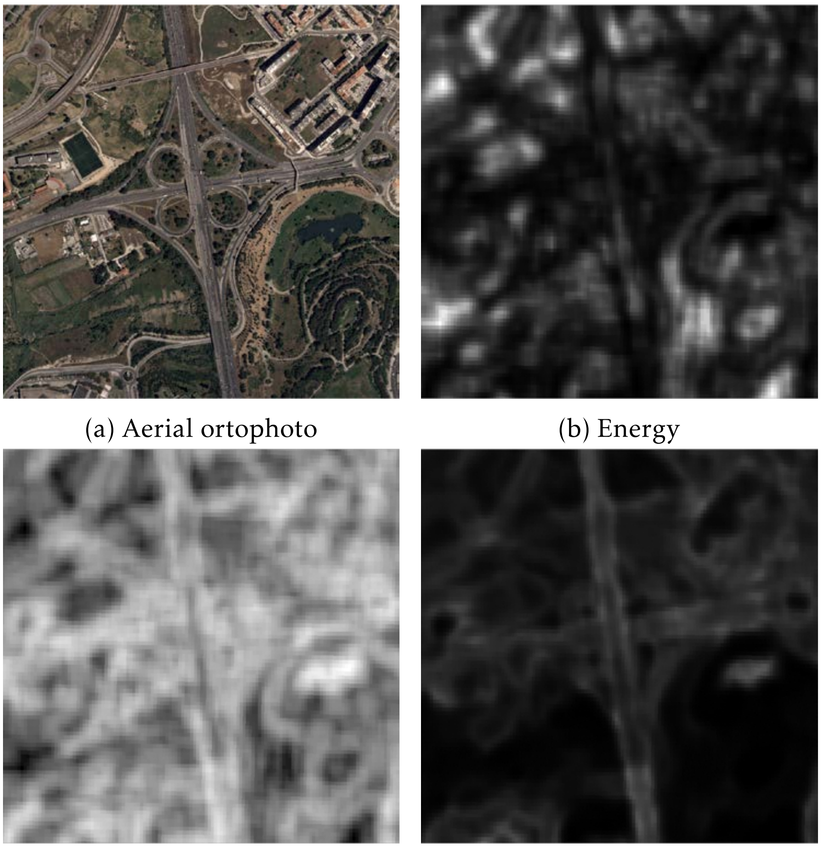

(a) Aerial ortophoto

(b) Energy

(c) Entropy

(d) Haralick Correlation

Figure 2.5: Comparison between orthophots and textural features

3

State of the Art

Similarly to any other research problem, a thorough reviewing of the literature surrounding the dissertation themes is necessary. This chapter presents the main findings of that review.

First, the two most common approaches to LULC classification, pixel-based and object-based are explored, with multiple studies in distinct areas, using different classifiers and combinations input data being reviewed. Subsequently, the utilization of the XGB classifier and textural features extracted using the GLCM method are further investigated, followed by an analysis of image segmentation evaluation techniques.

3.1 Approaches to LULC classification

The first automatic methods for LULC classification were developed through the use of PBIA, which analyses an image pixel by pixel. Supervised and unsupervised learning can and have been used throughout the years, although this dissertation focuses specifically on the supervised problems. Parametric and non-parametric classifiers have been explored, although the use of the former has been decreasing over the years due to the fact that the input data is usually not normally distributed, which is a core assumption of these type of classifiers [57]. The most frequently used classifiers are RF, SVM and kNN [67, 35, 3].

Another type of approach using OBIA is also widely used in LULC classification [58]. OBIA methods segment the image into objects of similar pixels, and use information about these objects to perform the classification [19]. As with PBIA methods, multiple types of classifiers have been utilized, mostly non parametric, such as SVM and RF [28, 15].

3.1.1 Pixel-based approach

As mentioned before, the pixel-based approach to LULC classification uses the pixel as its basic unit. Each pixel is classified based on its spectral properties, as pixels from the same class tend to have similar properties [57].

One limitation of this type of approaches is that it usually does not take into account the neighbourhood of each pixel, meaning that there is no spatial context included in the classifier. This limitation is especially prominent in Land Use classification, since each land use class can be composed of multiple land cover classes, with varied spectral properties [75]. In order to surpass this limitation, several researchers combine the satellite imagery with extracted textural features [69].

Nguyen et al. (2020) [50] studied LULC classification using multitemporal sentinel-2 imagery, and tested fours classifiers, logistic regression (parametric), RF, improved kNN and SVM (non-parametric), in Dak Nong, a vietnamese province. A total of 446 images from 2017 and 2018 were collected and divided into four time periods: dry season 2017-2018, rainy season 2017-2018, a combination of the two seasons, and the year 2017. They utilized a combination of 10 Sentinel-2 bands, all resampled at 10 meter resolution, with the addition of NDVI and information from a Digital Elevation Model (DEM). The classes distinguished in this study can be observed in Table 3.1

Table 3.1: Classes distinguished in Nguyen et al. (2020) [50]

Class names
Dense evergreen broadleaved forest
Open evergreen broadleaved forest
Semi-evergreen forest
Deciduous dipterocarp forest
Plantation forest
Mature rubber (more than 3 years old)
Perennial industrial plants
Croplands
Residential area
Water surface
Other lands (grassland, shrubs, bare land, and abandoned land...)

The model with the highest accuracy was found by using the composite set of the two seasons in 2017-2018, with SVM reaching an OA of 80.3% and Kappa of 0.813. Analyzing this result by class, the authors found that the ones with the worst accuracy were croplands and residencial areas. These findings are mostly consistent with the literature. Residential areas and cropland are two land use classes, which, as mentioned, are harder to classify using a pixel-based method [75]. Including the DEM information was not enough for these classes to reach high levels of accuracy. The lowest accuracy was obtained using the combination of logistic regression with the rainy season imagery, with OA of 63.9% and Kappa of 0.611.

The authors conclude that using multitemporal images from different seasons increases the accuracy of the model due to the additional information provided by each of them for the same land cover classes. One final remark is that although SVM was the best performing classifier, RF had extremely similar results (OA of 80.0% and Kappa of 0.802) and was less computationally demanding. This is congruent with the findings from Noi et al. (2017) [56]. and Abdi (2020) [1].

Noi et al. (2017) [56] produced a comparative study between RF, kNN and SVM for Land Cover Classification using Sentinel-2 images. A total of six LULC classes were distinguished in an area within the Red River Delta of Vietnam, and the effect of the size of the training samples was investigated. The training data was divided into 14 sets, in which seven were imbalanced, with percentages from the total training data ranging from 5 to 100, and seven were balanced, with 50 to 1250 pixels per class.

In the classification with the imbalanced sets, SVM always produced the highest accuracies, followed by RF and kNN, with the discrepancy between classifiers being larger in the smaller sample sizes. The highest accuracies for each classifier were not found in the largest sample size, but in sets that represented approximately 0.26% of the total study area. In the balanced sets, the ranking of the classifiers' accuracy was equal to that of the imbalanced. In general, the three algorithms all showed improvement when the size was increased up until a certain point (more than 750 pixels per class), in which the results hit a plateau.

SVM was found to be simultaneously the algorithm with the highest OA, and the least reactive to changes in training data size. Nonetheless, if the training data is sufficiently large, all three classifiers have comparable OA in both types of datasets. The authors close with the suggestion that training sample size should be aproximately 0.25% of the total area of the work.

Tavares at al. (2019) [69] investigated the effects of the combination of optical and SAR products, on LULC classification in Belém, Brazil with the group of classes presented in Table 3.2. Two Sentinel-1 images with an C-band SAR Interferometric Wide Swath (IW) in dual polarization mode (VV + VH) were collected, as well as one image with no cloud coverage, from Sentinel-2 Level-1C. For the classification all Sentinel-2 bands were used, except for SWIR/Cirrus. In conjunction with the images, multispectral indexes derived from S-2 were used (NDVI, Normalized Difference Water Index (NDWI) and Soil Adjusted Vegetation Index (SAVI)), as well as textural features calculated using the GLCM method using Sentinel-1 images. The classification algorithm chosen was RF.

The results demonstrate that the combination of both satellites provided the most accurate classification, with an OA of 91.07% and Kappa of 0.8709. As predicted, the single Sentinel-1 imagery provided the worst results with an OA of 56.01% and Kappa of 0.4194. As for the models completed with information derived from the satellites, although the inclusion of texture features did increase the accuracy of Sentinel-1 classification, the same did not happen with Sentinel-2, whose classification accuracy slightly dropped from 89.53% to 87.095% of OA and from 0.8487 to 0.8132 for the Kappa.

The authors conclude that although the application of spectral indices and texture information has been widely recognized to improve LULC classification, this isn't always the case. A final recommendation, based on their best results, is made for the synergetic use of both Sentinels for LULC classification, which is corroborated by other works [71].

Table 3.2: Classes distinguished in Tavares at al. (2019) [69]

Class names
Agriculture
Airport
Bare soil
Beach
Built-up
Grassland
Highway
Mining
Primary vegetation
Urban vegetation
Water with sediments
Water without sediments

3.1.2 Object-based approach

As the name evokes, object-based approach uses objects as its basic unit, which are composed of similar pixels. The greatest advantage of the OBIA methods is the homogenization introduced by the segmentation step, which leads to a reduction of the within class variation and the salt-and-pepper effect common in PBIA approaches [57]. In addition, in this type of approach other types of spatial information can be calculated, such as geometric attributes that describe the overall shape of each segment. The biggest challenge when using this type of approach is choosing the appropriate parameters for the segmentation. Multiple studies have been conducted using OBIA with high degrees of accuracy [28, 15].

In a paper by Clerici et al. (2017) [15], LULC classification was performed using both Sentinel-1A and Sentinel-2A data, for the lower Magdalena region, in Colombia. Spectral indices were calculted from Sentinel-2, as well as texture measures from Sentinel-1, and utilized in conjunction with both satellites' images, resampled to 10 meters.

The object-based classification was performed using the software eCognition. After obtaining the segmentation, the classifiers were trained on six classes: forests, secondary vegetation/shrubs, cropland, water, pastureland and built; using 160 locations obtained from Google Earth and on-site. Three different classification algorithms were tested, SVM, RF and kNN and, in order to evaluate the fusion of information from both satellites, the individual layers were also tested separately.

Like in the case of Tavares at al. (2019) [69], the worst accuracies were achieved with the sole use of Sentinel-1. SVM was the superior classifier in all of the tests, achieving the maximum OA of 88.75% and Kappa of 0.86 in the combination of both satellites. The classes secondary vegetation/shrubs and cropland had the lowest accuracies, and the authors theorize that this might be due to the model not being able to capture their high spectral variance.

Sánchez-Espinosa et al. (2019) [62] studied the use of Sentinel-2 and Landsat8 imagery for LULC classification in a Mediterranean wetland area. Images were collected from both satellites from autumn 2015 to summer 2016, and Sentinel-2's 20 meter bands were resampled to 10m. As reference data, the researchers used LULC maps produced by the regional government of Andalucia, and a total of 12 classes were distinguished, present in Table 3.3

Table 3.3: Classes distinguished in Sánchez-Espinosa et al. (2019) [62]

Class names
Urban
Arable land
Vineyards
Fruit trees and berry plantations
Olive groves
Grassland
Mixed forest with tree cover density higher than 80%
Mixed forest with tree cover density between 30% and 50%
Sclerophyllous vegetation
Inland marshes
Water courses
Areas without vegetation

The classifications were obtained using GeoClassifier, a Geographic Information System (GIS) software. This software first performs the image segmentation using spectral and geometrical characteristics, then trains the classifier using those segments and finally performs the test image classification and calculates the statistics. The parameters for the segmentation were found using a process of trial and error. To train the model, a minimum of 30 segments for each class were used and the classifier utilized was the maximum-likelihood.

Overall, the results obtained with Sentinel-2 were slightly better than Landsat8, with an OA of 88-87%, although both satellites obtained comparable results. The classes with the best results were agriculture and wetland, and the one with the lowest accuracy was urban, with around 61% of accuracy. The authors explain these low results by outlining the fact that the tested area is a rural region with elements like roads and dispersed houses, which are too small to be detected. They also note that there seems to be some confusion between areas under construction and areas without vegetation, and between green urban areas and natural vegetation.

3.1.3 Comparison of pixel and object methods

Goodin et al. (2015) [28] compared the results of LULC mapping using both pixel and object based approaches with an SVM classifier, in a complex agricultural landscape along the Ukraine-Poland border. The input data was obtained from a single date from Landsat

8 OLI, with bands 2-7 being used. Table 3.4 contains the land cover classes distinguished in this and Table 3.5 contains the land use classes.

Table 3.4: Land Cover classes distinguished in Goodin et al. (2015) [28]

Class names
Artificial/urban
Bare
Grasslands or Herbaceous cover
Woodland
Wetland
Water

Table 3.5: Land Use classes distinguished in Goodin et al. (2015) [28]

Class names
Artificial/urban
Arable land Type 1
Arable land Type 2
Pasture/abandoned
Heterogeneous agriculture
Forest - mixed
Forest - coniferous
Wetland/pasture
Water

Image segmentation was performed using the ENVI Zoom module and the parameters were obtained by trial and error. Following the segmentation, two types of attributes were calculated: spectral, related to the reflectance properties of the objects, and spatial, related to their geometry and texture.

As for the land cover results, both methods produced similar results, with OBIA resulting in a slightly more accurate map, although not statistically significant. In the land use classification, OBIA using both spectral and spatial attributes obtained the highest result, with an OA of 75%. Pixel based classification performed similarly to OBIA using only spatial characteristics, and OBIA using only spectral attributes outperformed them both.

The authors conclude that the OBIA method does not inherently provide a significant improvement for the OA of land-cover classification, since this task is more closely related to the spectral properties of the elements. As for land use, when the combined OBIA method was used, a noteworthy improvement was produced in overall accuracy, and especially in the agriculture classes.

The researchers also mention that although a single image was used for the study, this was done because it was the only available image. They attribute their lower OA, in comparison with other LULC classification studies, to this limitation and theorize that improvements could be achieved by using multitemporal imagery.

3.2 XGB classifier in Land-Use Land-Cover classification

The most prevalent machine learning classifiers for LULC classification in the last decade have been Support Vector Machines, Random Forests and K-Nearest Neighbours, with RF and SVM being considered the best techniques, with consistently high results in several OBIA and PBIA studies [67, 46, 54, 44].

However, Gradient Boosting Machines, in particular Xgboost, a regularized implementation of Gradient Boosting Machines (GBM) developed by Chen and Guestrin (2016) [12], has recently risen in popularity and have achieved excellent results [66, 26, 33].

Georganos et al. (2018) [26] developed a comparison of the XGB classifier with RF and SVM in an object-based urban LULC classification, with a diverse group of land use and land cover classes. The authors concluded that the XGB, optimized with a Bayesian model, consistently outperformed the other classifiers, although it had an increased computational time.

Additionally, Dobrinić et al. (2020) [66] tested RF and XGB in a LULC classification of Lyon, France, with a combination of Sentinel-1 and Sentinel-2 imagery, and the group of land cover classes presented in Table 3.6. Similar to Georganos et al. (2018) [26], the XGB classifier slightly outperformed RF, although in this study the computational time was lower for the XGB.

Table 3.6: Land Cover classes distinguished in Dobrinić et al. (2020) [66]

Class names
Water
Bare soil
Forest
Built-up
Low vegetation

In Portugal, Neves et al. (2019) [49] explored Sentinel-1 and Sentinel-2 imagery for the detection of permanent structures using the XGB classifier. The final results were robust, with the classification model being able to identify structures which were not represented in the reference data.

3.3 Textural features - GLCM

Research shows that the use of textural information in classification when combined with spectral data, can increase the accuracy by helping to distinguish areas with spectral similarities in both object and pixel-based studies [42, 5, 68].

Textural features can be extracted from images using a multitude of techniques, and one of the most common is through the utilization of the Gray Level Co-Occurrence Matrix. As mentioned in the previous chapter, Haralick et al. (1973) [31] proposed several statistical measures, which have achieved good results when used in LULC classification [53, 6, 55].

A study by Kupidura (2019) [42] reported an increase in kappa value when combining GLCM features with spectral properties, to classify Sentinel-2 imagery with the group of classes in Table 3.7. The author applied a Principal Component Analysis (PCA) to the satellite imagery, and calculated several versions of the GLCM matrix (with neighborhoods of 5, 7, 10 and 13) from the first component. Although all versions had a positive effect in classification accuracy, the best results were obtained with neighborhood 7. The class with the most improvement in accuracy was urban, with deciduous forest having a slight deterioration.

Table 3.7: Land Cover classes distinguished in Kupidura (2019) [42]

Class names
Water
Low vegetation
Bare soil
Urban
Coniferous forest
Deciduous forest

3.4 Image segmentation evaluation

Image segmentation is a key step in the OBIA approaches to LULC classification and obtaining a quality segmentation of the study area highly influences the classification results [34]. The most common segmentations algorithms used in remote sensing are region-based methods, such as the multiresolution and mean-shift algorithms, which generate good results but require parameter optimization that greatly influences the quality [34]. Therefore, the assessment and evaluation of segmentation quality is a crucial part of the OBIA methodology.

There are three main methods of segmentation evaluation: subjective, which is based on human visual judgment; supervised, in which the segmentation is compared to a segmented reference image; and unsupervised. The subjective methodology is the most common and has been used on a number of studies [34], although it is time consuming and limits the evaluation to a small number of comparisons [76]. In this dissertation, since no well segmented reference data exists, the review will focus on the topic of unsupervised evaluation.

Unsupervised evaluation methods measure the quality of the segmentations without requiring manual supervision, and are extremely useful when assessing the quality of a substantial amount of segmentations. These types of procedures usually calculate metrics that describe intra-region homogeneity and inter-region heterogeneity, and combine them into one overall index [76]. An optimal segmentation should have both high intra-region homogeneity, with each segment being composed of spectrally similar pixels, and high inter-region heterogeneity, with each segment being different from its neighbors.

One popular approach, proposed by Espindola et al. (2006) [21] uses the Moran's Index (MI) to measure inter-segment heterogeneity, and Area-Weighted Variance (WV) to measure intra-segment homogeneity. The WV is calculated as:

$$\mathrm{WV} = \frac{\sum\limits_{i=1}^{n} a_i * v_i}{\sum\limits_{i=1}^{n} a_i}, \tag{3.1}$$

where a_i and v_i are the area and variance of segment i, and n is the number of segments. The MI is calculated as:

$$\mathrm{MI} = \frac{n \sum\limits_{i=1}^{n} \sum\limits_{j=1}^{n} w_{ij}(y_i - \overline{y})(y_j - \overline{y})}{\sum\limits_{i=1}^{n} (y_i - \overline{y})^2 \left(\sum\limits_{i \neq j} \sum w_{ij} \right)}, \tag{3.2}$$

where n is the total number of segments, w_{ij} is the measure of spatial proximity (0 if segments Ri and Rj are not neighbors), y_i and y_j is the mean spectral value of segment R_i and R_j, and $\overline{y}$ is the mean value of the image.

The two indices are then normalized to a common range (such as 0 to 1) and the sum of the two normalized measures yields the final score of each segmentation, Global Score (GS):

$$\mathrm{GS} = \mathrm{WV}_{norm} + \mathrm{MI}_{norm} \tag{3.3}$$

The objective in this approach is to minimize both indices and consequently, the optimal segmentation is the one which obtains the lowest GS. Although this approach was developed for single band images, multispectral imagery has also been used, by averaging each band for the two indices [38].

However, Böck et al. (2017) [9] showed that this method has an instability introduced by the normalization of the indices, which makes the GS values sensitive to the range of segmentations tested and returns different optimums depending on that range. The authors proposed a normalization scheme using a fixed range, correspondent to the extreme values of the two indices. Since then, this new normalization has also been proved to be ineffective and results in the GS skewing towards the MI, selecting undersegmented segmentations as optimal [25].

3.5 Conclusion

LULC classification is highly dependent on the region and the chosen land use land cover classes. For this reason, it is impossible to assume which approach or methods will have the highest accuracy. Nonetheless, there seem to be certain topics which gather relative consensus, such as the utilization of multitemporal series, as opposed to a single image and the synergetic use of Sentinel-1 and Sentinel-2 imagery.

SVM and RF have both been extensively used in LULC classification, demonstrating excellent results [63]. Recently, the application of XGB to this type of problems has been growing, with comparable performances [26]. Since the use of XGB is still relatively uncommon, this research work focused on its comparison with one of the most common classifiers, RF. The choice of RF, in detriment of SVM, was made due to its computational speed and easy hyperparameter optimization [7], characteristics especially important when performing a significant number of experiences.

Including textural features in the classification models, specifically through the use of the GLCM method was studied in this review. Although the research by Kupidura (2019) [42] concluded that the use of such features had a positive influence on the classification kappa, the same was not verified by Tavares at al. (2019) [69]. These two studies were performed on different areas, with a completely different group of classes, and using different Sentinels, Kupidura (2019) [42] using Sentinel-2 and Tavares at al. (2019) [69], Sentinel-1. Consequently, this research will study the effect of the inclusion of textural features using the GLCM method, by performing separate experiments using Sentinel-1 and Sentinel-2 imagery.

After the review on segmentation evaluation, it is clear why the majority of OBIA approaches to classification still employ the subjective method to evaluate the segmentations. Additional research on segmentation evaluation, in particular the unsupervised version still needs to be executed [76]. Notwithstanding, this research will employ the use of the WV and MI proposed by Espindola et al. (2006) [21]. Due to the conflicting reports on the validity of GS, it was decided that it would not be used to automatically select the optimal segmentation. As such, the calculation of the two indices will be complemented by the subjective evaluation (visual analysis) when needed. Although this is not an ideal solution, as it requires a great amount of manual analysis, the creation and validation of segmentation metrics is a complex problem, which falls out of the scope of this dissertation.

Finally, it is important to mention the obvious exclusion of Deep Learning in this review. Convolutional Neural Networks (CNN) are the state of the art solution in various computer vision tasks, and have also been applied to LULC classification problems using remote sensing [64, 74]. However this approach has two main problems: the necessity for high amounts of training data and high processing power, in order to accurately understand the complexities present in remote sensing data [51]. Furthermore, some studies have shown that traditional machine learning produces competitive results, at a fraction of the computational time, and with a higher degree of interpretability [39]

4

General approach

The main goal of this dissertation was to study whether remote sensed imagery, specifically Sentinel-1 and Sentinel-2 and derived products, could be used to create functional LULC maps, in the context of the Almada municipality. Since the most recent version of the main reference map, COS, is from 2018, this region's 2018 LULC map was created.

Through the investigation produced by the state-of-the-art review, a proposed solution was developed. This chapter opens with a description of the execution plan for that solution, followed by the presentation of multiple key elements: the available reference data, the chosen classification classes, and the study region. Moreover, a recently released LULC map, a simplified version of COS (COSsim) is presented. The final section details the utilized software.

4.1 Proposed Solution

The proposed solution was achieved through a comparison between the two most common approaches to LULC classification, PBIA and OBIA, using two classifiers, Random Forests and XGBoost. Additionally, multiple combinations of satellite imagery and derived products were tested. The diagram in Figure 4.1 represents the general pipeline of the execution of this research.

The first three steps are common to both approaches. In **Data acquiring and pre-processing**, all satellite data was obtained and pre-processed, and in **Creation of derived products**, the spectral indices and textural features were calculated. In **Ground truth construction**, the reference data was used to create two ground truths for the future labelling of data for the classifiers.

Subsequently, two separate paths were followed. In the PBIA approach, the next phase was **Dataset creation**, where the two ground truths were random sampled and used to create all the different datasets. This was followed by **Classification**, in which the datasets were used to train and test several classification models. In the last step, **Accuracy Assessment**, all models were analysed and the best one was used to produce the final LULC map.

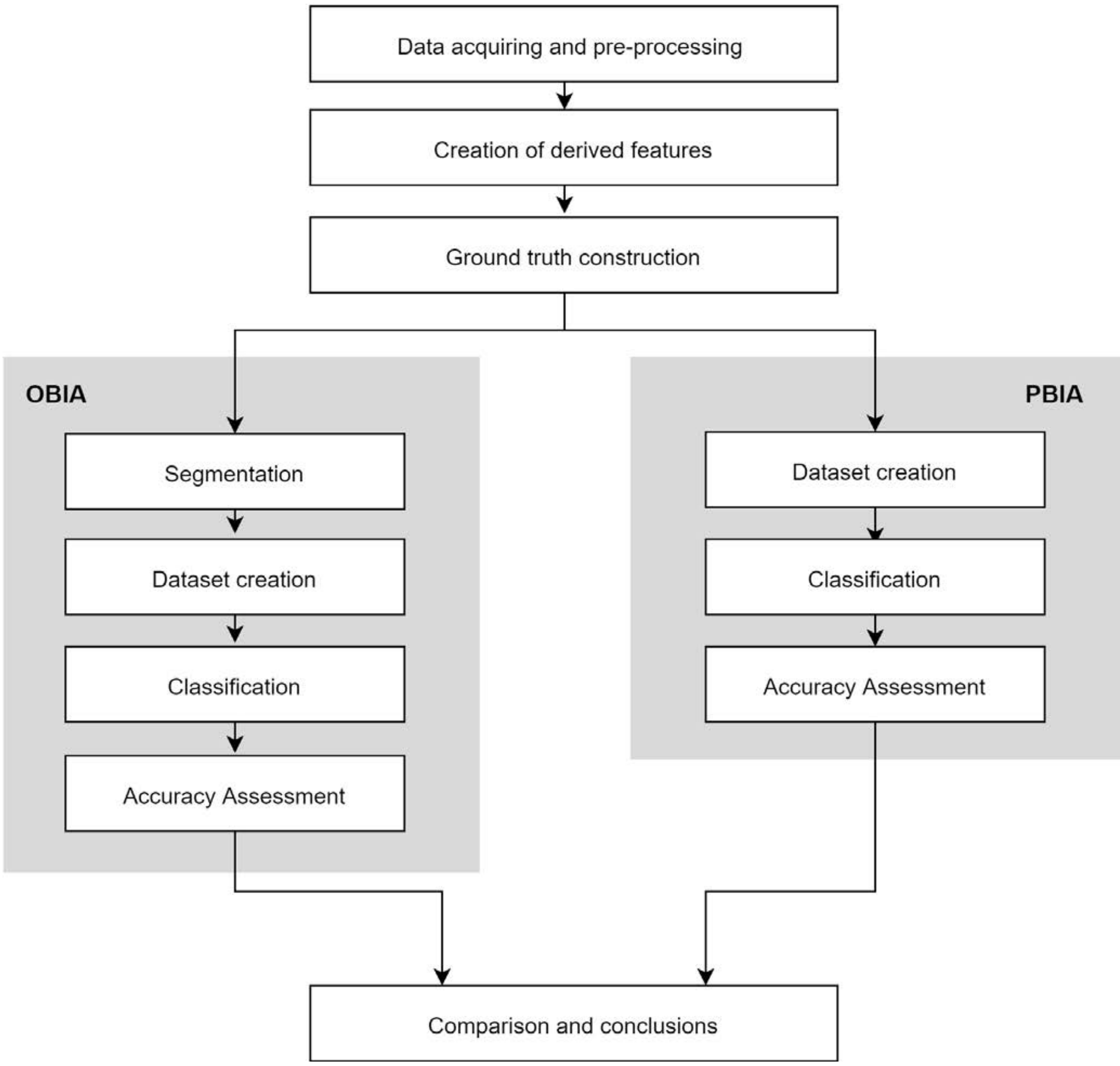

Figure 4.1: Diagram of the dissertation's general pipeline

The **OBIA** approach followed a similar path, with **Dataset creation** being preceded by a **Segmentation** step, which created the objects used to extract features and build the datasets.

The last phase, **Comparisons and conclusions**, consisted of a comparative review of the maps obtained by the best classification models, as well as a general comparison of the implementation of each approach.

4.2 Reference data

Supervised classification models are trained on labeled information. In this case, the input data to the classifier models is Sentinel-1 and Sentinel-2 imagery, as well as information derived from them, which are not labeled. As so, reference data was used to create ground truth to label the input data.

Two sources of information were used: the most recent COS, from 2018, presented in chapter 1, and a mosaic of aerial orthophotos, an example area of which is present in Figure 4.2. The orthophotos were created by the DGT, using a 2018 aerophotogrametric survey, acquired by the Instituto de Financiamento da Agricultura e Pescas, I.P (IFAP). They are available free of charge through WMTS visualization service, and cover the entirety of continental Portugal's territory, with a spatial resolution of 0.25m, providing information on four spectral bands, RGB and NIR.[1]

Figure 4.2: Example area (0,43289 km^2) of DGT's 2018 ortophotos

4.3 Classes and study region

One key detail in LULC classification is the choice of classes. Analysing the relevant literature, different groups of classes are used in every region and study, with some degree of overlapping.

For this research, the chosen classes were based on the Level 1 classes in COS 2018, with representation in the Almada municipality, presented in Table 4.1.

[1] https://snig.dgterritorio.gov.pt/, Accessed on 2020-11-06

Table 4.1: Level 1 COS 2018 classes, represented in Almada

Classes
1. Artificial Territories
2. Agriculture
3. Pastures
5. Forests
6. Spontaneous vegetation areas with shrub coverage (in Portuguese, *Matos*)
7. Bare and sparsely vegetated areas
8. Wetlands
9. Shallow bodies of water

After some initial tests, and a meeting with the Almada city council, it was decided that classes **Spontaneous vegetation areas with shrub coverage** and **Pastures** should be merged into a new class, **Other Vegetation**, due to their similarities. **Wetlands** was also added to this new class, due to its very small representation in the study region. For the same reason, **Shallow bodies of water** was eliminated from the group. The final group of classes can be observed in Table 4.2

Table 4.2: Final group of classes

Classes
1. Artificial Territories
2. Agriculture
3. Other Vegetation
4. Forests
5. Bare and sparsely vegetated areas

After determining the group of classes, it is important to describe the Almada municipality in their context and so, COS 2018 was used to estimate the proportions of each class. Analysing both Table 4.3, which presents the area of each class, and Figure 4.3, which visually represents the proportion, it is evident that the areas are extremely imbalanced, with **1. Artificial Territories** representing more than 50% of the region. This imbalance in representation was a critical detail in the research problem.

Table 4.3: Area of each class in Almada

Class	**Area (in km^2)**	**% of total area**
1. Artificial Territories	37.99	54.29%
2. Agriculture	8.20	11.72%
3. Other Vegetation	5.51	7.87%
4. Forests	16.53	23.67%
5. Bare and sparsely vegetated areas	1.71	2.44%
Total	**69.97**	**100.00%**

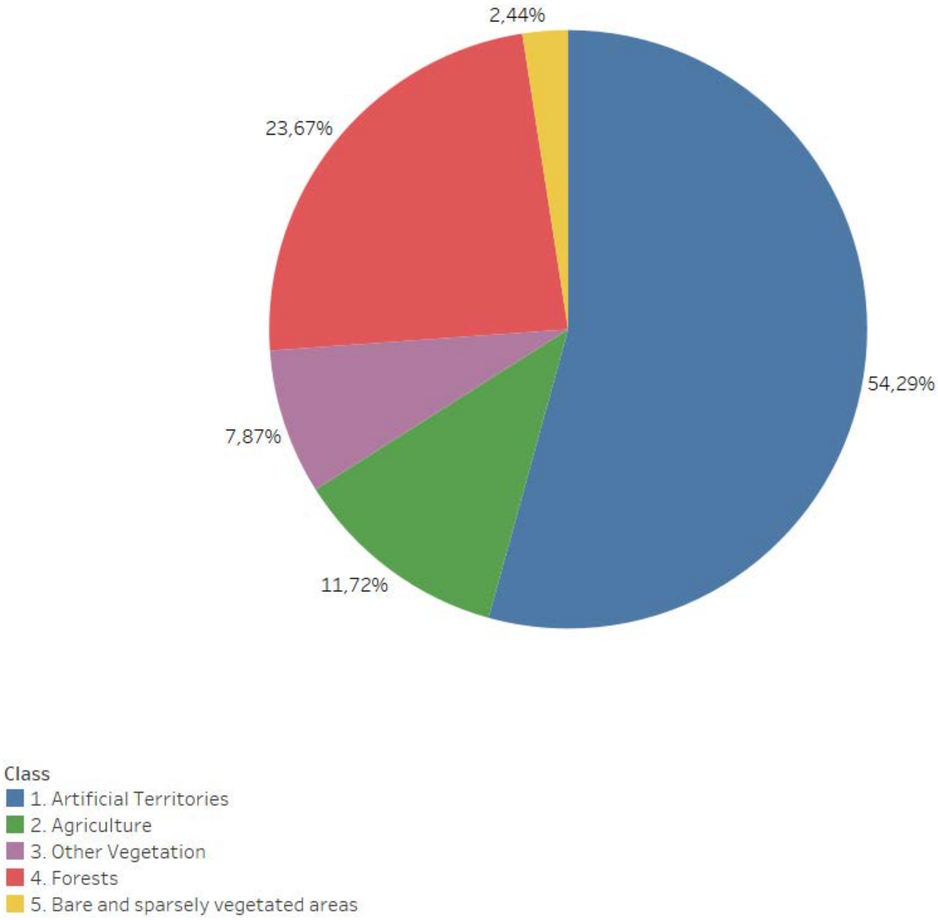

Figure 4.3: Proportion of each class in Almada

These areas are solely an approximation, as COS has a minimum mapping unit of 1 hectare and is not able to fully capture all objects. Additionally, there are some choices of classification in COS which do not fully align with the classes in this dissertation, such as identifying parks and golf courses as **Artificial Territories**. It is important to note that when talking about errors and inaccuracies in other maps, such as COS and COSsim, it is solely in the context of this dissertation, as they generally occur due to known limitations or specific methodological choices.

4.4 COSsim

During the development of this dissertation, a different product was made available by the DGT, COSsim[2], a simplified version of COS.

COSsim is a LULC map, created to provide complementary information to COS. It was

[2] `https://www.dgterritorio.gov.pt/COSsim-Carta-de-Ocupacao-do-Solo`, Accessed on 2020-11-07

produced through a combination of rules derived from expert knowledge and artificial intelligence methods, using time-series of Sentinel-2 imagery and spectral indices. The training samples were obtained through the automatic processing of ancillary information and by photo interpretation. More information about development of this product can be found in [17].

COSsim has a yearly production frequency and is made available in raster format with a spatial resolution of 10m (MMU of 100 m^2), in the EPSG:3763 coordinate system. The global precision of this map is 81.3% (±2.1%), obtained through a sample of 4018 points with a confidence level of 95%.

This map has three hierarchical levels of classification, with 6, 9 and 13 (or 15, from 2020 forward) classes, which are detailed in Table 4.4. It is interesting to note that COSsim's Level 1 classes correspond exactly to the ones chosen for this dissertation, with the exception of **Water and wetlands**, which has almost no representation in Almada.

Table 4.4: Classification nomenclature in COSsim

Level 1	**Level 2**	**Level 3**
1. Artificial	10. Artificial	100. Artificial
2. Agriculture	21. Agriculture	211. Annual autumn/winter crops 212. Annual spring/summer crops 213. Other agricultural areas
3. Forest	31. Broadleaf	311. *Quercus rotundifolia* and *Quercus suber* 312. Eucalyptus 313. Other broadleaf
	32.Coniferous	321. *Pinus pinaster* 322. *Pinus pinea* 323. Other coniferous
4. Shrub and spontaneous herbaceous vegetation	41. Spontaneous vegetation areas with shrub coverage	410. Spontaneous vegetation areas with shrub coverage
	42. Spontaneous herbaceous vegetation	420. Spontaneous herbaceous vegetation
5. Areas with no vegetation	50. Areas with no vegetation	500. Areas with no vegetation
6. Water and wetlands	61. Wetlands 62. Water	610. Wetlands 620. Water

The DGT emphasizes that COSsim is still an experimental product, and that COS must still be used as the main cartography. Nevertheless, the release of this product was extremely interesting in the context of this dissertation, since it provided an extra LULC map, obtained through similar techniques, for further evaluation of the proposed solution.

4.5 Software

During the execution of this study, multiple software and applications were used in order to reach the proposed solution. This section presents those tools and their main purposes.

4.5.1 QGIS

QGIS[3] is a free open-source GIS, which offers a variety of standard GIS functionalities and allows users to visualize and manipulate spatial information, that can be stored in vector or raster formats. It can also be integrated with various plug-ins to extend its functionalities.

In the development of this dissertation, QGIS was heavily explored, being used as a visualization tool and employing several of its raster and vector editing functions. Additionally, OTB, a remote sensing open-source project, was also used as a fully integrated QGIS plug-in. OTB has a variety of functionalities, some of which were explored such as dimensionality reduction and image segmentation.

4.5.2 Spyder

The majority of the code developed for this project was written in Python, in the Spyder IDE running with Anaconda. As this research problem deals with geospatial data, multiple libraries developed to work with such data in vector or raster format were used, as well as libraries pertaining to machine learning. The complete list of Python libraries utilized is represented in Table 4.5.

Table 4.5: Python libraries used

Libraries	Version	General purpose
rasterio	1.2.10	Geospatial raster data manipulation
fiona	1.8.20	Geospatial vector data manipulation
geopandas	0.6.1	Geospacial data analysis
pandas	1.3.0	Data analysis
xgboost	1.5.0	Classification model
scikit-learn	1.0.1	Classification model, validation and metrics

4.5.3 Google Earth Engine

Google Earth Engine (GEE) is a platform developed by Google for the analysis and visualization of geospatial datasets. It hosts satellite imagery from multiple sources dating back around 40 years, which is publicly available for consulting and downloading. One of the main advantages of GEE is the possibility to retrieve the satellite images and pre-process them in the Google servers, eliminating the need for storing the raw data locally.

[3] https://www.qgis.org/en/site/

In this dissertation, GEE served exclusively as a data acquiring and pre-processing tool, and it was utilized via the web-based IDE, Earth Engine Code Editor.[4] This IDE can be freely accessed after activation through a Google account, and allows for the development of Javascript scripts for a multitude of applications. The GEE scripts used in this dissertation were provided by the colleague André Neves, and altered to suit the needs of this research work.

4.5.4 Tableau

Tableau[5] is a data visualization and analytics platform, which makes creating visually pleasing and easily understandable charts and tables extremely simple. For this dissertation, it was used in its Desktop version to explore and understand data in depth, as well as produce various figures and tables for this document.

[4] https://code.earthengine.google.com/
[5] https://www.tableau.com/

5

Methodology

After the general plan for the execution of the proposed solution was presented, in this chapter each component of that plan is further detailed, including methodologies and technologies used, as well as any necessary implementation details.

All experiments were produced on a machine with CPU Intel(R) Core(TM) i7-8750H CPU @ 2.20GHz with 8GB RAM, HDD 931GB and SSD 477GB.

5.1 Acquiring and pre-processing the input data

As discussed before, this study aimed to create a 2018 LULC map for the Almada region. Initially, only 2018 input data was used to create the classification models, but after some experimentation it was discovered that combining both 2017 and 2018 data provided better classification results. Accordingly, the temporal window for obtaining the satellite data was set between January 2017 and December of 2018.

5.1.1 Sentinel-1

Sentinel-1 imagery is available in GEE in the 'COPERNICUS/S1_GRD' Image Collection. This collection consists of backscatter coefficient processed Level-1 Ground Range Detected. Figure 5.1 represents the full process of obtaining and processing the Sentinel-1 imagery, including GEE's pre-processing steps, implemented by the Sentinel-1 Toolbox.

First, the collection was filtered by region, to gather the images where Almada is present. Then, a date filter was applied, with the images from 2017 and 2018 being collected separately. A total of 121 images for 2017, and 120 for 2018 were used.

In order to create homogeneous groups of data, the **ascending** and **descending** orbits of each year were separated, and for each one the **'VV'** and **'VH'** polarization were selected. Subsequently, each band in each year's collection of images was reduced to its 30th, 50th and 70th percentiles. Finally, the images from the two years were stacked and all bands were resampled to the 10x10m spatial resolution, in the EPSG:4326 coordinate system. The final product downloaded from GEE was a raster image with 20 bands.

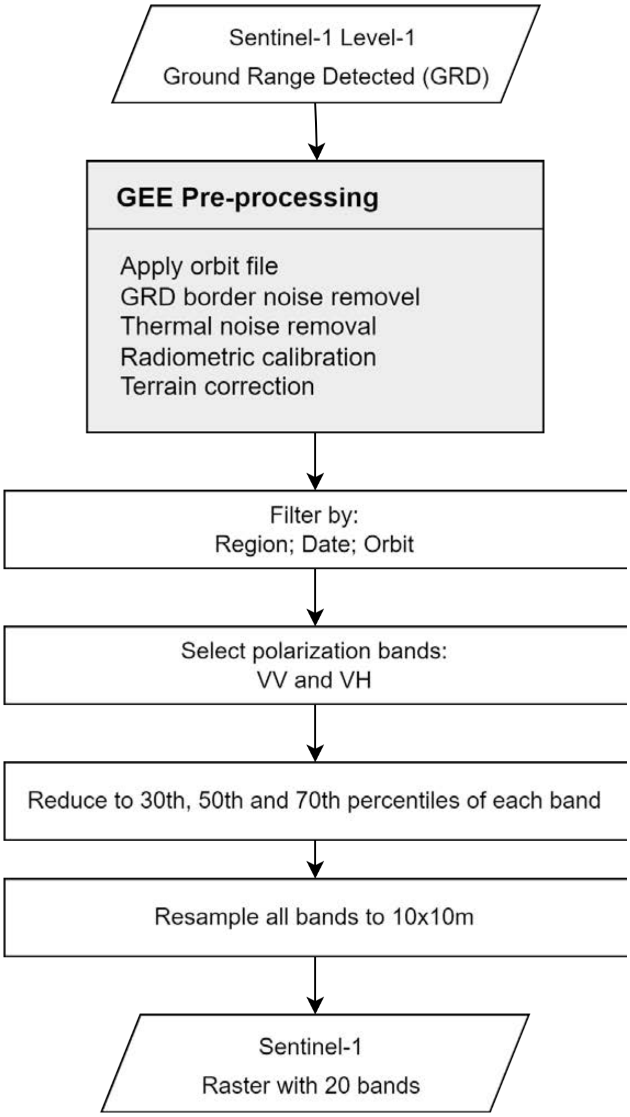

Figure 5.1: Sentinel-1 processing chain

5.1.2 Sentinel-2

Sentinel-2 imagery is available in GEE in the 'COPERNICUS/S2' and 'COPERNICUS/S2_SR' Image Collections. While 'COPERNICUS/S2' contains Level-1C, which are Top-Of-Atmosphere (TOA) products, 'COPERNICUS/S2_SR' contains Level-2A products, which are Bottom-Of-Atmosphere (BOA) corrected reflectance product, derived from the respective 1C images. In this research, only Level-2A products were utilized. Figure 5.2 represents the full process of obtaining and processing the Sentinel-2 imagery.

As with Sentinel-1 imagery, the first step was filtering the 'COPERNICUS/S2_SR' collection by region and date.

Since Sentinel-2 instruments are passive sensors, its products are affected by the weather, specifically clouds which highly influence the spectral values. As so, the collection of images of each year was filtered, and only the images with a percentage of

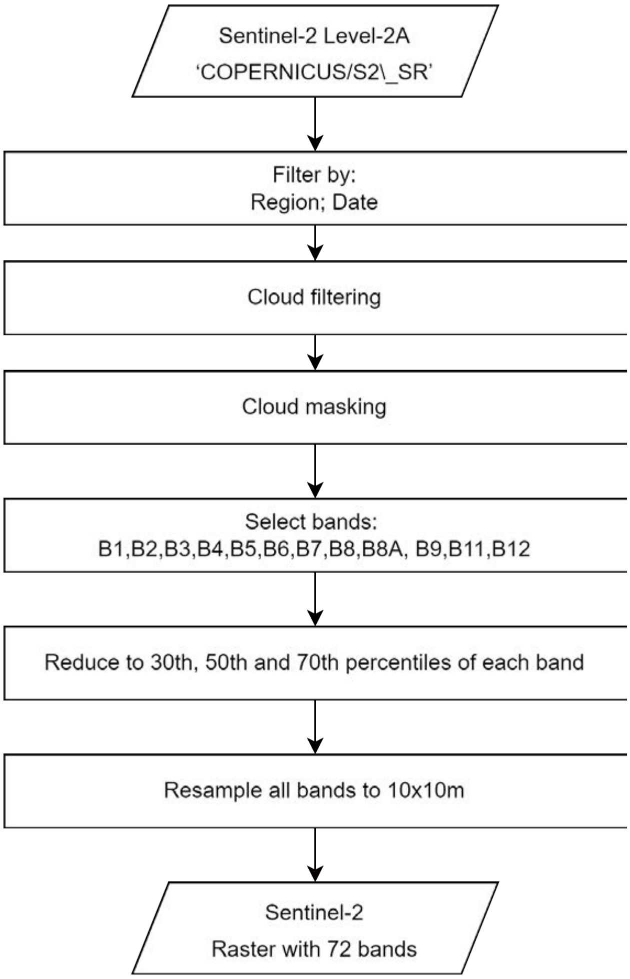

Figure 5.2: Sentinel-2 processing chain

cloudy pixels lower than 10% were kept. Following this filtering, a mask was applied over the remaining cloud pixels. Both the filtering and masking were performed using GEE functions.

For both years, all Sentinel-2 band were selected, with the exception of **B10**, and reduced to its 30th, 50th and 70th percentiles.

Finally, the images from the two years were stacked and all bands were resampled to the 10x10m spatial resolution, in the EPSG:4326 coordinate system. The final product downloaded from GEE was a raster image with 72 bands.

A total of 77 Sentinel-2 images were collected and Figure 5.3 presents the number of images obtained in each month of 2017 and 2018. The variation is due to the satellites' revisit time, as well as each months' cloud coverage which influenced the number of images deleted by the filtering. As Sentinel-2 Level-2A images have only been processed from Level-1C images starting from the 28th of March of 2017, no images were acquired from January, February and March of 2017.

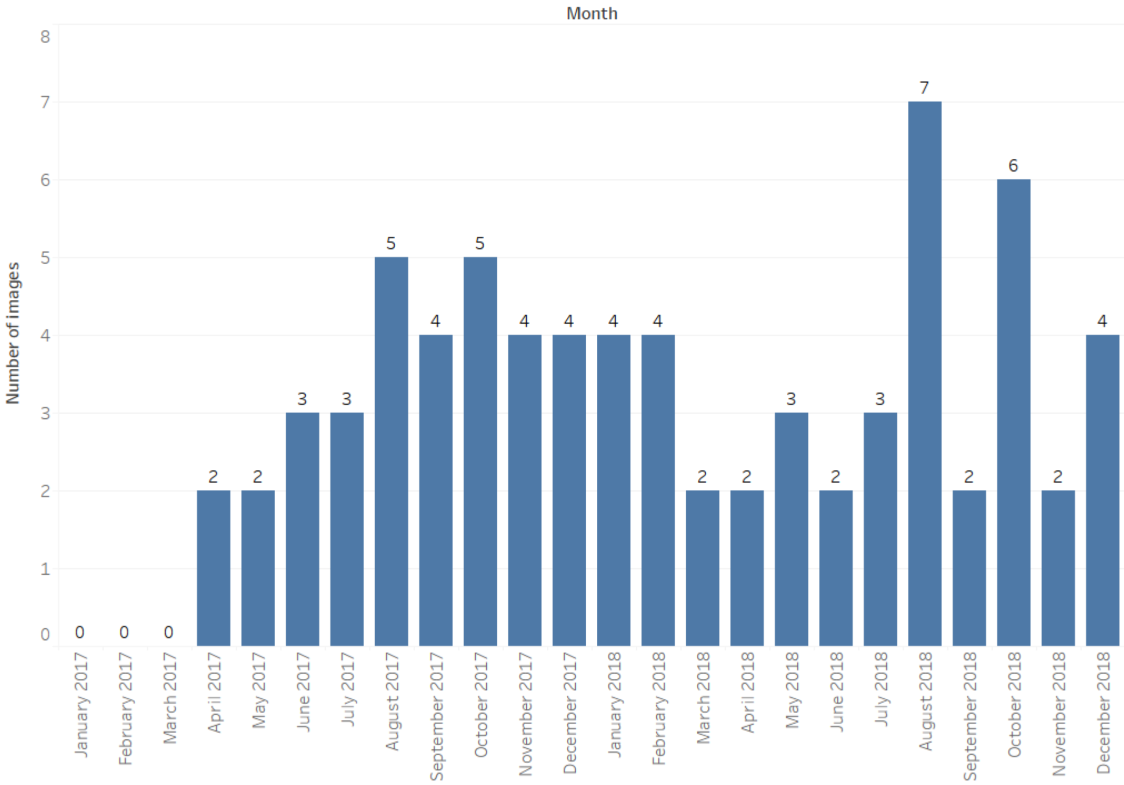

Figure 5.3: Number of Sentinel-2 images acquired per month

5.2 Creation of products derived from satellite imagery

5.2.1 Spectral Indices

The three spectral indices detailed in Chapter 2, NDVI, NDBI and BUI, were calculated using Sentinel-2 bands: **B8**, as the near-infrared band, **B4**, as the red band, and **B12**, as the short-wave infrared band.

This calculation was performed in GEE, and as with the satellite's bands, the 30th, 50th and 70th percentiles were computed from the 2017 and 2018 data.

5.2.2 Texture information

Inspired by experiments by Kupidura et al. (2019) [42], texture information was introduced in the classification models using GLCM features in conjunction with PCA. Although the authors employed only Sentinel-2 data, in this dissertation two paths were explored, using Sentinel-1 and Sentinel-2 separately. Despite the input data being different, the same process was used for both satellites, represented in Figure 5.4.

First, a PCA was performed on all image bands of each satellite, in order to obtain the first principal component, using the **DimensionalityReduction** function in OTB QGIS. In both satellites' data, this component explains over 80% of the overall variability. Then, the first component was used to extract the GLCM features, using the **HaralickTexture-Extraction** function in OTB QGIS. The utilized parameters for the extraction are present in Table 5.1.

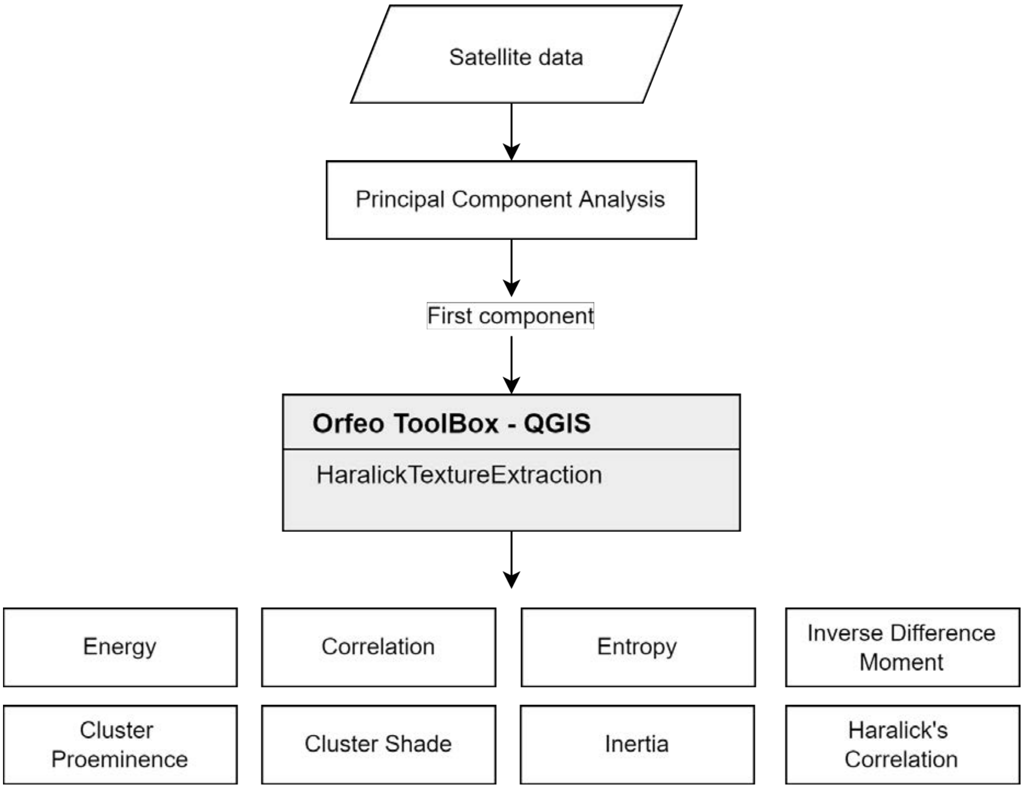

Figure 5.4: Creation of the textural features

Table 5.1: HaralickTextureExtraction parameters

Parameter	**Value**
Computational step	1
X Radius	3
Y Radius	3
X Offset	1
Y Offset	0
Histogram number of bin	16

For each satellite 8 features were computed: **Energy**, **Entropy**, **Correlation**, **Inverse Difference Moment**, **Inertia**, **Cluster Shade**, **Cluster Prominence** and **Haralick's Correlation**. Further information on the calculations of these features by OTB can be found in [52].

5.2.3 Combination of data

After collecting all satellite imagery and derived products, four sets of aggregated data were created:

- **S1+S2**;
- **S1+S2+SI**;
- **S1+S2+T1**;
- **S1+S2+T2**;

S1 represents the Sentinel-1 bands, **S2**, the Sentinel-2 bands, **SI**, the spectral indices calculated through Sentinel-2, **T1** the texture obtained through Sentinel-1 bands and **T2** the texture obtained through Sentinel-2 bands. The same notation will be used throughout this document.

5.3 Ground Truth construction

5.3.1 Manual

Even though COS is a useful tool for urban planning, when it is analysed with the help of the aerial ortophotos, it is clear that some of the methodological choices in the construction of its classes, as well as the MMU limitations, lead to a map which cannot be reliably used to automatically collect ground truth for the group of classes in this dissertation.

As such, a manual ground truth was constructed, in order to provide the classifiers with the most accurate data possible. This manual ground truth was made by inspecting the reference data: the orthophotos, as well as COS, and hand-drawing polygons in QGIS. To ensure that the models would be able to classify all the different elements within the same class, several subclasses were created using COS's Level 4 classes, which are shown in Table 5.2.

A total of 3194 polygons were drawn, covering around 14.71 km^2, approximately 21% of the study area. Table 5.3 presents the area collected for each subclass and the total of each class.

5.3.2 Semi-automatic

After some tests, a concern arose that the manually extracted polygons might not be a representative sample of the true composition of each class. Thus, an additional ground truth was created in a semi-automatic way to minimize the bias introduced by hand picking. A new version of COS, henceforth referred to as **improved COS**, was constructed based on the original map, but with some changes on the major areas with the largest incompatibilities in classification.

Table 5.2: Classes, subclasses and respective COS Level-4 classes

Class	Subclass	COS Level-4 class
1. Artificial Territories	10	1.1.1.1 Continuous urban fabric predominantly horizontal
		1.1.1.2 Continuous urban fabric predominantly vertical
	11	1.1.2.1 Discontinuous urban fabric
		1.1.2.2 Sparse discontinuous urban fabric
	12	1.2.1.1 Industrial areas
		1.2.2.1 Commercial areas
	13	1.4.1.1 Road network and associated spaces
		1.4.1.2 Rail network and associated spaces
	14	1.1.3.1 Parking areas and public spaces
		1.4.2.1 Sea and river port terminals
		1.6.1.2 Sports facilities
		1.6.2.1 Camping sites
		1.6.5.1 Other equipments and touristic facilities
2. Agriculture	20	2.2.2.1 Orchards
		2.2.3.1 Olive groves
	21	2.1.1.1 Non-irrigated and irrigated temporary crops
	22	2.3.2.1 Complex cultivation patterns
3. Other vegetation	30	6.1.1.1 Spontaneous vegetation areas with shrub coverage
		8.1.2.1 Marshes
	31	3.1.2.1 Spontaneous pastures
	32	3.1.1.1 Improved pastures
	33	1.6.1.1 Golf courses
		1.7.1.1 Parks and gardents
4. Forests	40	5.1.2.2 *Pinus pinaster* forests
	41	5.1.2.1 *Pinus pine* forests
	42	5.1.1.7 Other broadleaf forests
	43	5.1.1.5 Eucalyptus forests
	44	5.1.1.2 *Quercus rotundifolia* forests
		5.1.1.6 Forests of invasive species
5. Bare and sparsely vegetated areas	50	7.1.1.2 Beaches, dunes and coastal sand areas

Table 5.3: Area of manually selected ground truth for each subclass and class

Class	**Subclass**	**Area (in km^2)**
1. Artificial Territories	10	2.10
	11	0.50
	12	0.28
	13	0.26
	14	0.74
	Total	3.88
2. Agriculture	20	0.07
	21	1.82
	22	0.16
	Total	2.05
3. Other vegetation	30	1.45
	31	0.61
	32	0.20
	33	0.02
	Total	2.28
4. Forests	40	2.58
	41	1.86
	42	0.13
	43	0.20
	44	1.26
	Total	6.03
5. Bare and sparsely vegetated areas	50	0.47
	Total	0.47
Total		14.71

Four areas were identified:

- The Alfeite region, in Figure 5.5, with a significant section of **Forests** classified as **Artificial Territories**;
- The beach area, in which almost no artificial buildings are represented;
- Parks, classified as Level-1 **Artificial Territories** (although divided in its own Level-2 class, **Parks and Gardens**);
- Golf courses, also classified as Level-1 **Artificial Territories**, in its own Level-4 class, **Golf Courses**.

In the case of Alfeite and the beach area, QGIS was utilized to manually draw polygons and divide the classes. The parks, gardens, and golf courses were included in class **3. Other Vegetation**.

Event though the Aroeira area, in Figure 5.6 was also identified as problematic, with a significant amount of **Forests** being identified as **Artificial Territories**, the small size of the objects made the manual separation of the classes infeasible.

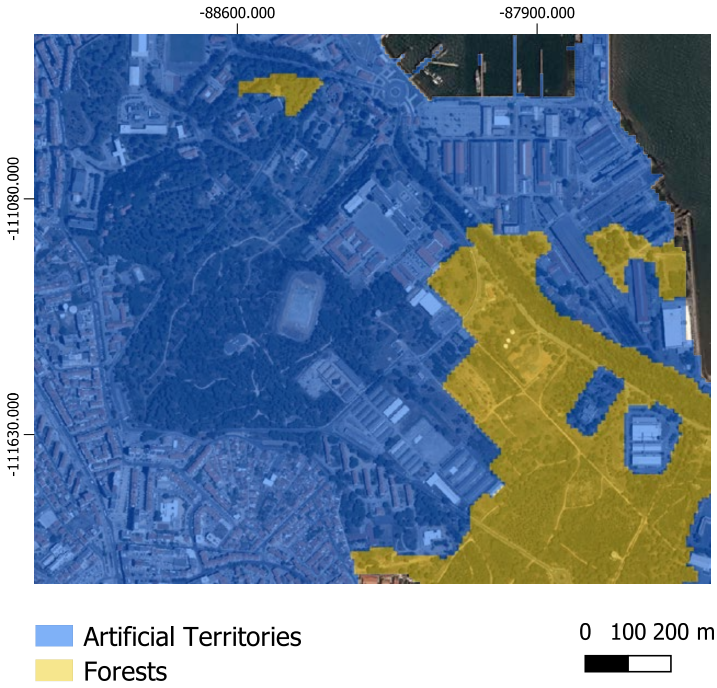

Figure 5.5: COS's classification of **Artificial Territories** and **Forests** in the Alfeite region

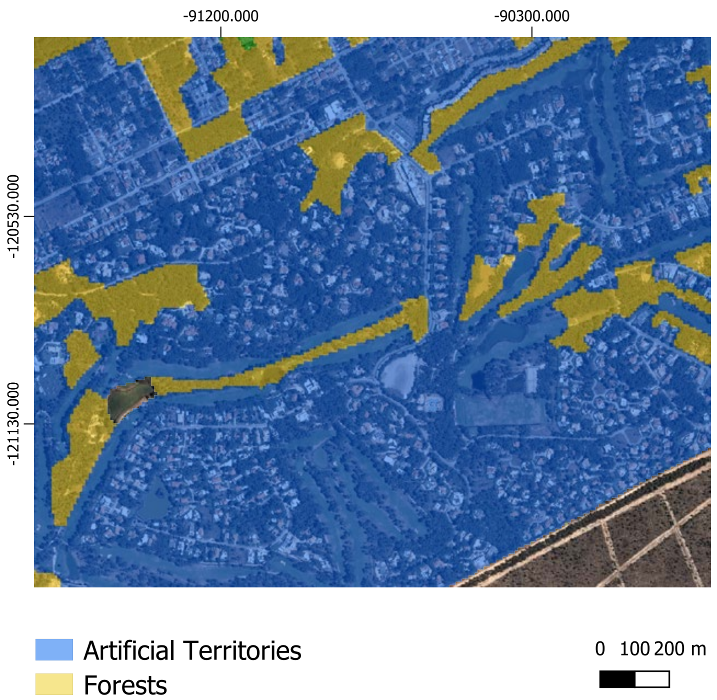

Figure 5.6: COS's classification of **Artificial Territories** and **Forests** in the Aroeira region

The same subclasses present in Table 5.2 were used to label all zones of the improved COS.

5.4 Dataset creation - PBIA

Figure 5.7 represents the pipeline of the creation of the datasets for the pixel-based experiments.

Since the basic unit of the PBIA classification is the pixel, collecting samples in this approach was done by performing a stratified (using the subclasses) random sampling of each of the two constructed ground truths. Those pixels were then used to extract the features from each set of data and create the datasets. While several datasets were created using the manual ground truth, only one was constructed for the semi-automatic, using the best combination of features obtained with the manual datasets, **S1+S2+T1**.

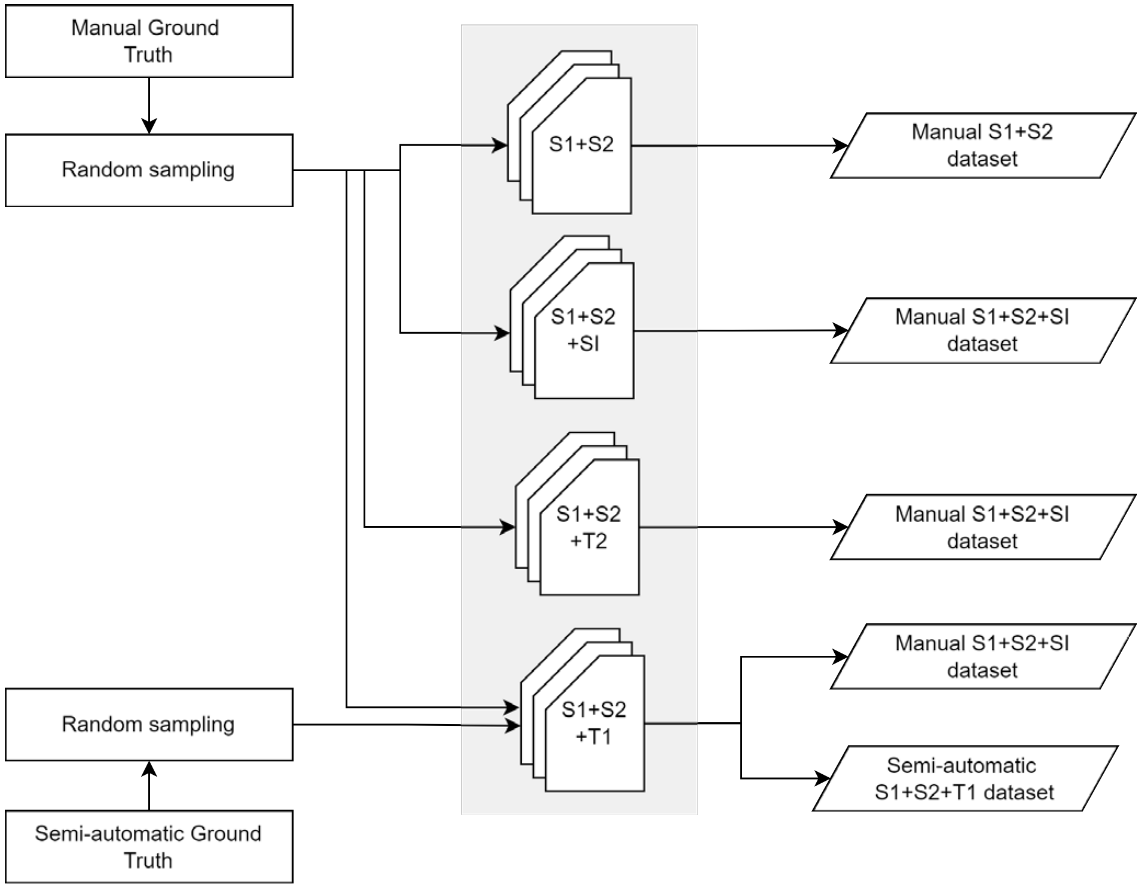

Figure 5.7: Dataset creation in the PBIA approach

Table 5.4 represents the class and subclass composition of the datasets created. There was an attempt to maintain the proportions of the classes, which was difficult since the manual selection of **Artificial Territories** was extremely laborious. Each dataset is composed of 120885 pixels (12.09 km^2), representing approximately 16,9% of the full area.

Table 5.4: Class composition of PBIA datasets

Class	Subclass	Number of pixels
1. Artificial Territories	10	26964
	11	6381
	12	3357
	13	3287
	14	9396
	Total	49585 (41.02%)
2. Agriculture	20	646
	21	15919
	22	1435
	Total	18000 (14.89%)
3. Other vegetation	30	10160
	31	4278
	32	1398
	33	164
	Total	16000 (13.24%)
4. Forests	40	13667
	41	9846
	42	699
	43	1084
	44	6704
	Total	32000 (26.47%)
5. Bare and sparsely vegetated areas	50	5300
	Total	5300 (4.38%)
Total		120885 (100.00%)

5.5 Image Segmentation

Achieving good image segmentation is essential in OBIA classification and there are three components that greatly influence this process: the data, the segmentation algorithm and its parameters, and the segmentation evaluation.

5.5.1 Segmentation algorithm

As detailed previously, the segmentation algorithm used in this dissertation was Mean-Shift segmentation, implemented in OTB in the **LargeScaleMeanShift** function, which has three parameters: spatial radius, range radius, and minimum segment size. The minimum size was set at 4 pixels, meaning that an object on the ground has to have an area of at least 200 m^2 in order to not be absorbed into other elements. The spatial and range radius have a great influence on the quality of the segmentation and, as such, a wide range of combinations was tested and evaluated, with the results being presented in Chapter 7.

5.5.2 Data

The first experiments of segmentation were performed on a composite of the bands with the highest spatial resolution (10m) in Sentinel-2: band 2, **Blue**; band 3, **Green**; band 4, **Red**; and band 8, **NIR**. The Sentinel-2 data was obtained in an identical process as the one mentioned in section 5.1.2, with the only exception being the calculated percentiles, which were the 25th, 50th and 75th.

After some experimentation with segmentation evaluation, it was decided that due to the high number of bands (12), a PCA would be applied to the Sentinel-2 composite in order to reduce the dimensionality of the data. Only the 5 first principal components were kept and used for the segmentation, explaining approximately 99% of the overall variability.

Combinations of Sentinel-2 images with other sources of data, such as Sentinel-1 imagery and texture features, were also tested, but later abandoned as the visual inspection suggested that the additional bands were creating confusion in the segmentation algorithm, and produced inferior segmentations.

5.5.2.1 Segmentation Evaluation

As observed in the state-of-the-art review, the process and metrics to evaluate segmentations, specifically in unsupervised approaches, are still highly debated.

For this dissertation, the metrics proposed by Espindola et al. [21], area-weighted variance (WV) and Moran's I Index (MI), without the computation of Global Score, were chosen to evaluate the segmentations produced, complemented by visual analysis. Each index was calculated for each band (principal component) of the composite, and analyzed separately.

An R script was developed to calculate the WV and MI, using two libraries, **raster** and **spdep**, to read the shapefiles containing each segmentation, and to obtain the neighbors of each segment for the calculation of MI.

5.5.3 Spatial Geometric Attributes

One advantage of the OBIA approach is the possibility to use geometric attributes of the segments, in addition to their spectral properties.

In this dissertation three spacial attributes were calculated:

- **Area**: obtained by the number of pixels;

- **Rectangularity**: calculated by dividing the area of each segment by the area of its smallest bounding box;

- **Compactness**: calculated using a commonly used test, Polsby-Popper, developed for calculating compactness of political districs [59]:

$$C = \frac{4 \cdot a \cdot \pi}{p^2}, \tag{5.1}$$

where a and p represent the area and perimeter of each segment

5.6 Dataset creation - OBIA

Figure 5.8 represents the pipeline of the creation of the datasets for the object-based experiments. In this approach, only the manual ground truth was used.

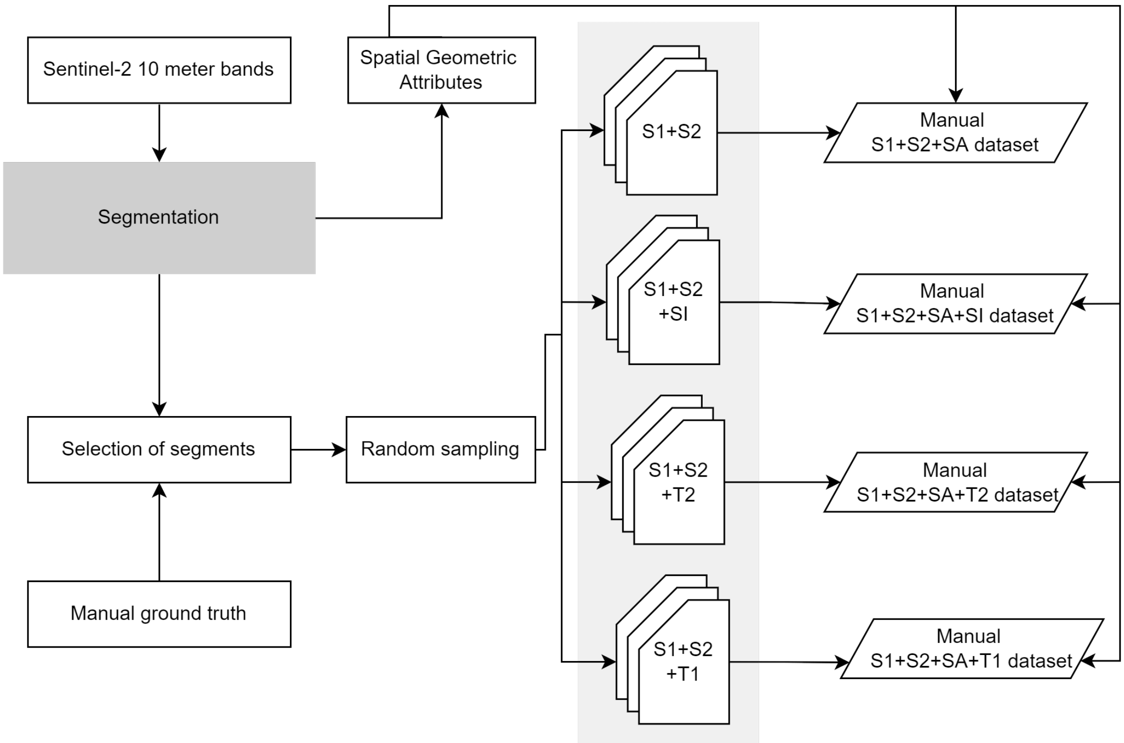

Figure 5.8: Dataset creation in the OBIA approach

The segmentation step performed on Sentinel-2 data produced objects, which are the unit of classification in this approach. Each object was intersected with the ground truth polygons and assigned the class of the polygon with the largest area of intersection. Since the ground truth does not cover the entire region of study, only segments with a coverage higher than 50% were selected, in order to avoid choosing segments with small areas of intersection, which could be due to poor segmentation quality.

Subsequently the segments were randomly selected using stratification (using the subclasses) and used to extract the features from each set of aggregated data: the average value of each band inside the segment. The datasets were created by combining these features and the spatial geometric attributes of the objects.

Table 5.5 presents the number of segments collected for each class and subclass. A total of 5152 segments were obtained, representing 7.9% of the total number of segments obtained, 65519.

Table 5.5: Class composition of OBIA datasets

Class	Subclass	Number of pixels
1. Artificial Territories	10	26964
	11	6381
	12	3357
	13	3287
	14	9396
	Total	49585 (41.02%)
2. Agriculture	20	646
	21	15919
	22	1435
	Total	18000 (14.89%)
3. Other vegetation	30	10160
	31	4278
	32	1398
	33	164
	Total	16000 (13.24%)
4. Forests	40	13667
	41	9846
	42	699
	43	1084
	44	6704
	Total	32000 (26.47%)
5. Bare and sparsely vegetated areas	50	5300
	Total	5300 (4.38%)
Total		5152 (100.00%)

5.7 Classification

The process of building the classification models for each dataset and classifier is described in this section.

First, the dataset was divided into training and test sets by performing an 80/20 split.

Since both XGB and RF have several hyperparameters which must be tuned in order to obtain the best possible results, the training set was further divided with a second 80/20 split, creating the smaller validation set.

Validation was performed using sklearn's **RandomizedSearchCV** with 40 iterations. This function uses the training set to train the network with multiple parameter combination (sampled from a given distribution), and chooses the best by evaluating with the validation set. Although it would have been interesting to test other validation methods, such as stratified k-fold cross validation, the amount of experiments and the computation time did not allow for that.

Table 5.6 presents the python libraries for the classifiers used, as well as the hyperparameters optimized in the validation stage and the corresponding distributions searched.

Table 5.6: Hyperparameters optimized for each classifier

Classifier	Python library	Hyperparameters
XGB	xgboost	**n_estimators**: [100,200,300,400,500,600] **max_depth**: [3,4,5,6,8] **learning_rate**: [0.01,0.05,0.1,0.15,0.2,0.25,0.3] **gamma**: [0,0.2,0.3,0.4,0.5]
RF	sklearn.ensemble. RandomForest- Classifier	**n_estimators**: [100,200,300,400,500,600] **max_depth**: [5,10,15,20,25] **max_features**: ['auto', 'sqrt']

After validation, the model was retrained using the training data and the best hyperparameter combination found, and the test set was used to provide an unbiased evaluation of the model.

5.8 Final list of experiments

Table 5.7 and 5.8 present a detailed view of all classification models developed during this dissertation. For both approaches and classifiers, the datasets created were tested in their entirety, using all the calculated percentiles for each band in Sentinel-1, Sentinel-2 imagery and for the spectral indices, and truncated, using only the 50th percentile of those products' bands.

In the OBIA approach, an additional experiment was performed using the best performing dataset up to that point, **S1+S2+SA+T2**, with the exclusion of the spatial geometric attributes (**SA**).

5.9 Full map classifications

The final step of this research was assessing the performance of the best classification models of the PBIA and OBIA approaches, when creating the full 2018 LULC maps for the region of Almada. These maps, henceforth refered to as **PBIA_map** and **OBIA_map** can be consulted in Appendix A.

In order to evaluate the quality of these maps, each of them was compared with the two available LULC maps, COS and COSsim and a two part review was conducted: a quantitative analysis, in which the kappa, and comission and omission errors were calculated; and a qualitative analysis, developed via visual analysis.

Table 5.7: PBIA approach experiments

Input data	Percentiles	Ground truth	Classifier
S1+S2	30th, 50th, 70th	manual	XGB
S1+S2	30th, 50th, 70th	manual	RF
S1+S2+SI	30th, 50th, 70th	manual	XGB
S1+S2+SI	30th, 50th, 70th	manual	RF
S1+S2+T1	30th, 50th, 70th	manual	XGB
S1+S2+T1	30th, 50th, 70th	manual	RF
S1+S2+T2	30th, 50th, 70th	manual	XGB
S1+S2+T2	30th, 50th, 70th	manual	RF
S1+S2	50th	manual	XGB
S1+S2	50th	manual	RF
S1+S2+SI	50th	manual	XGB
S1+S2+SI	50th	manual	RF
S1+S2+T1	50th	manual	XGB
S1+S2+T1	50th	manual	RF
S1+S2+T2	50th	manual	XGB
S1+S2+T2	50th	manual	RF
S1+S2+T1	30th, 50th, 70th	semi-automatic	XGB

Table 5.8: OBIA approach experiments

Input data	Percentiles	Ground truth	Classifier
S1+S2+SA	30th, 50th, 70th	manual	XGB
S1+S2+SA	30th, 50th, 70th	manual	RF
S1+S2+SA+SI	30th, 50th, 70th	manual	XGB
S1+S2+SA+SI	30th, 50th, 70th	manual	RF
S1+S2+SA+T1	30th, 50th, 70th	manual	XGB
S1+S2+SA+T1	30th, 50th, 70th	manual	RF
S1+S2+SA+T2	30th, 50th, 70th	manual	XGB
S1+S2+SA+T2	30th, 50th, 70th	manual	RF
S1+S2+SA	50th	manual	XGB
S1+S2+SA	50th	manual	RF
S1+S2+SA+SI	50th	manual	XGB
S1+S2+SA+SI	50th	manual	RF
S1+S2+SA+T1	50th	manual	XGB
S1+S2+SA+T1	50th	manual	RF
S1+S2+SA+T2	50th	manual	XGB
S1+S2+SA+T2	50th	manual	RF
S1+S2+T2	30th, 50th, 70th	manual	XGB

Two LULC maps can only be compared if they share the same classes and, as such, some modifications were required in COS and COSsim. Since the Level-1 classes of COSsim are extremely similar to this dissertation's chosen classes, they were maintained, with the only modification being the merging of Level-2 class **Wetlands** into the Level-1 **Shrub and spontaneous herbaceous vegetation**, correspondent to this dissertation's **3. Other Vegetation**.

As for COS, the Level-1 classes were maintained, with the only modification being the combination of Level-1 classes **Pastures**, **Spontaneous vegetation areas with shrub coverage** and **Wetlands** to represent the equivalent of this dissertation's **3. Other Vegetation**.

6

Results - Pixel Based Approach

This chapter contains all the discussions concerning the pixel-based approach. Firstly, the experiments using the manual datasets are presented, and the effect of the different combinations of features are discussed. Secondly, the results of the two methodologies of ground truth creation are compared. Finally, a thorough comparison between the map obtained by the best classification model, **PBIA_map**, and COS and COSsim is produced.

All coordinates are presented in the EPSG:3763 Coordinate System.

6.1 Experiments using the manual datasets

The kappa values for the first experiments using the manual datasets, with all percentiles, are presented in Figure 6.1.

	XGB	RF
SI+S2	0,99362	0,98075
SI+S2+SI	0,99282	0,97977
SI+S2+T1	0,99437	0,98075
SI+S2+T2	0,99362	0,98115

Table 6.1: Kappa values per classifier and set of input data - all percentiles

XGB is the classifier with the highest kappa in all experiments, with the input data combination **S1+S2+T1** having the best performance out of all the experiments. Despite being consistently lower by at least 1%, RF also reaches excellent results.

The presence of spectral indices produce a small decrease in classification performance, creating the worse models for each classifier. As for the textural attributes, **T1** very slightly improved the classification when the XGB classifier was used, while **T2** slightly improved the model using RF.

Analysing Table 6.2, which presents the F1 score, precision and recall of each class, for each experiment using XGB, it's possible to see that class **3. Other vegetation** is consistently the one with the lowest results (albeit still excellent), in particular recall, followed by **2. Agriculture**.

		XGB		
Dataset	Class	F1 Score	Precision	Recall
SI+S2	1	0,99813	0,99798	0,99829
	2	0,99361	0,99361	0,99361
	3	0,98765	0,98842	0,98688
	4	0,99586	0,99563	0,99609
	5	0,99670	0,99717	0,99623
SI+S2+SI	1	0,99788	0,99808	0,99768
	2	0,99278	0,99196	0,99361
	3	0,98591	0,98808	0,98376
	4	0,99532	0,99438	0,99625
	5	0,99717	0,99717	0,99717
SI+S2+T1	1	0,99834	0,99839	0,99829
	2	0,99473	0,99390	0,99556
	3	0,98889	0,99090	0,98688
	4	0,99617	0,99563	0,99672
	5	0,99764	0,99717	0,99811
SI+S2+T2	1	0,99839	0,99829	0,99849
	2	0,99319	0,99361	0,99278
	3	0,98624	0,98747	0,98500
	4	0,99617	0,99547	0,99687
	5	0,99811	0,99811	0,99811

Table 6.2: XGB Metric results for each dataset - all percentiles

The presence of the spectral indices has a negative effect on all classes' F1 score, except **5. Bare and sparsely vegetated land**, which is very slightly improved. As for the textural features, **T1** has a slight positive effect on the F1 score of all classes.

The confusion matrices for **S1+S2**, in Table 6.3, and **S1+S2+T1**, in Table 6.4, show that the textural features were particularly useful in clearing up some confusion between classes, **3. Other Vegetation** and **4. Forests**, AND **1. Artificial Territories** and **5. Bare and sparsely vegetated areas**.

	True Class				
Predicted Class	1	2	3	4	5
1	9 900	7	4	5	4
2	4	3 577	16	3	0
3	6	15	3 159	16	0
4	5	1	22	6 374	0
5	2	0	0	0	1 056

Table 6.3: XGB Confusion matrix for **S1+S2** - all percentiles

	True Class				
Predicted Class	1	2	3	4	5
1	9 900	3	5	6	2
2	6	3 584	15	1	0
3	4	12	3 159	13	0
4	5	1	22	6 378	0
5	2	0	0	1	1 058

Table 6.4: XGB Confusion matrix for **S1+S2+T1** - all percentiles

Regarding the RF experiments, in Table 6.5, the class with the lowest results is, again, **3. Other Vegetation**, followed by **2. Agriculture**. As with the previous classifier, the spectral indices decrease the F1 score of all classes, except **5. Bare and sparsely vegetated areas**. The benefits of using XGB over RF are felt mostly in **2. Agriculture**, **3. Other Vegetation** and **4. Forests**, the three most spectrally similar classes.

The results of the second round of experiments, using the truncated manual sets with only the 50th percentile are represented in Table 6.6. All results are lower than the respective counterparts of Table 6.1, with XGB being again the highest performing classifier. Once more, the presence of spectral indices decreased the kappa in both classifiers. In RF both textural features improved the performance with **T2** being the best; while in XGB, **T2** had a small positive effect and **T1** produced a slight decrease in kappa.

		RF		
Dataset	Class	F1 Score	Precision	Recall
SI+S2	1	0,99617	0,99497	0,99738
	2	0,97869	0,97518	0,98222
	3	0,95691	0,96713	0,94689
	4	0,98814	0,98645	0,98984
	5	0,99291	0,99526	0,99057
SI+S2+SI	1	0,99602	0,99547	0,99657
	2	0,97732	0,97302	0,98167
	3	0,95570	0,96467	0,94689
	4	0,98713	0,98551	0,98875
	5	0,99291	0,99526	0,99057
SI+S2+T1	1	0,99632	0,99557	0,99708
	2	0,97895	0,97624	0,98167
	3	0,95665	0,96563	0,94783
	4	0,98768	0,98553	0,98984
	5	0,99433	0,99621	0,99245
SI+S2+T2	1	0,99602	0,99447	0,99758
	2	0,97991	0,97734	0,98250
	3	0,95807	0,96691	0,94939
	4	0,98814	0,98691	0,98937
	5	0,99337	0,99715	0,98962

Table 6.5: RF Metric results for each dataset - all percentiles

	XGB	RF
S1+S2	0,98937	0,97281
S1+S2+SI	0,98708	0,97143
S1+S2+T1	0,98845	0,97310
S1+S2+T2	0,99046	0,97482

Table 6.6: Kappa values per classifier and set of input data - 50th percentile

The reduction in percentiles had the highest negative impact in class **3. Other Vegetation**, followed by **2. Agriculture**, as can be seen in Table 6.7 and 6.8. This difference was more substantial in the RF classifiers.

		XGB		
Dataset	Class	F1 Score	Precision	Recall
S1+S2	1	0,99773	0,99798	0,99748
	2	0,98865	0,98538	0,99194
	3	0,97775	0,98082	0,97470
	4	0,99250	0,99250	0,99250
	5	0,99764	0,99717	0,99811
S1+S2+SI	1	0,99738	0,99768	0,99708
	2	0,98409	0,98016	0,98806
	3	0,97284	0,97790	0,96782
	4	0,99180	0,99095	0,99266
	5	0,99764	0,99811	0,99717
S1+S2+T1	1	0,99778	0,99788	0,99768
	2	0,98739	0,98480	0,99000
	3	0,97538	0,97922	0,97157
	4	0,99196	0,99126	0,99266
	5	0,99670	0,99717	0,99623
S1+S2+T2	1	0,99778	0,99768	0,99788
	2	0,99015	0,98919	0,99111
	3	0,97963	0,98271	0,97657
	4	0,99383	0,99313	0,99453
	5	0,99623	0,99529	0,99717

Table 6.7: XGB Metric results for each dataset - 50th percentile

To sum up, despite all classification models achieving outstanding results, some clear conclusions can be derived.

The use of spectral indices for this group of classes in this region was unsuccessful, as deterioration of metrics happened in all models they were present in.

Textural features had mostly a positive or neutral effect on classification kappa, although no specific pattern could be detected when comparing the experiments. Both **T1** and **T2** integrated the models with the highest kappa, the former in the XGB and the latter in the RF experiments.

		RF		
Dataset	Class	F1 Score	Precision	Recall
S1+S2	1	0,99562	0,99447	0,99677
	2	0,96884	0,96169	0,97611
	3	0,93687	0,95402	0,92034
	4	0,98271	0,97936	0,98609
	5	0,99337	0,99715	0,98962
S1+S2+SI	1	0,99552	0,99476	0,99627
	2	0,96740	0,96209	0,97278
	3	0,93393	0,94992	0,91846
	4	0,98156	0,97723	0,98594
	5	0,99243	0,99526	0,98962
S1+S2+T1	1	0,99592	0,99487	0,99697
	2	0,96959	0,96505	0,97417
	3	0,93687	0,95166	0,92252
	4	0,98201	0,97858	0,98547
	5	0,99717	0,99811	0,99623
S1+S2+T2	1	0,99582	0,99427	0,99738
	2	0,97289	0,97694	0,97694
	3	0,94187	0,95800	0,92627
	4	0,98319	0,97938	0,98703
	5	0,99291	0,99526	0,99057

Table 6.8: RF Metric results for each dataset - 50th percentile

The inclusion of the bands' 30th and 70th percentiles, as well as the utilization of classifier XGB provided a considerable improvement in kappa values, and particularly benefited the three most spectrally similar, and as such, harder to separate, classes: **2. Agriculture**, **3. Other Vegetation** and **4. Forests**.

The best overall classification model was obtained using **S1+S2+T1** with all percentiles, with XGB.

6.2 Experiment using the semi-automatic dataset

The best combination of data **S1+S2+T1** with the three percentiles was used to train and test a XGB model, using the semi-automatic ground truth.

The new model obtained a kappa of **0.87080**, a good result, albeit significantly lower than the one previously obtained for the manual dataset, **0.99437**. Observing Table 6.9, it is possible to see that the classes with the worst performances are again, **3. Other Vegetation** and **2. Agriculture**.

		XGB		
Dataset	Class	F1 Score	Precision	Recall
S1+S2+T1	1	0,9318	0,9196	0,9443
	2	0,8874	0,9017	0,8736
	3	0,8700	0,9065	0,8363
	4	0,9139	0,9065	0,9214
	5	0,9554	0,9609	0,9500

Table 6.9: XGB Metric results for **S1+S2+T1** - all percentiles and semi-automatic

The confusion matrix in Table 6.10 shows that, in addition to the expected confusion between classes 2, 3 and 4, some confusion exists when separating **1. Artificial Territories** from the nature classes, especially **4. Forests**. Since the previous results suggested that these classes are highly separable, this is likely an indication that either the semi-automatic test set's ground truth is not completely accurate, and/or the model has learned to adapt to some of the errors in the training set's ground truth and is producing misclassifications.

	True Class				
Predicted Class	1	2	3	4	5
1	9 365	249	239	305	26
2	153	3 145	115	74	1
3	78	88	2 677	106	4
4	305	118	163	5 896	22
5	16	0	7	18	1 007

Table 6.10: XGB Confusion matrix for **S1+S2+T1** -all percentiles and semi-automatic

The same model was used to test the manual test sets, the results of which can be observed in Table 6.11 and 6.12. The kappa value of this experiment was **0.98448**, and all metrics were lower than the the ones previously obtained by the model trained on the manual samples, shown in Table 6.2. Again, class **1. Artificial Territories**, one of the consistently best performing in the previous section, shows some added confusion with the natural classes.

		XGB		
Dataset	Class	F1 Score	Precision	Recall
S1+S2+T1	1	0,99451	0,99286	0,99617
	2	0,98506	0,99018	0,98000
	3	0,97498	0,98844	0,96189
	4	0,99107	0,98473	0,99750
	5	0,99483	0,99157	0,99811

Table 6.11: XGB Metric results for **S1+S2+T1** - all percentiles and semi-automatic training, tested on manual test set

	True Class				
Predicted Class	1	2	3	4	5
1	9 879	30	34	6	1
2	4	3 528	31	0	0
3	7	19	3 079	10	0
4	18	23	57	6 383	1
5	9	0	0	0	1 058

Table 6.12: XGB Confusion matrix for **S1+S2+T1** - all percentiles and semi-automatic training, tested on manual test set

These results suggest that the model built with the semi-automatic dataset is likely adapting to errors in the training ground truth, which lead to incorrect classifications. To fully verify this claim, the semi-automatic and manual models were used to create the Almada full map, and a visual analysis was produced.

In general, the semi-automatic map is extremely similar to the map which produced its ground truth, **improved COS**. However, it is clear that the manual classifier is able to produce a much more detailed and accurate map, especially in class **1. Artificial Territories**, examples of which can be seen in Figure 6.1 and 6.2.

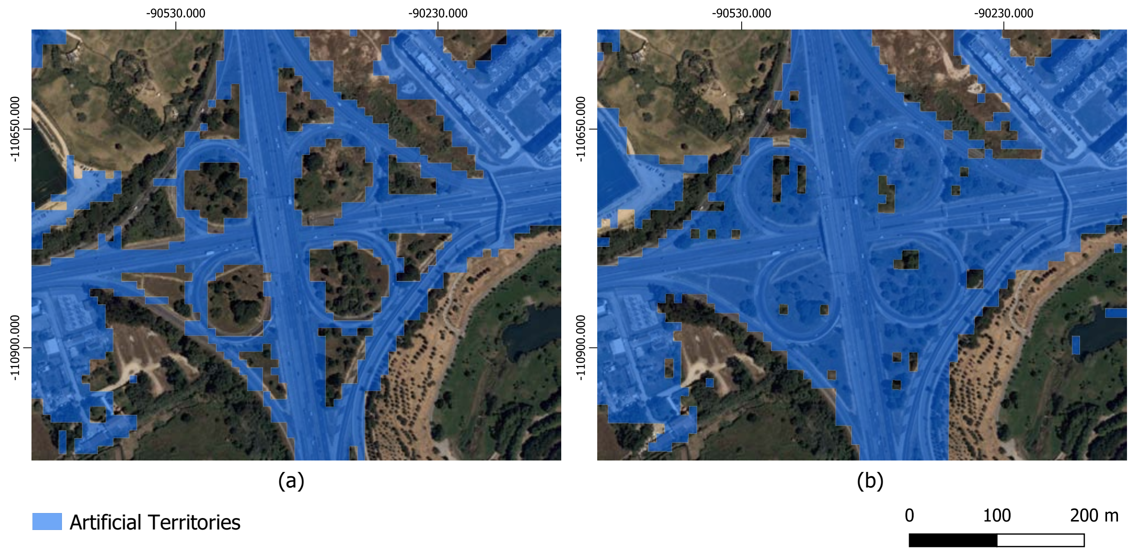

Figure 6.1: Classification examples of the **manual map** (a) and **semi-automatic map** (b) with ortophoto background. The **manual map** is able to delineate **1. Artificial Territories** with very high precision, as opposed to the **semi-automatic map**, which is unable to separate most of the vegetation from the highway.

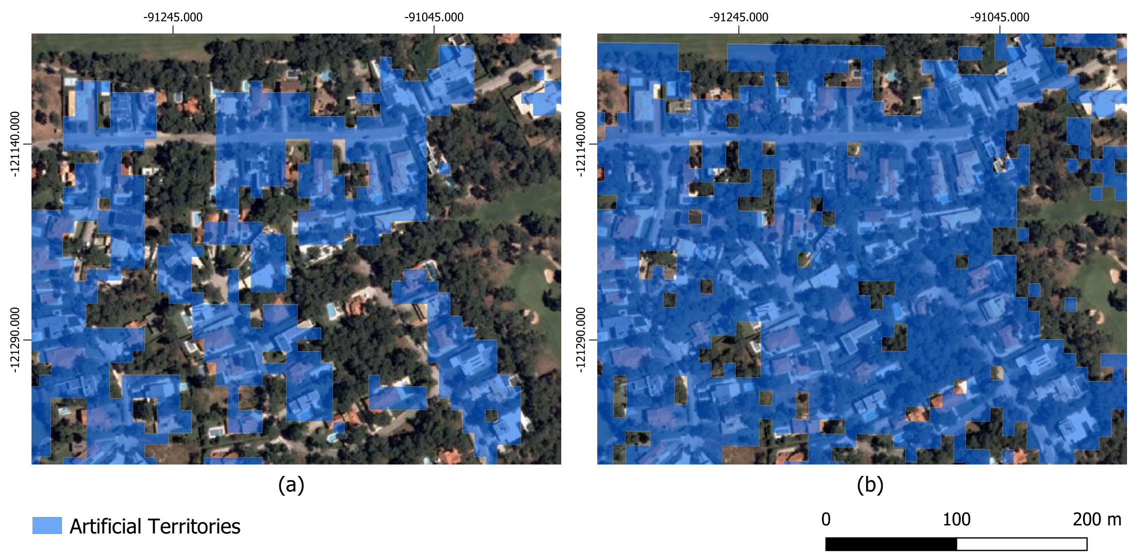

Figure 6.2: Classification examples of the **manual map** (a) and **semi-automatic map** (b) with ortophoto background. The **manual map** is able to identify small houses with very high precision, as opposed to the **semi-automatic map**, which classifies a substantial amount of vegetation as **1. Artificial Territories**.

When comparing the manual and the semi-automatic map, the latter suffers from less of the "salt-and-pepper" effect, but at the expense of high accuracy in classification.

In conclusion, the utilization of an automatic way of collecting ground truth through COS, even with manual improvements, produced a map with a lower degree of precision and accuracy than the one produced by the manual ground truth. These results are in line with the ones obtained by Varga et al. [72]. In this article, the authors proposed to confirm whether CLC Level-1 categories could be confirmed by spectral values, using Sentinel-2, Landsat-8 and PlanetScope Images, and RF and Linear Discriminant Analysis. Despite concluding that CLC polygons hold, in general, relevant information about land cover, the authors question the validity of using this map as ground truth for classification, due to the number of issues it possesses. This is exactly the problem encountered multiple times during this dissertation. COS polygons, although correct in general, suffer from a lot of intra-polygon class variance, which makes the collection of ground truth and the evaluation of the results extremely challenging.

6.3 Comparison with available LULC maps

In this subsection, the full map produced by the best model: manual ground truth, **S1+S2+T1** input data with all percentiles and XGB classifier, designated **PBIA_map**, was compared against COS and COSsim. The metrics, kappa, omission and comission errors, as well as the confusion matrix are presented first, followed by the results of the visual analysis in QGIS.

6.3.1 Carta de Uso e Ocupação do Solo (COS)

The kappa value obtained from the comparison of **PBIA_map** and COS was **0.6360**, normally considered a moderate to substantial agreement. Analysing Table 6.13, it is possible to observe that classes **2. Agriculture** and **3. Other vegetation** have the highest amount of errors, while **1. Artificial Territories** is the class with the highest performance. As expected, these results follow the pattern observed in the test set results.

	Comission Errors (%)	Omission Errors (%)
1. Artificial Territories	7,92	22,98
2. Agriculture	37,64	36,13
3. Other Vegetation	63,03	23,50
4. Forests	23,23	22,80
5. Bare and sparsely vegetated areas	17,89	16,54

Table 6.13: Comission and omission errors in **PBIA_map** using COS as reference.

In order to thoroughly understand the errors identified in **PBIA_map**, a detailed visual analysis for each class was constructed, with the support of the confusion matrix, presented in Table 6.14.

	True Class				
Predicted Class	1	2	3	4	5
1	41,83	1,11	0,73	1,51	0,25
2	2,89	7,48	0,56	1,02	0,04
3	4,70	2,77	6,03	2,79	0,02
4	4,58	0,34	0,51	18,26	0,09
5	0,31	0,02	0,05	0,07	2,03

Table 6.14: Area-based (% of total area) confusion matrix of **PBIA_map** using COS as reference.

6.3.1.1 Artificial Territories

In **1. Artificial Territories**, a significant part of errors (specifically omission errors) occur due to some of the problematic areas identified in Chapter 5: the Alfeite and Aroeira region, parks and golf courses. Most of these areas are, in fact, well classified in **PBIA_map**, as can be seen in Figure 6.3, which represents a portion of the Aroeira area, and in Figure 6.4. These examples show that **PBIA_map** is able to perform good delineation of **1. Artificial Territories**, even when the elements on the ground are small.

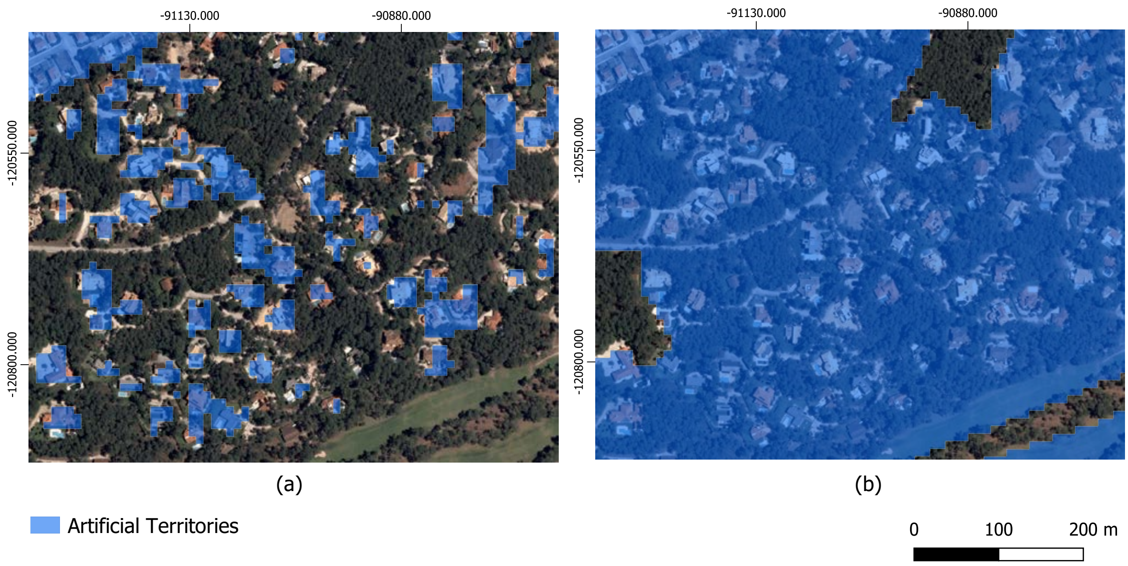

Figure 6.3: Classification examples of **PBIA_map** (a) and COS (b) with ortophoto background. **PBIA_map** is able to identify and delineate the small houses with higher precision than COS.

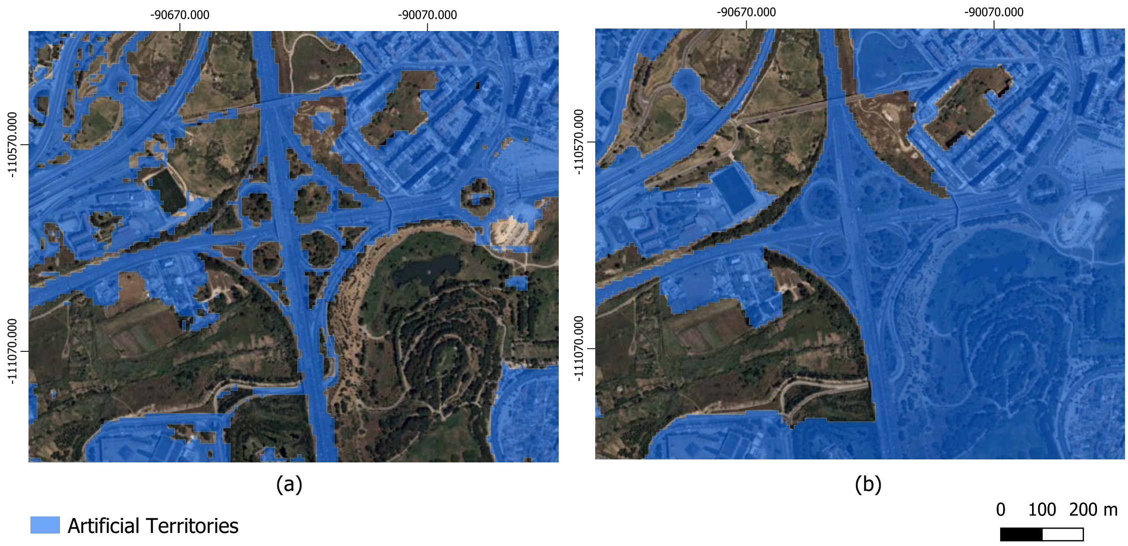

Figure 6.4: Classification examples of **PBIA_map** (a) and COS (b) with ortophoto background. **PBIA_map** is able to identify and delineate the highways with higher precision than COS.

PBIA_map is also able to correctly classify some roads and small buildings not represented in COS, an example of which can be seen in Figure 6.5.

Figure 6.5: Classification examples of **PBIA_map** (a) and COS (b) with ortophoto background. **PBIA_map** is able to classify small roads and buildings, not represented in COS.

On the other hand, an issue was identified with the boundaries of this class, which seem to be slightly shifted and/or overestimated. A probable explanation for the shifting effect is misalignment of the satellite images. As for the small overestimation, since the region (and dataset) was dominated by **1. Artificial Territories**, and the border pixels are a mixture of two or more classes, it is possible that even pixels with a very small amount of artificial structures get categorized as such, inflating the edges.

In addition, there is an area, represented in Figure 6.6, which is unexpectedly misclassified in **PBIA_map** as **1. Artificial Territories**, instead of **3. Other Vegetation**.

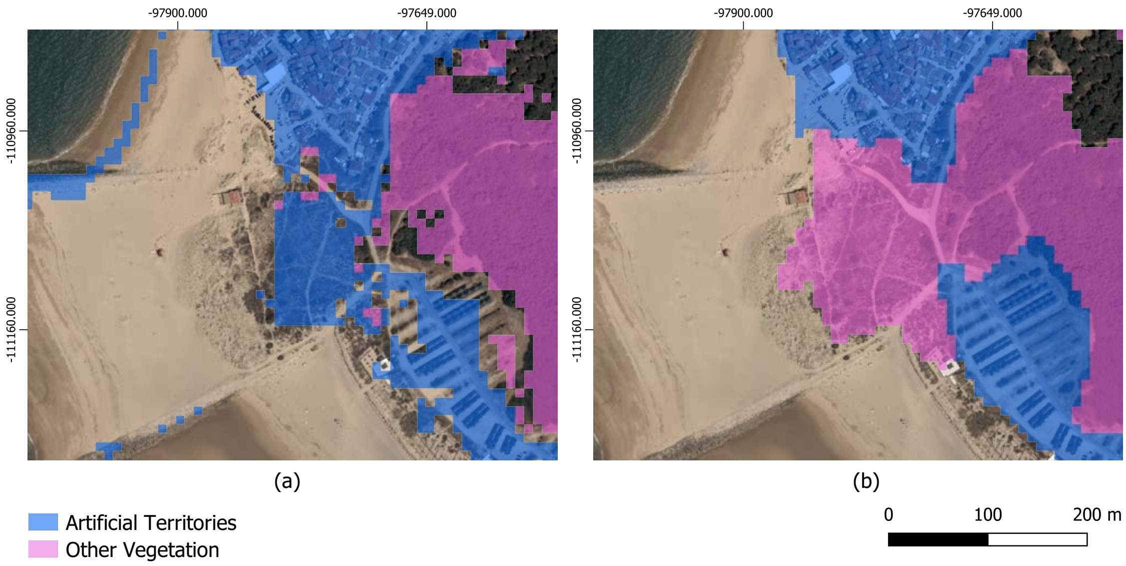

Figure 6.6: Classification examples of **PBIA_map** (a) and COS (b) with ortophoto background. **PBIA_map** wrongly classifies the area as **1. Artificial Territories**, while COS identifies it correctly as **3. Other Vegetation**.

6.3.1.2 Agriculture

Assessing the **2. Agriculture** classification is a more complex task, since the visual aids, the ortophotos, don't provide enough information to discern whether **PBIA_map** or COS is correct. This is especially true in the case of confusion between this class and **3. Other Vegetation**, which accounts for a significant portion of the errors.

A lot of confusion with class **1. Artificial Territories** can also be observed, both in the form of comission and omission errors. The omission errors occur mostly due to **PBIA_map**'s ability to correctly classify small artificial structures and roads, and are not real errors. As for the identified comission errors, these are areas which COS identifies as **1. Artificial Territories**, but are actually natural areas with vegetation. However, it is difficult to evaluate whether **PBIA_map**'s classification of **2. Agriculture** is correct, or if another vegetation class would be more accurate. An example of an incorrect classification is represented in Figure 6.7, in which **PBIA_map** wrongly identifies a park as **2. Agriculture** instead of the expected **3. Other Vegetation**.

6.3.1.3 Other Vegetation

In **3. Other Vegetation**, most of the identified errors occur due to **PBIA_map**'s ability to more accurately delineate the classes, as seen in Figure 6.8.

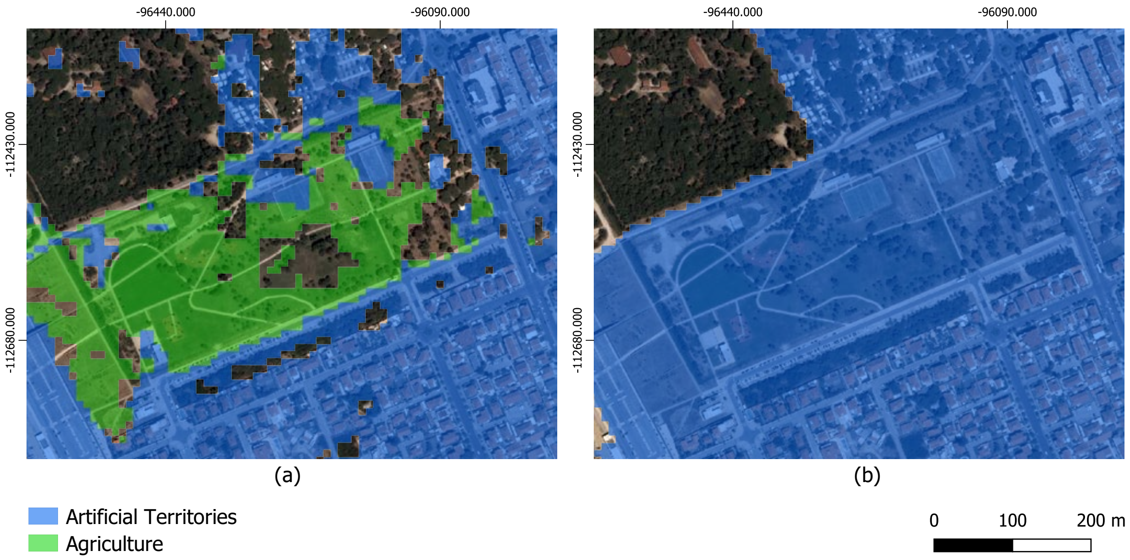

Figure 6.7: Classification examples of **PBIA_map** (a) and COS (b) with ortophoto background. **PBIA_map** wrongly classifies the area (a park) as **2. Agriculture**, instead of the expected **3. Other vegetation**. COS identifies this area as **1. Artificial Territories**.

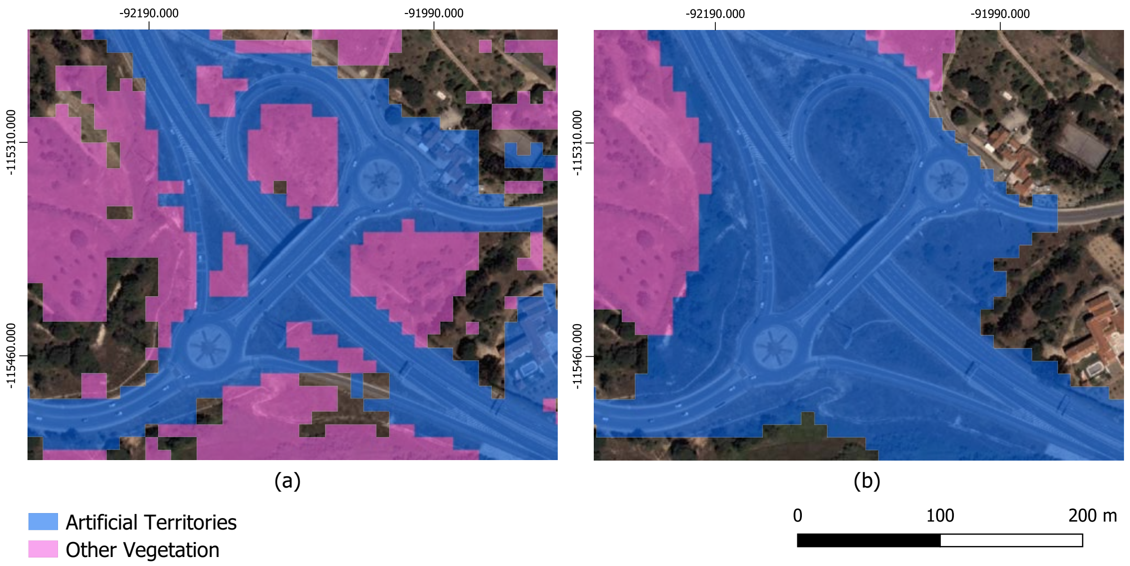

Figure 6.8: Classification examples of **PBIA_map** (a) and COS (b) with ortophoto background. **PBIA_map** is able to delineate both classes with better precision than COS.

PBIA_map can even identify some (although not all) small vegetation inside urban conglomerates, not identified in COS, as in Figure 6.9

Figure 6.9: Classification examples of **PBIA_map** (a) and COS (b) with ortophoto background. **PBIA_map** identifies small areas of vegetation, not represented in COS.

As mentioned in the previous subsection, a considerable amount of errors also occur due to confusion with class **2. Agriculture**.

6.3.1.4 Forests

The majority of omission errors in this class are areas that are classified in **PBIA_map** as **3. Other Vegetation**, generally due to not having a thick coverage of trees. In most cases, **PBIA_map**'s identification seems to have a better correspondence to the ortophotos, such as in Figure 6.10

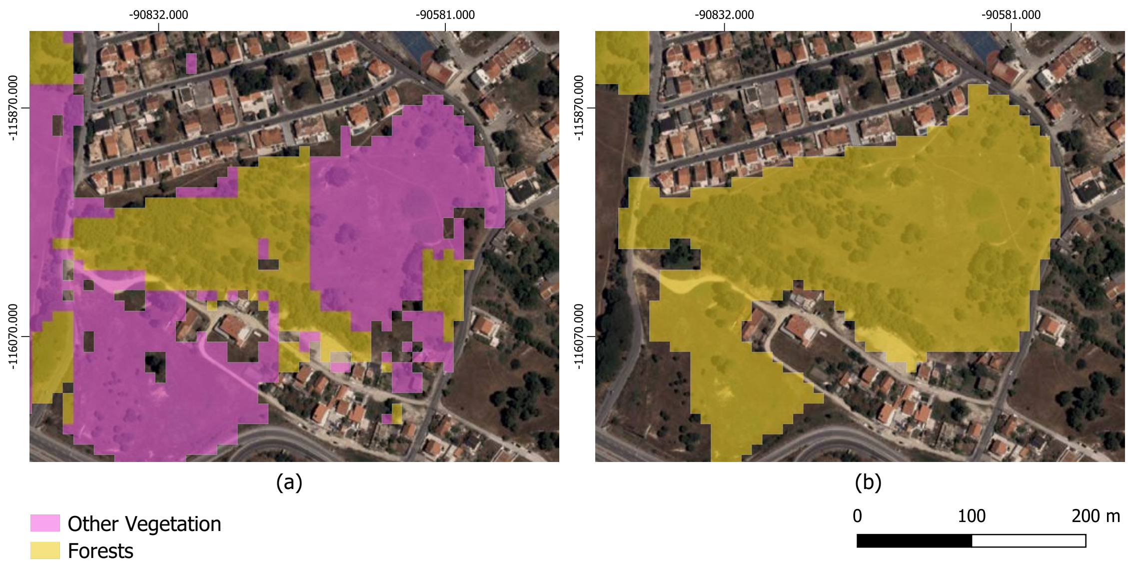

Figure 6.10: Classification examples of **PBIA_map** (a) and COS (b) with ortophoto background. **PBIA_map** is able to correctly separate **3. Other Vegetation** and **4. Forests**.

The comission errors in this class are mainly in parts of the problematic areas detailed in Chapter 5: Aroeira, Alfeite and parks, and seem to be correctly classified in **PBIA_map**. Figure 6.11 presents an area where **PBIA_map** is able to delineate the forests, as opposed to COS, which identifies the full areas as **1. Artificial Territories**.

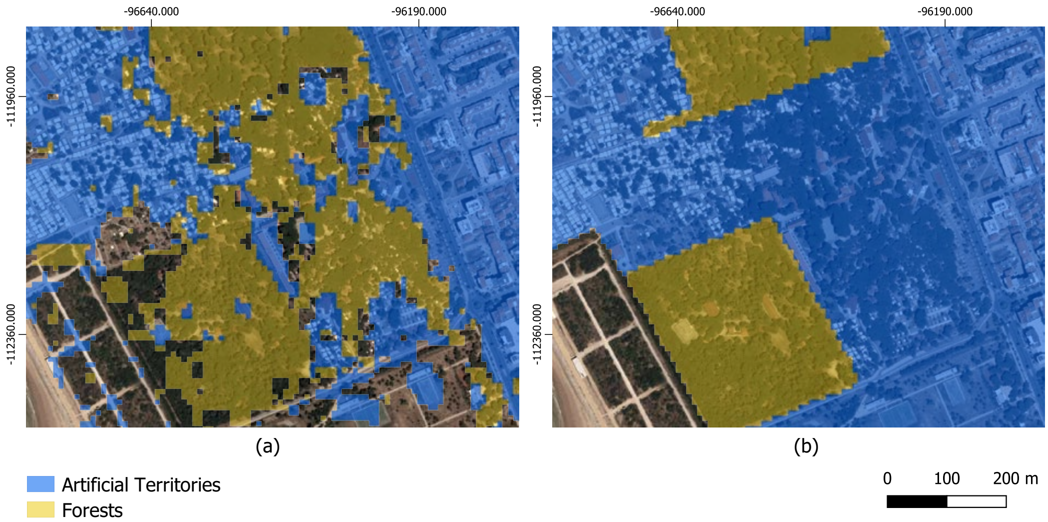

Figure 6.11: Classification examples of **PBIA_map** (a) and COS (b) with ortophoto background. **PBIA_map** is able to delineate **4. Forests** with high precision.

6.3.1.5 Bare and sparsely vegetated areas

A considerable portion of this class' identified errors are due to **PBIA_map**'s correct classification of beach bars and roads as **1. Artificial Territories**, as can be seen in Figure 6.12. The breakwaters are also identified as class 1, which could be considered correct, as they are man-made.

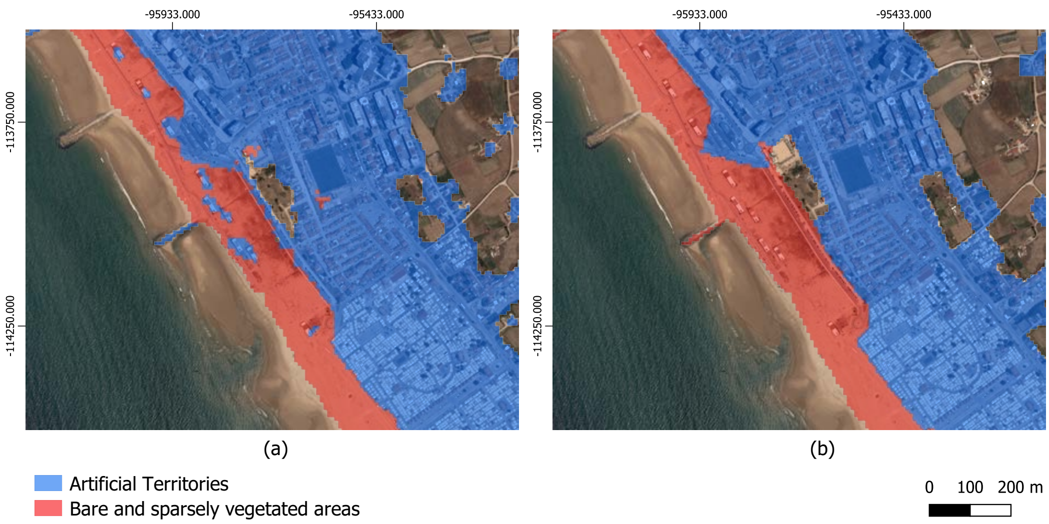

Figure 6.12: Classification examples of **PBIA_map** (a) and COS (b) with ortophoto background. **PBIA_map** correctly identifies the small beach bars and breakwaters.

Additionally, some errors occur in open areas, with no vegetation, like sports fields (covered in dirt), as in Figure 6.13, and the parking areas near the beach (covered in sand), and are not true errors of **PBIA_map**.

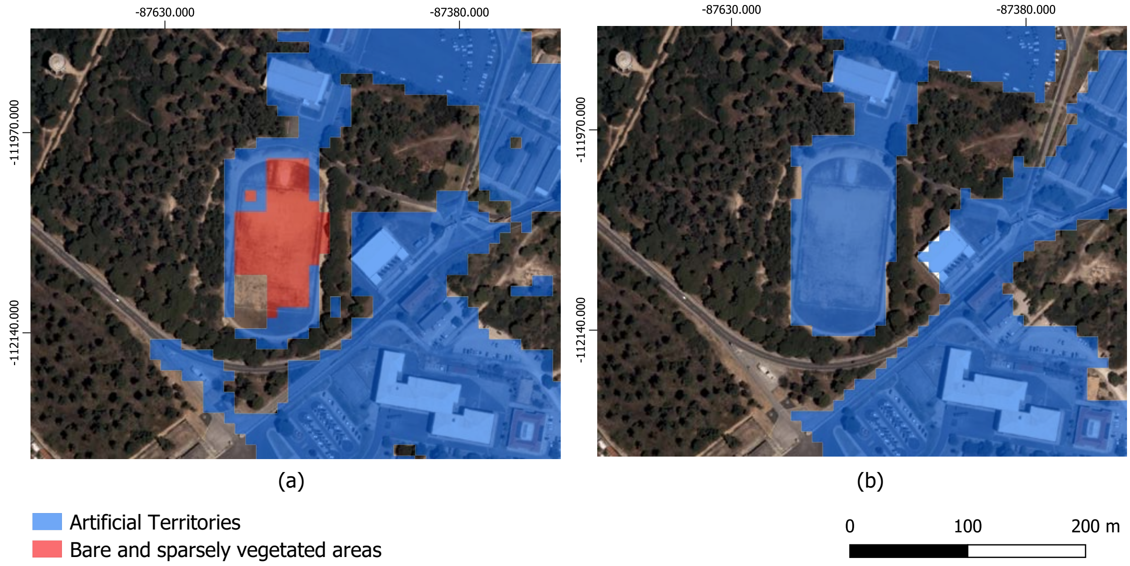

Figure 6.13: Classification examples of **PBIA_map** (a) and COS (b) with ortophoto background. **PBIA_map** correctly identifies a dirt sports field as **5. Bare and sparsely vegetated areas**.

6.3.2 COSsim

The kappa value of the comparison between COSsim and **PBIA_map** was **0.6085**, a moderate agreement, and Table 6.15 presents the percentage of comission and omission errors of each class. Once more, class **3. Other vegetation** had the worst performance, followed by **2. Agriculture**. Surprisingly, class **5. Bare and sparsely vegetated areas**, one of the highest performing classes in the test sets, had 50% of omission errors. Class **1. Artificial Territories** had the lowest amount of disagreement between the two maps.

	Comission Errors (%)	Omission Errors (%)
1. Artificial Territories	20,64	4,02
2. Agriculture	33,47	47,84
3. Other Vegetation	39,03	58,65
4. Forests	35,51	17,30
5. Bare and sparsely vegetated areas	9,62	50,69

Table 6.15: Comission and omission errors in **PBIA_map** using COSsim as reference.

Once more, a detailed visual analysis for each class was produced, with the support of the confusion matrix, presented in Table 6.16.

	True Class				
Predicted Class	1	2	3	4	5
1	36,05	2,94	3,85	0,71	1,87
2	0,55	7,98	2,93	0,28	0,25
3	0,49	3,56	9,94	2,21	0,11
4	0,40	0,76	7,22	15,34	0,06
5	0,07	0,06	0,10	0,00	2,23

Table 6.16: Area-based (% of total area) confusion matrix of **PBIA_map** using COSsim as reference.

6.3.2.1 Artificial Territories

The majority of errors in this class are due to mismatched edges with COSsim. This happens due to the difference in spatial resolution between both maps, but also because of the previously mentioned issue with shifted and/or overestimated boundaries. Interestingly, COSsim seems to have the opposite problem, and sometimes under-represents this class, as can be seen in Figure 6.14.

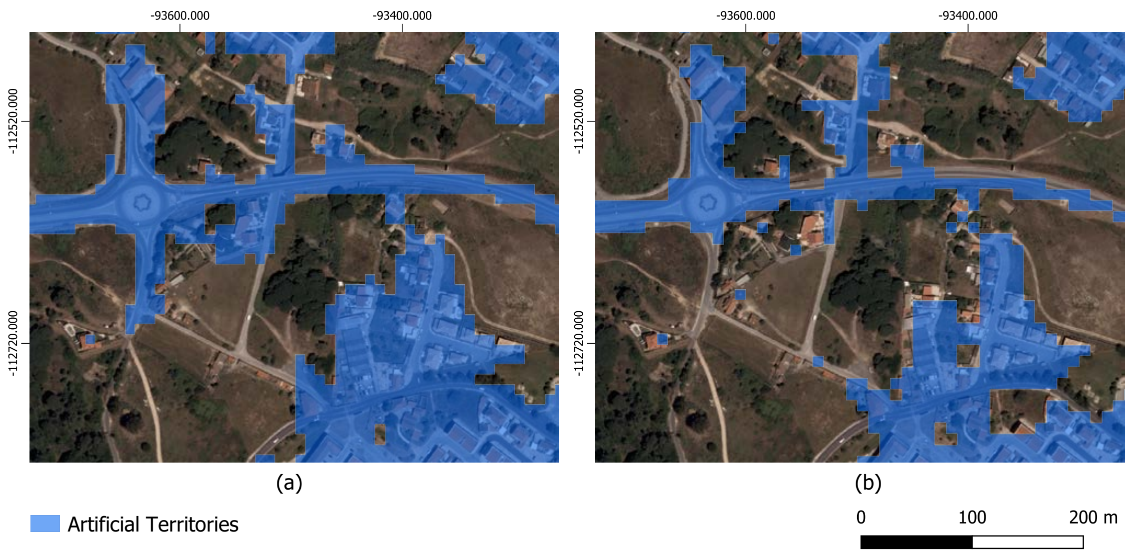

Figure 6.14: Classification examples of **PBIA_map** (a) and COSsim (b) with ortophoto background. **PBIA_map** appears to be overestimating the edges of **1. Artificial Territories**, while COSsim appears to underestimate them.

In addition, **PBIA_map** is capable of detecting smaller roads and houses with higher accuract, which COSsim does not identify, such as in Figure 6.15.

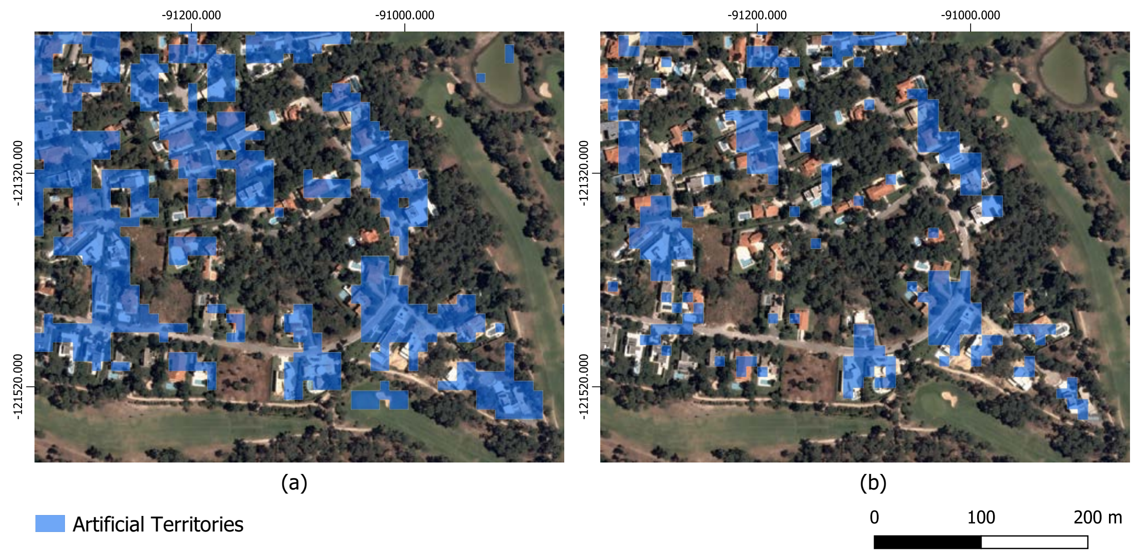

Figure 6.15: Classification examples of **PBIA_map** (a) and COSsim (b) with ortophoto background. **PBIA_map** is able to identify small roads and structures, which COSsim cannot.

6.3.2.2 Agriculture

In this class, a large amount of disagreement is due to confusion with **3. Other Vegetation**, which is, again, extremely hard to visually evaluate.

6.3.2.3 Other vegetation

A significant portion of this class' errors, arise from a specific area which is classified in **PBIA_map** as **Forests**. These are likely inaccuracies in COSsim, as COS's classification of the same area is **Forest**, more specifically **Invasive forest**.

Additionally, some errors are identified due to **PBIA_map**'s better separation between this class and **4. Forests**, and are not true errors, as can be seen in Figure 6.16

6.3.2.4 Forests

For the class **4. Forests**, most of identified errors are well classified in **PBIA_map** and are due to the disagreement on the classification of **Invasive forest**, and the better delineation of this class, as previously detailed.

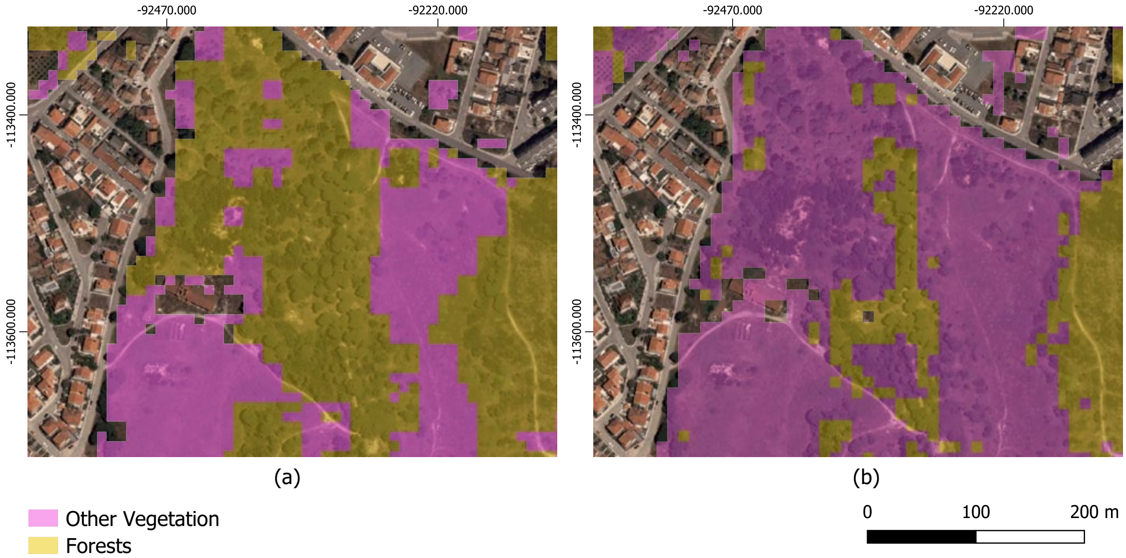

Figure 6.16: Classification examples of **PBIA_map** (a) and COSsim (b) with ortophoto background. **PBIA_map** is able to separate **3. Other Vegetation** and **4. Forests** more accurately than COSsim.

6.3.2.5 Bare and sparsely vegetated areas

The biggest source of comission errors in this class is confusion with class **3. Other Vegetation**, mostly due to slightly mismatched edges. In addition, an interesting source of comission errors in this class is the region represented in Figure 6.17. Here, COSsim wrongly classifies a big portion of the area as **2. Agriculture**, while **PBIA_map** is able to discern that it is in fact mostly **5. Bare and sparsely vegetated areas**.

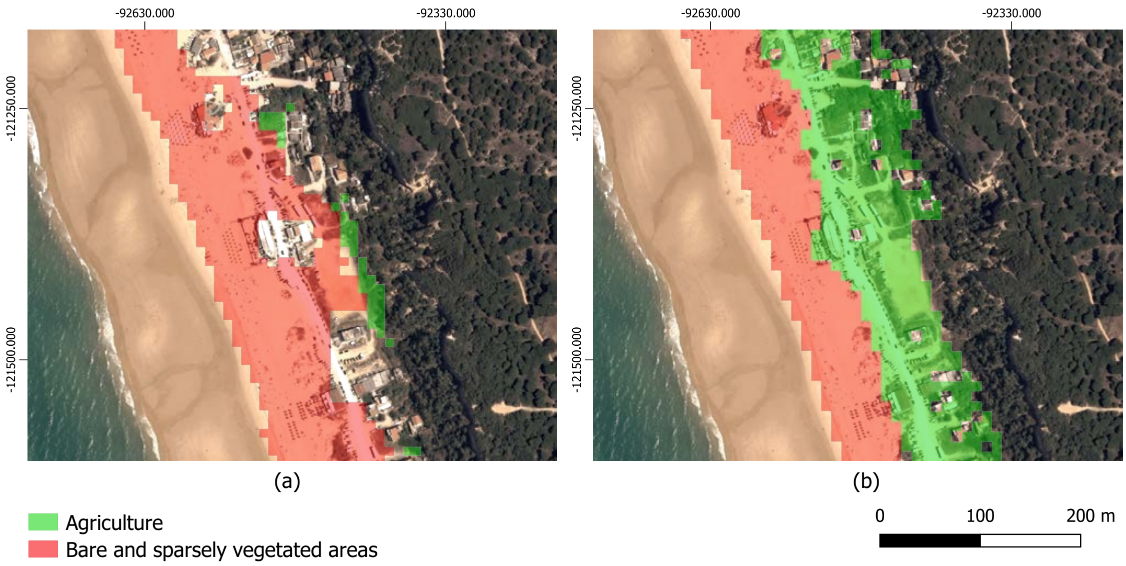

Figure 6.17: Classification examples of **PBIA_map** (a) and COSsim (b) with ortophoto background. **PBIA_map** correctly identifies the area as **5. Bare and sparsely vegetated areas**, while COSsim classifies it as **2. Agriculture**.

The percentage of omission errors in this class is the second highest out of all classes, surprising since it was consistently one of the best performing classes in the test sets of all classification models. In general, COSsim seems to have some difficulty distinguishing between classes **1. Artificial Territories** and **5. Bare and sparsely vegetated areas**, which causes the disagreement with **PBIA_map**. Observing the ortophotos, the majority of the supposed errors are, in fact, correctly classified in **PBIA_map**, such as in Figure 6.18 and 6.19.

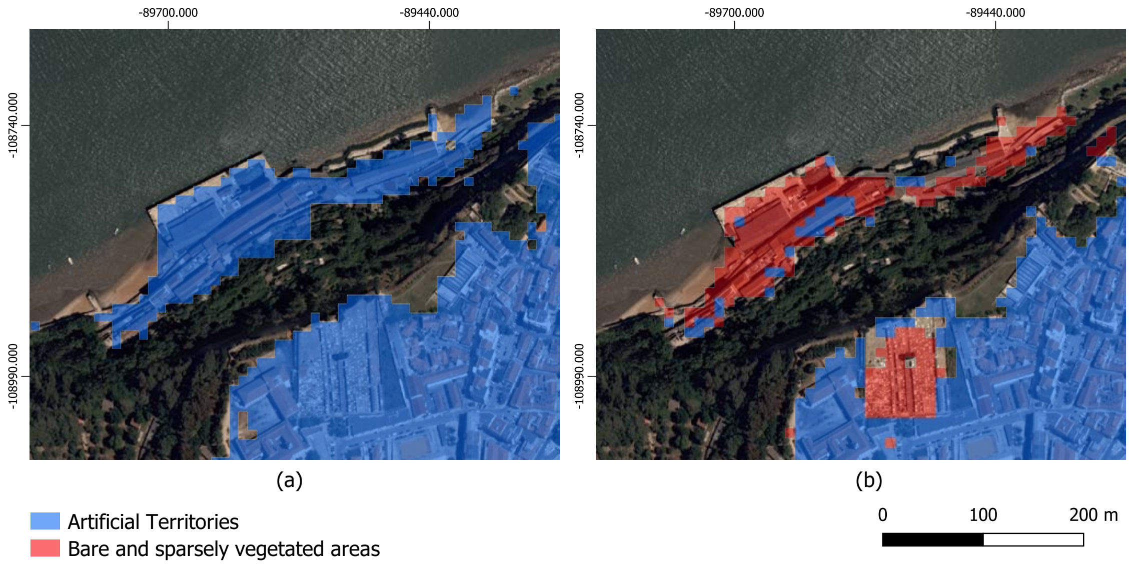

Figure 6.18: Classification examples of **PBIA_map** (a) and COSsim (b) with ortophoto background. **PBIA_map** correctly identifies the area as **1. Artificial Territories**, while COSsim presents some confusion with this class and **5. Bare and sparsely vegetated areas**.

6.3.3 Conclusions

PBIA_map has a higher level of agreement with COS than with COSsim, which is understandable, since COS was used as reference data to construct the ground truth (in conjunction with ortophotos).

Through the analysis of each class, it was possible to conclude that **1. Artificial Territories**, **4. Forests** and **5. Bare and sparsely vegetated areas** seem to be well classified in **PBIA_map**, with disagreements being mostly due to issues in the reference data. As for **2. Agriculture** and **3. Other vegetation**, it is hard to assess the quality of the classifications, though it is obvious that a lot of confusion exists between them. It is likely that **PBIA_map** possesses some amount of errors, since disagreements occurred with both COS and COSsim.

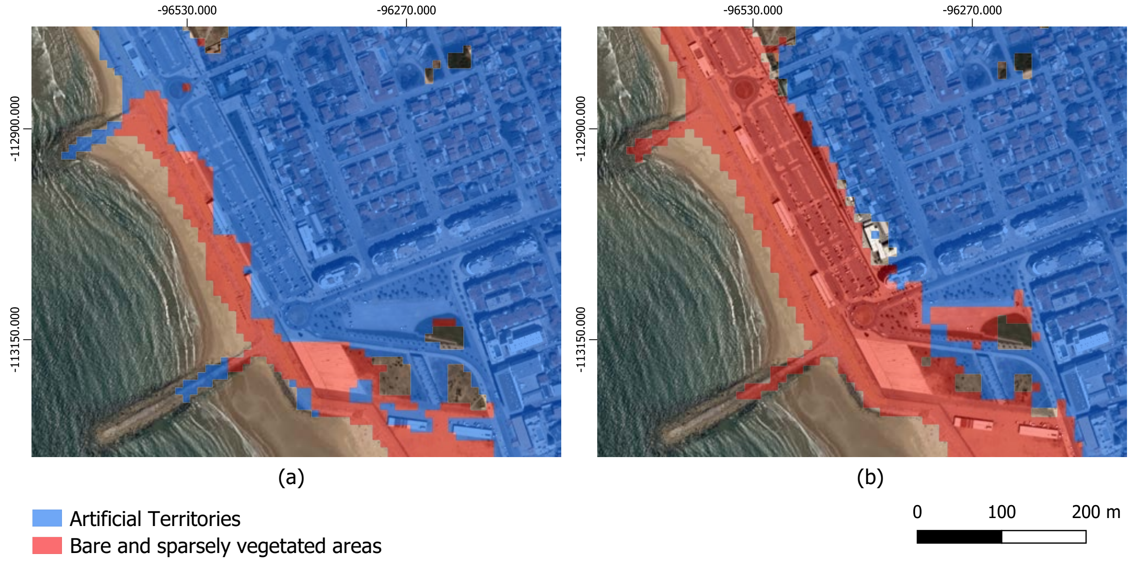

Figure 6.19: Classification examples of **PBIA_map** (a) and COSsim (b) with ortophoto background. **PBIA_map** correctly separates classes **1. Artificial Territories** and **5. Bare and sparsely vegetated areas**. COSsim incorrectly classifies the parking lot as **5. Bare and sparsely vegetated areas**.

6.4 Conclusion

The results obtained in this chapter allowed for multiple conclusions.

First, the experiments comparing the multiple combinations of input data and classifiers showed that XGB was the highest performing classifier in all tests, with the combination of input data **S1+S2+T1** producing the model with the best kappa.

For this group of classes in this region, spectral indices proved to be ineffective, deteriorating the performance of all models where present. The addition of textural features, had either a neutral or slightly positive effect in most models. In the best classification model, **S1+S2+T1** with XGB, **T1** helped to further distinguish between classes **1. Artificial Territories** and **5. Bare and sparsely vegetated areas**, and **3. Other vegetation** and **4. Forests**.

Moreover, the models which included the three calculated percentiles, 30th, 50th and 70th, all produced higher results than their counterparts using only the 50th percentile, with the three most spectrally similar classes (**2. Agriculture**,**3. Other vegetation** and **4. Forests**) particularly benefiting from this inclusion.

The experiments using a semi-automatic ground truth revealed that the use of a automatic approach based on the existing LULC map, COS, created a model that adapted to the errors in ground truth and delivered a less precise map, especially in class **Artificial Territories**. This is especially pertinent since a significant amount of studies are produced using existing LULC maps to collect ground truth, without considering (or mentioning) the amount of errors or inconsistencies they can have [22].

Finally, the map created with the best classification model, **PBIA_map** appears to have some issues identifying **2. Agriculture** and **3. Other Vegetation**, although an objective assessment of the performance is difficult. However, the map presents a high degree of accuracy in classes **1. Artificial Territories**, **4. Forests** and **5. Bare and sparsely vegetated land**. Comparing the classifications of these classes **PBIA_map** and COS, it is clear that **PBIA_map** can detail more information, which is not surprising due to COS's lower spatial resolution. However, comparisons with COSsim, which has a similar spatial resolution, further proved the accuracy and superiority of the **PBIA_map** in those three classes.

7

Results - Object Based Approach

This chapter contains all results related to the object-based approach. It is divided in two main sections: segmentation and classification. The first section consists of all the discussions concerning segmentation. The second is divided in two parts: presentation and analysis of all the classification results obtained with the different combinations of input data and classifiers; and comparison between the final obtained LULC map, and the available reference data.

All coordinates are presented in the EPSG:3763 Coordinate System.

7.1 Segmentation Results

Table 7.1 contains the details of the segmentations produced for the study region, including the ID, the MSS spatial and range radius used, and the number of segments it created.

Table 7.1: Segmentation experiments

ID	Spatial radius	Range radius	No. of Segments
A	5	2	16208
B	5	1.5	35966
C	5	1.25	50639
D	5	1	67756
E	5	0.75	86684
F	5	0.25	122746
G	7	2	15243
H	7	1.5	33659
I	7	1.25	48204
J	7	1	65519
K	7	0.75	84888
L	7	0.25	122342

The influence of the MSS parameters on the number and size of the segments was studied. In Figure 7.1 it is possible to observe that variations in range radius lead to significant changes in both number and size of the segments, although the same is not true for the spatial radius. The difference between segmentations with spatial radius 5 and 7 gets progressively smaller, as the image becomes oversegmented, and all segments approach the set minimum of 4 pixels.

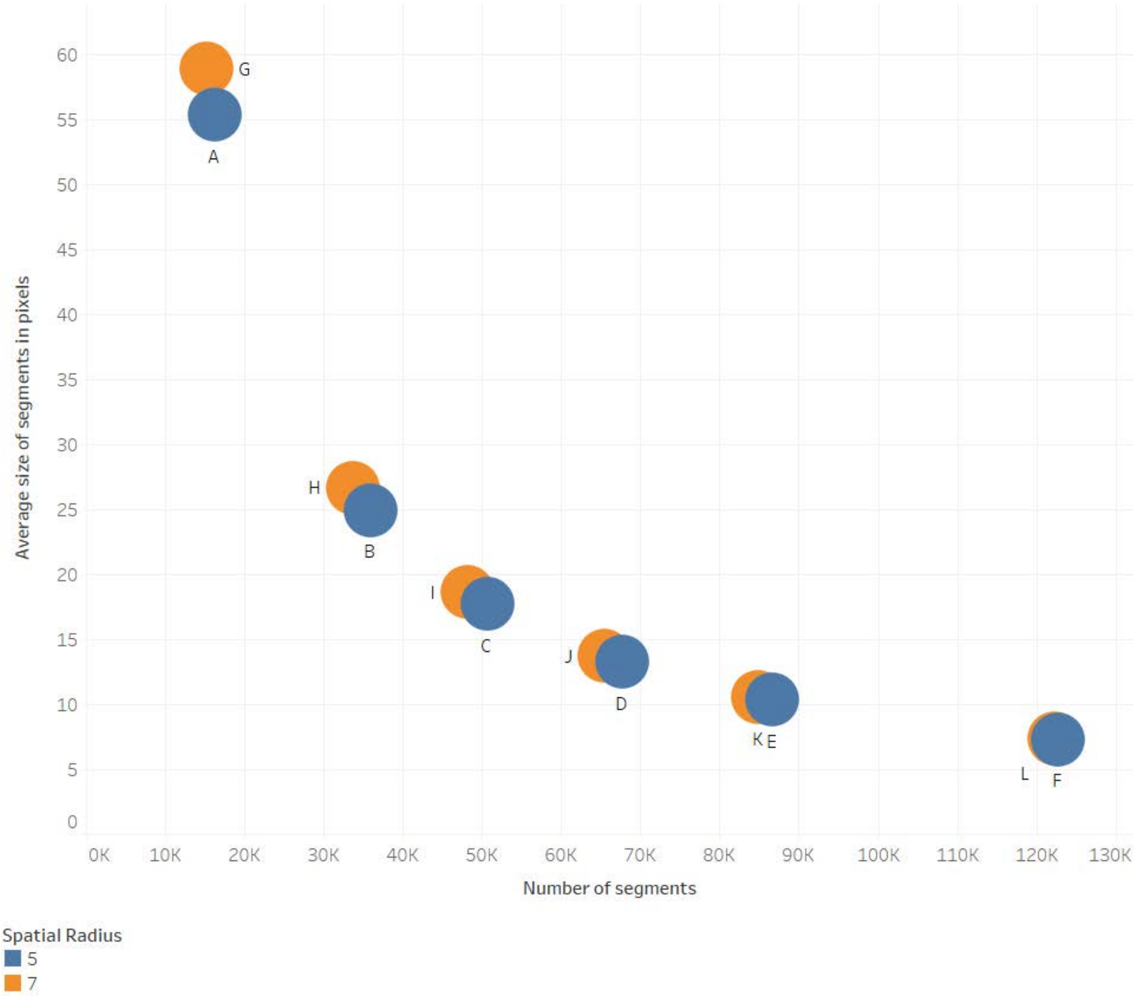

Figure 7.1: Number and average size of objects in each segmentation

Figure 7.2 and Figure 7.3 represent, respectively, the computed WV and MI for each principal component, of each segmentation. The behaviors of the indices are similar in all principal components. As seen in the reviewed literature [25, 9], when the image is undersegmented, such as in segmentation **A**, the WV is high. As the segmentations start to get more fine and oversegmentation starts, WV continuously decreases. As for the MI, it is low when the image is undersegmented and it rises as the number of segments also increases, indicating that the new segments produced are increasingly similar to their neighbors and demonstrating that the image is approaching oversegmentation.

Almost every segmentation produced with the spatial range of 7 obtained lower MI and WV values than its 5 counterpart, even with less segments produced. Since the objective is to minimize both indices, the results seem to point to the superiority of the segmentations produced using spatial radius 7. As for the ideal range radius, the indices

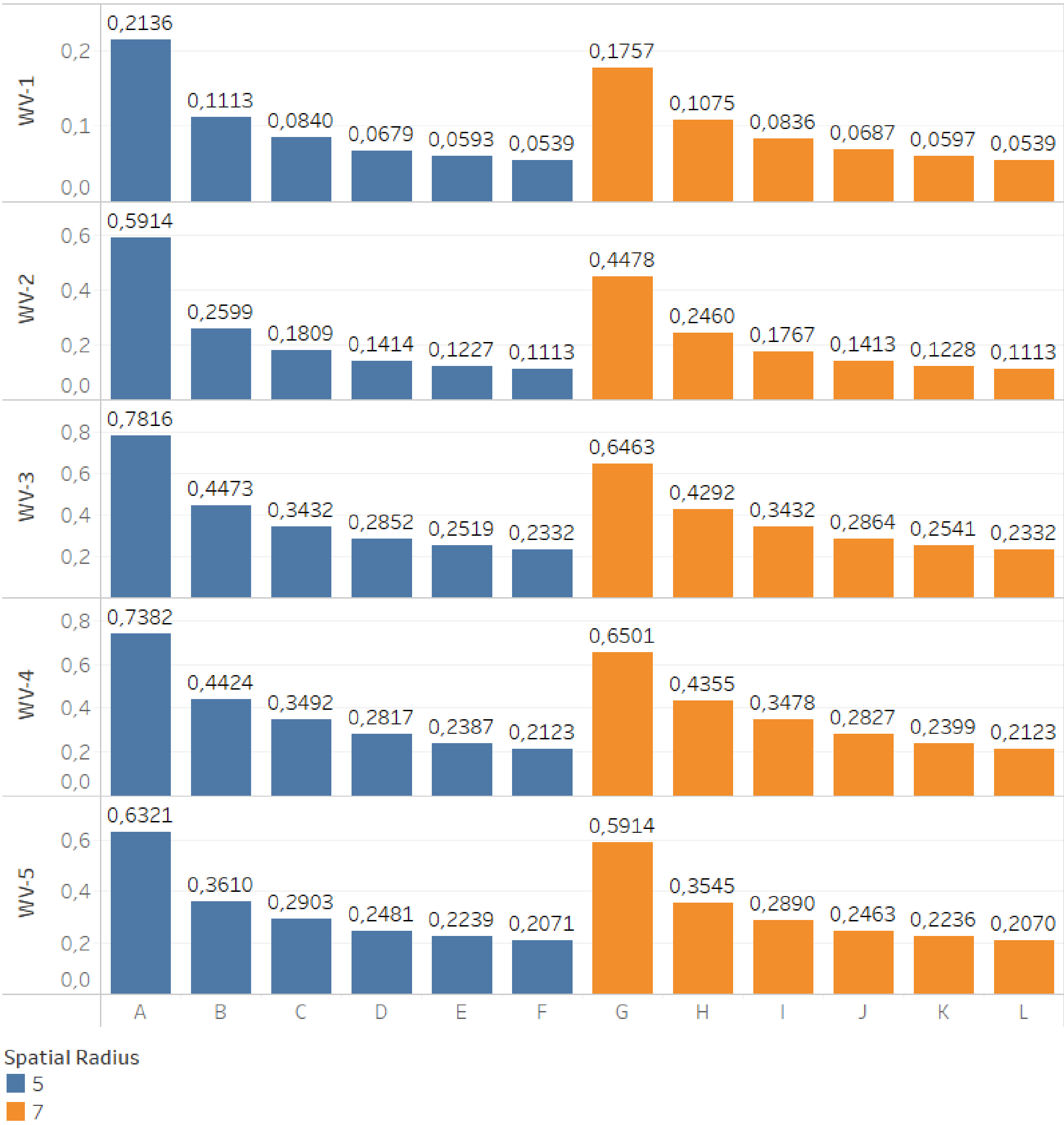

Figure 7.2: Weighted Variance for each principal component, per segmentation

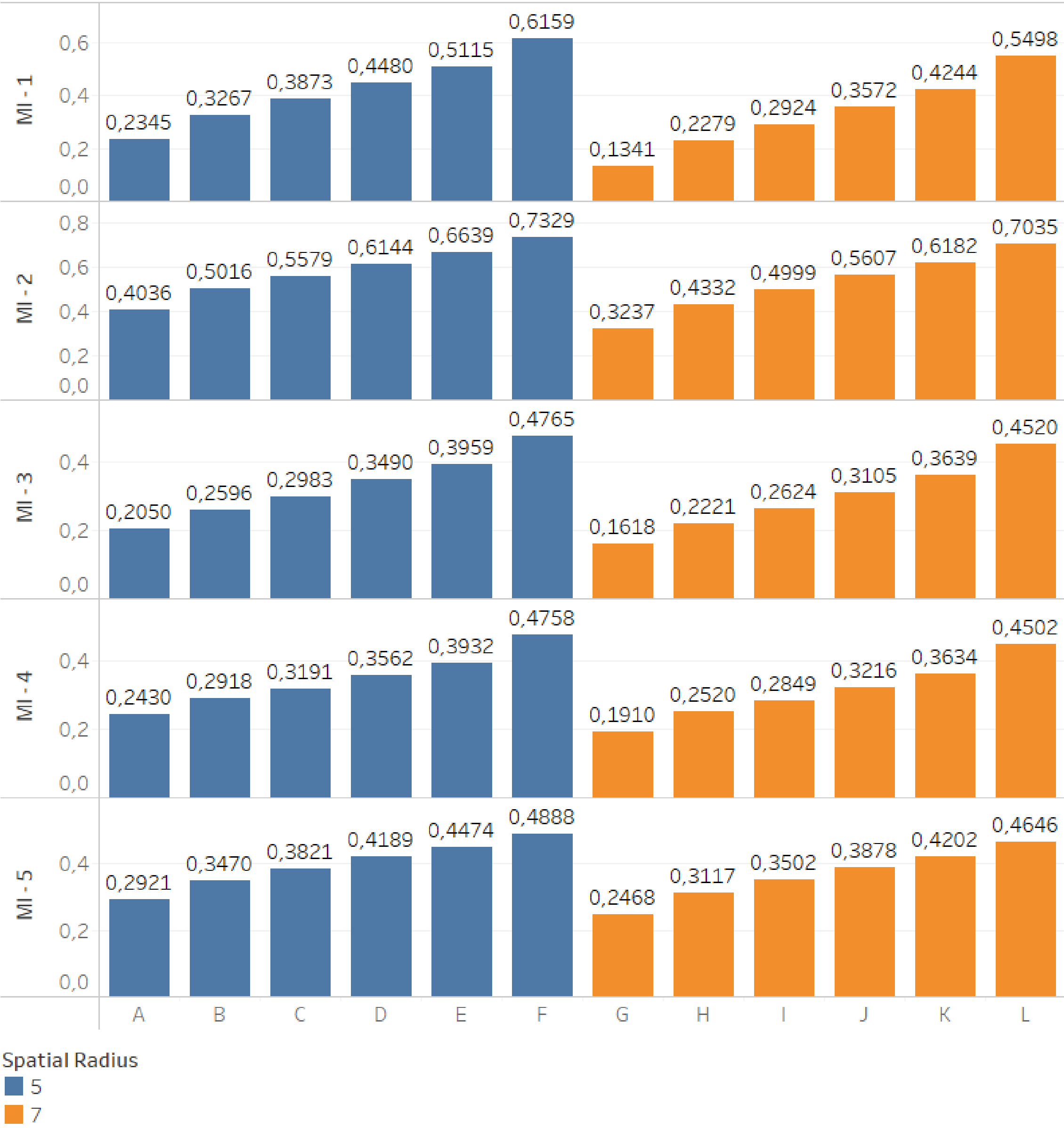

Figure 7.3: Moran's Index for each principal component, per segmentation

had to be complemented with visual analysis. Considering all segmentations produced, as well as the fact that, in land-cover classification, some oversegmentation is more desirable than undersegmentation, the chosen segmentation was **J**.

Segmentation **J** presents an overall good delineation of objects. Urban areas are much more finely separated, almost reaching oversegmentation, while different types of natural areas have a less precise separation, which will undoubtedly affect the quality of the classification. Figure 7.4 presents two examples of areas in this segmentation.

Figure 7.4: Example areas of segmentation **J**. Urban areas are finely segmented, whereas natural areas have less precise separation and non-homogeneous segments.

7.2 Classification

7.2.1 Experiments

The first models were produced using the different combinations of input data with all calculated percentiles. The kappa values for the two classifiers are presented in Table 7.2.

	XGB	RF
S1+S2+SA	0,88736	0,87797
S1+S2+SA+SI	0,88427	0,87660
S1+S2+SA+T1	0,89339	0,88251
S1+S2+SA+T2	0,89490	0,87607

Table 7.2: Kappa values for each dataset, per classifier - all percentiles

XGB was the highest performing classifier in all experiments. However, the RF models also delivered comparable results, aside from **S1+S2+SA+T2** which had an unusual low result.

The inclusion of spectral indices had a small negative effect on both classifiers, but in contrast, the presence of textural features improved the kappa of all experiences, except in the model using **S1+S2+SA+T2** and RF. Interestingly, the dataset **S1+S2+SA+T2** produced the best performing model, using XGB, and the worst performing of the group, using RF.

The F1 score, precision and recall of each class, for each experiment, are presented in Table 7.3 and Table 7.4. In both classifiers, class **1. Artificial Territories** and **5. Bare and sparsely vegetated areas** had consistently the best results in all experiments. In contrast, class **3. Other Vegetation** had the worst results, followed by **4. Forests** and **2. Agriculture**. The use of XGB was highly beneficial for classes **4. Forests** and **3. Other Vegetation**.

Analysing the XGB results, the inclusion of spectral indices had a beneficial effect in class **5. Bare and sparsely vegetated areas** and **1. Artificial Territories**. The remaining classes, 2**. Agriculture**, 3**. Other Vegetation** and **4. Forests** all had a decrease in F1 values. This is due to the calculated spectral indices being specifically for identifying built up areas and vegetation, and as such, likely not useful in distinguishing between different types of vegetation. The addition of **T1** produced a positive effect in the F1 score of all classes, but **T2** generated a slightly higher increase, helping to separate classes **4. Forests** and **3. Other Vegetation**, as can be observed by comparing the **S1+S2+SA** confusion matrix, presented in Table 7.5, to the one obtained by **S1+S2+SA**, in Table 7.6.

		XGB		
Dataset	Class	F1 Score	Precision	Recall
S1+S2+SA	1	0,98981	0,98981	0,98981
	2	0,86384	0,89063	0,83824
	3	0,79221	0,77707	0,80795
	4	0,86222	0,85840	0,86607
	5	0,98824	0,97674	1,00000
S1+S2+SA+SI	1	0,99490	0,99490	0,99490
	2	0,86142	0,87786	0,84559
	3	0,76923	0,77702	0,76159
	4	0,84483	0,81667	0,87500
	5	1,00000	1,00000	1,00000
S1+S2+SA+T1	1	0,98730	0,98480	0,98981
	2	0,86545	0,85612	0,87500
	3	0,79085	0,78065	0,80132
	4	0,86607	0,86607	0,86607
	5	1,00000	1,00000	1,00000
S1+S2+SA+T2	1	0,98985	0,98651	0,99321
	2	0,87023	0,90476	0,83824
	3	0,80656	0,79870	0,81457
	4	0,87225	0,86087	0,88393
	5	1,00000	1,00000	1,00000

Table 7.3: XGB Metric results for each dataset - all percentiles

		RF		
Dataset	Class	F1 Score	Precision	Recall
S1+S2+SA	1	0,98981	0,98981	0,98981
	2	0,85057	0,88800	0,81618
	3	0,77814	0,75625	0,80132
	4	0,84444	0,84071	0,84821
	5	0,98824	0,97674	1,00000
S1+S2+SA+SI	1	0,99147	0,99319	0,98981
	2	0,86891	0,88550	0,85294
	3	0,76721	0,75974	0,77483
	4	0,81938	0,80870	0,83036
	5	0,98824	0,97674	1,00000
S1+S2+SA+T1	1	0,98983	0,98816	0,99151
	2	0,86792	0,89147	0,84559
	3	0,78431	0,77419	0,79470
	4	0,83929	0,83929	0,83929
	5	0,98824	0,97674	1,00000
S1+S2+SA+T2	1	0,98985	0,98651	0,99321
	2	0,87313	0,88636	0,86029
	3	0,76159	0,76159	0,76159
	4	0,82143	0,82143	0,82143
	5	1,00000	1,00000	1,00000

Table 7.4: RF Metric results for each dataset - all percentiles

	True Class				
Predicted Class	1	2	3	4	5
1	585	1	3	4	0
2	2	114	10	0	0
3	2	20	123	9	0
4	0	1	15	99	0
5	0	0	0	0	42

Table 7.5: XGB Confusion matrix for **S1+S2+SA+T2** - all percentiles

	True Class				
Predicted Class	1	2	3	4	5
1	583	2	2	2	0
2	2	114	11	1	0
3	3	20	122	12	0
4	0	0	16	97	0
5	1	0	0	0	42

Table 7.6: XGB Confusion matrix for **S1+S2+SA** - all percentiles

Analogous to Chapter 6, the same exact experiments were performed using only the 50th percentile of each band. Table 7.7 contains the kappa values of each experiment.

	XGB	RF
S1+S2+SA	0,87648	0,86368
S1+S2+SA+SI	0,86893	0,86543
S1+S2+SA+T1	0,87304	0,87453
S1+S2+SA+T2	0,89023	0,86983

Table 7.7: Kappa values for each dataset per classifier - 50th percentile

As expected, all experiments produced worse results than the equivalents in Table 7.2, with XGB classifier having the highest results. Once again, the combination **S1+S1+SA+T2** and XGB produced the model with the highest kappa, with a similar kappa to the one obtained by the identical model using all percentiles.

Analysing Table 7.8, it is possible to see that classes **1. Artificial Territories** and **5. Bare and sparsely vegetated areas**, **2. Agriculture** either don't benefit or benefit very slightly from the inclusion of the percentiles. On the other hand, class **3. Other Vegetation** had a significant increase in F1 score, on all experiments, as well as **4. Forests**.

		XGB		
Dataset	Class	F1 Score	Precision	Recall
S1+S2+SA	1	0,98981	0,98981	0,98981
	2	0,86131	0,85507	0,86765
	3	0,75768	0,78169	0,73510
	4	0,84348	0,82203	0,86607
	5	0,98824	0,97674	1,00000
S1+S2+SA+SI	1	0,99064	0,99317	0,98812
	2	0,85199	0,83688	0,86765
	3	0,73720	0,76056	0,71523
	4	0,83478	0,81356	0,85714
	5	0,98824	0,97674	1,00000
S1+S2+SA+T1	1	0,98730	0,98480	0,98981
	2	0,86545	0,85612	0,87500
	3	0,75254	0,77083	0,73510
	4	0,83556	0,83186	0,83929
	5	1,00000	1,00000	1,00000
S1+S2+SA+T2	1	0,99154	0,98820	0,99491
	2	0,87273	0,86331	0,88235
	3	0,78082	0,80851	0,75497
	4	0,86726	0,85965	0,87500
	5	0,98824	0,97674	1,00000

Table 7.8: XGB Metric results for each dataset - 50th percentile

To study the effect of the inclusion of the spatial geometric attributes in the classification, the best model so far, using **S1+S2+T2** with XGB was retrained, omitting the spatial attributes.

The kappa value obtained was **0.89959**, the highest result obtained in all experiments. Comparing the model's metrics, included in Table 7.9, with Table 7.3, an increase in both precision and recall can be seen in class **1. Artificial Territories**, **2. Agriculture** and **3. Other Vegetation**, while **4. Forests** suffered a small decreased in recall.

This result suggests that the inclusion of spatial geometric attributes is ineffective for this group of classes, perhaps due to them being mostly land-cover classes, which are usually separable by their spectral properties [28].

		XGB		
Dataset	Class	F1 Score	Precision	Recall
S1+S2+SA+T2	1	0,99323	0,98988	0,99660
	2	0,87879	0,90625	0,85294
	3	0,81046	0,80000	0,82119
	4	0,86607	0,86607	0,86607
	5	1,00000	1,00000	1,00000

Table 7.9: XGB Metric results for S1+S2+T2

To summarize, XGB was consistently the best performing classifier. The use of this classifier was particularly beneficial for classes **4. Forests** and **3. Other Vegetation**.

The inclusion of the spectral indices had a negative impact in most of the models, although they were sometimes useful in helping to distinguish **1. Artificial Territories** and **5. Bare and sparsely vegetated areas**. The inclusion of the 30th and 70th percentiles in the models had the highest positive impact in class **3. Other Vegetation**, followed by **4. Forests**.

Finally, the use of spatial geometric proved to be ineffective, as the highest kappa was obtained by excluding them from the model.

7.3 Comparison with available LULC maps

In this section, the full map produced by the best model: manual ground truth, S1+S2+T2 input data and XGB classifier; designated **OBIA_map** was compared against COS and COSsim. First, a quantitative analysis is produced followed by the results of the visual analysis in QGIS.

7.3.1 Carta de Uso e Ocupação do Solo (COS)

The kappa value of the comparison between COS and **OBIA_map** was **0.5734**, considered a moderate agreement, and Table 7.10 presents the percentage of comission and omission errors for each class. Class **3. Other Vegetation** had the worst performance, with a percentage of comission errors of over 73%. The class with the highest amount of agreement was **1. Artificial Territories**.

To understand the errors identified in **PBIA_map**, a detailed visual analysis for each class was constructed, with the support of the confusion matrix, presented in Table 7.11.

	Comission Errors (%)	Omission Errors (%)
1. Artificial Territories	7,41	26,99
2. Agriculture	34,06	49,39
3. Other Vegetation	73,05	24,12
4. Forests	26,43	27,21
5. Bare and sparsely vegetated areas	20,04	15,08

Table 7.10: Percentage of **OBIA_map**'s comission and omission errors using COS

	True Class				
Predicted Class	1	2	3	4	5
1	39,64	0,93	0,69	1,33	0,22
2	2,02	5,93	0,42	0,61	0,02
3	7,23	4,53	5,98	4,41	0,04
4	5,05	0,31	0,75	17,23	0,09
5	0,36	0,02	0,05	0,09	2,06

Table 7.11: Area-based (in proportion) confusion matrix of **OBIA_map** using COS as reference.

7.3.1.1 Artificial Territories

In general, the identified errors in class **1. Artificial Territories** are not true errors, and occur from ground truth inaccuracies. The problematic areas mentioned previously, Aroeira, Alfeite and parks, contribute significantly to these errors, but are generally correctly classified in **OBIA_map**.

OBIA_map is able to identify some small urban conglomerates and roads, not present in COS, two examples of which are represented in Figure 7.5 and 7.6. In Figure 7.5, even though **OBIA_map** represents the small roads, there are still some small artificial structureS that were not identified

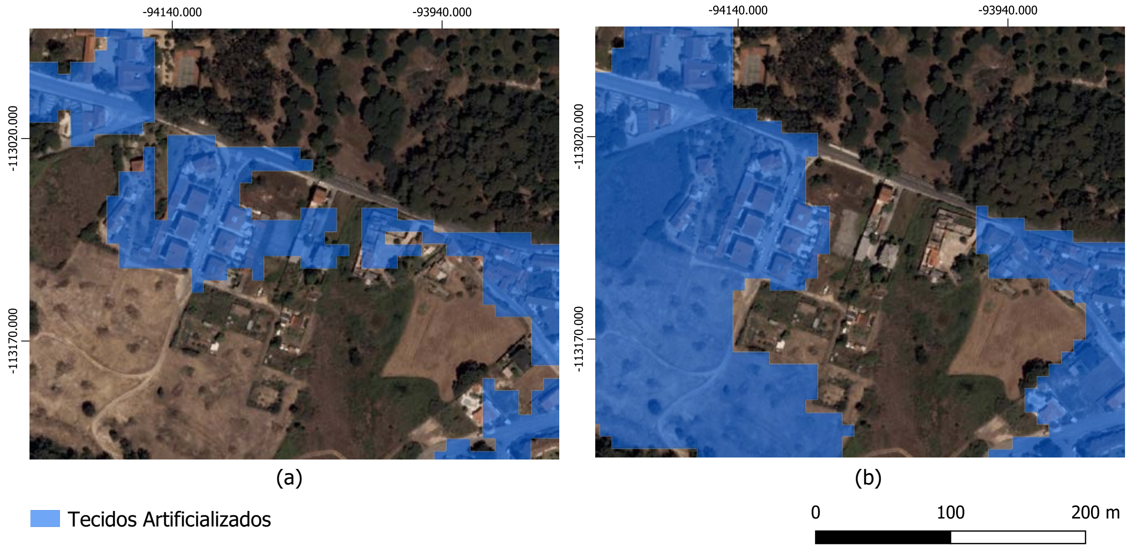

Figure 7.5: Classification examples of **OBIA_map**(a) and COS with ortophoto background. **OBIA_map** is able to delineate and detect artificial structures and roads, with higher precision than COS.

Figure 7.6: Classification examples of **OBIA_map**(a) and COS with ortophoto background. **OBIA_map** is able to identify small artificial structures, which are not identified in COS.

Nonetheless, some errors do exist in **OBIA_map**, as can be seen in Figure 7.7, which represents a portion of the Aroeira area. Although **OBIA_map** is able to discern some houses from the vegetation, it cannot distinguish all of them. Analysing the segmentation result in this area in Figure 7.8, it appears to be adequate, being able to detect the differences between houses and forest. However, most of the house segments include some amount of vegetation, which likely explains the incorrect classification.

Figure 7.7: Classification examples of **OBIA_map**(a) and COS with ortophoto background. Although **OBIA_map** is able to identify houses and artificial structures with higher precision than COS, a significant portion are not identified.

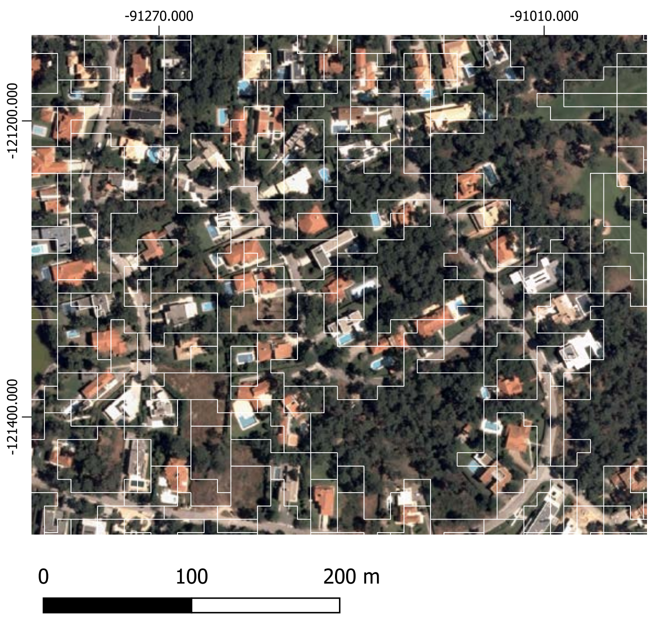

Figure 7.8: Segmentation result of the area represented in Figure 7.7. Most of the segments are not homogeneous, with a mixture of artificial structures and vegetation.

In addition, in the beach area, some rocky areas and the breakwaters are classified as class **1. Artificial Territories** in **OBIA_map** but considered class **5. Bare and sparsely vegetated areas** in COS. Although the breakwaters could be considered artificial structures and so, not an error in **OBIA_map**, the rocky parts are misclassifications.

Furthermore, the classifier seems to have difficulty distinguishing between **1. Artificial Territories** and sandy areas with medium coverage of vegetation, as can be seen in Figure 7.9. While COS fully classifies this area as **4. Forests**, visually it would appear to be either **3. Other Vegetation** or **5. Bare and sparsely vegetated areas**.

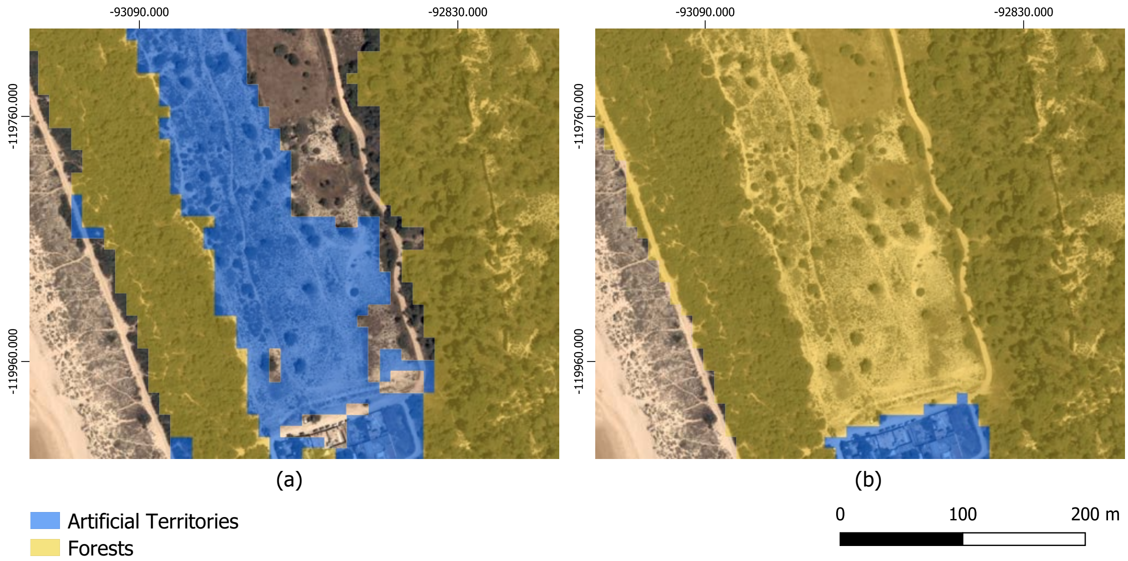

Figure 7.9: Classification examples of **OBIA_map**(a) and COS with ortophoto background. **OBIA_map** wrongly classifies the area as **1. Artificial Territories**, while COS classifies it as **4. Forests**.

7.3.1.2 Agriculture

In this class, the majority of errors occur due to confusion with class **3. Other Vegetation**, making it difficult to visually discern which map is correct.

Notwithstanding, there are also some areas in which **OBIA_map** wrongly classifies houses as **2. Agriculture**, as in Figure 7.10, probably due to the segmentation minimum area and small size of the structures.

7.3.1.3 Other Vegetation

A significant part of this class' errors occur due to confusion with class **4. Forests**. Although some instances exist where **OBIA_map** is accurate, the majority of the disagreement is due to true errors in classification in **OBIA_map**, which is not able to properly separate the classes. Figure 7.11 and 7.13 show two examples. The misclassifications seem to be a direct consequence of the segmentation, which was not able to separate the area in different segments, as shown in Figure 7.12 and 7.14.

Figure 7.10: Classification examples of **OBIA_map**(a) and COS with ortophoto background. **OBIA_map** wrongly classifies houses as **2. Agriculture**.

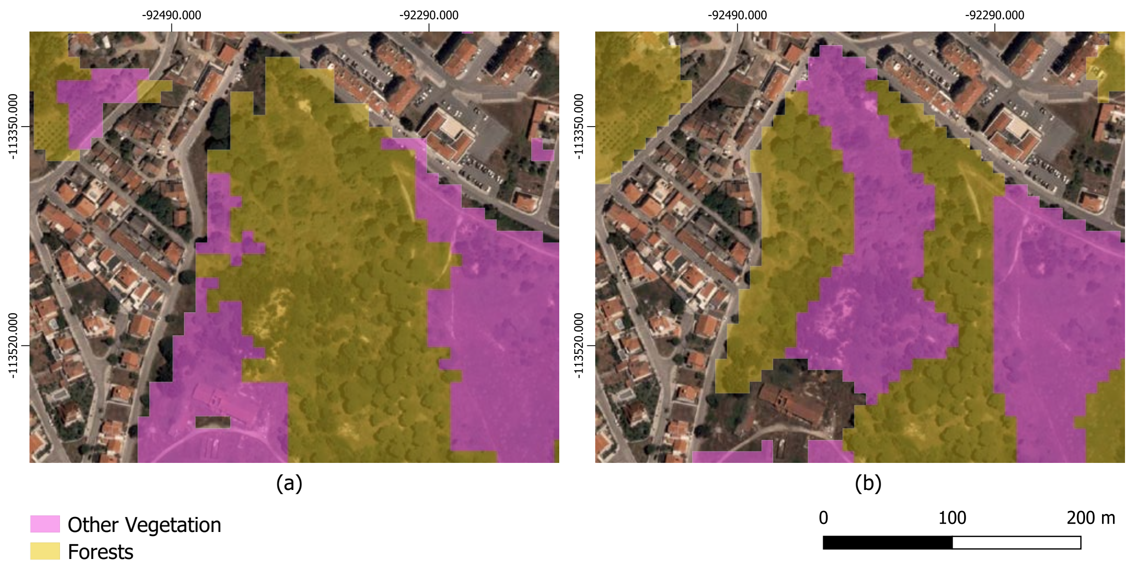

Figure 7.11: Classification examples of **OBIA_map**(a) and COS with ortophoto background. **COS** provides a more accurate separation of classes **3. Other Vegetation** and **4. Forests** than **OBIA_map**.

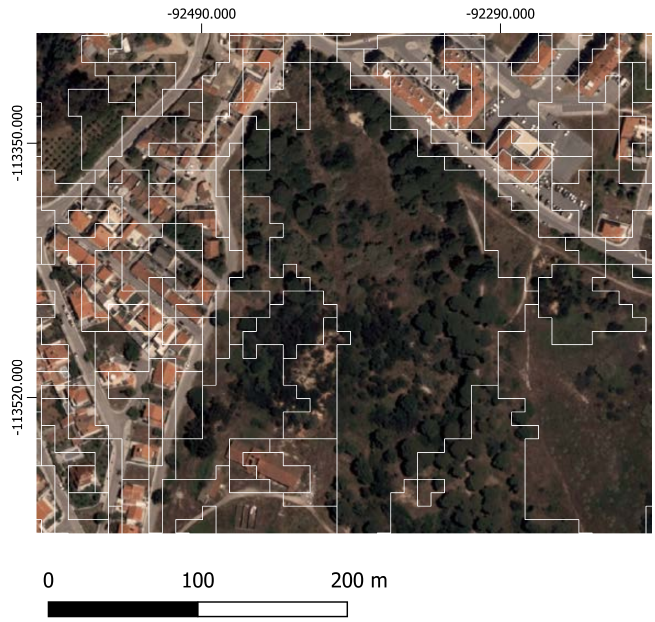

Figure 7.12: Segmentation result of the area represented in Figure 7.11. The main center segment is not homogeneous, and could have been subdivided.

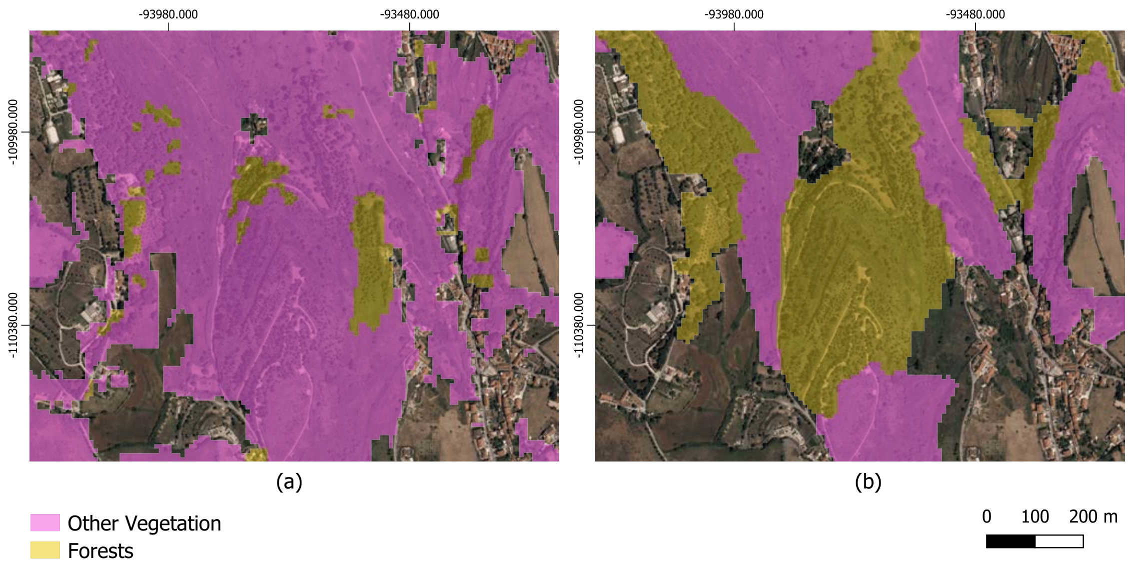

Figure 7.13: Classification examples of **OBIA_map**(a) and COS with ortophoto background. **COS** provides a more accurate separation of classes **3. Other Vegetation** and **4. Forests** than **OBIA_map**.

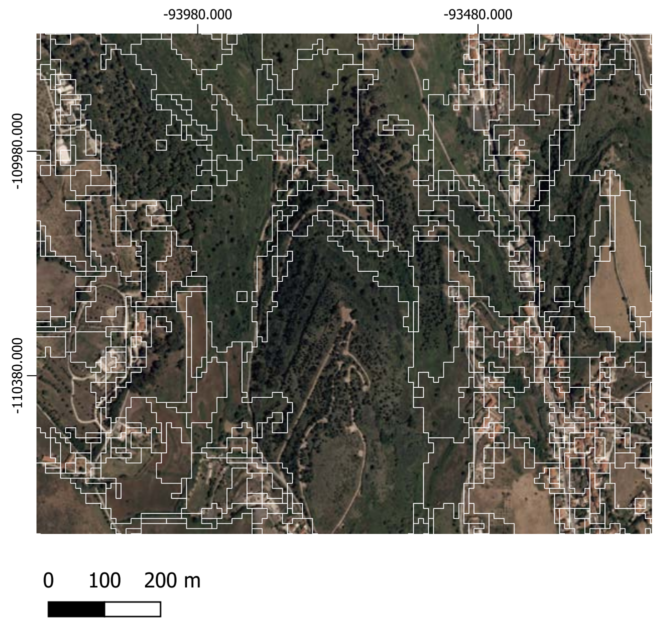

Figure 7.14: Segmentation result of the area represented in Figure 7.13. Some segments are not homogeneous, and could have been subdivided.

3. Other Vegetation has the highest percentage of comission errors, and a significant portion arise from parks, golf courses, and the Aroeira area, and are correctly classified in **OBIA_map**. In addition, some of the small green areas in mostly urban zones are not classified as vegetation in COS but are correctly identified in **OBIA_map**.

7.3.1.4 Forests

In this class, the majority of omission errors are due to confusion with class **3. Other Vegetation**, and seem to be real inaccuracies in **OBIA_map** as declared before.

However, most of the comission errors are not actual errors, and stem from better delineation of classes in the Aroeira and Alfeite areas, with the latter being represented in Figure 7.15.

7.3.1.5 Bare and sparsely vegetated areas

The majority of errors in this class arise from the already discussed situations of breakwaters, rocky portions of beach and beach bars.

An interesting case in this class are two sports fields, one with synthetic grass and one which appears covered in dirt and sand, which **OBIA_map** identifies as class **5. Bare and sparsely vegetated areas**, but are marked in COS as **1. Artificial Territories**. **OBIA_map**'s classification of the dirt field, though not compatible with COS, was logical, while the synthetic grass was unexpected.

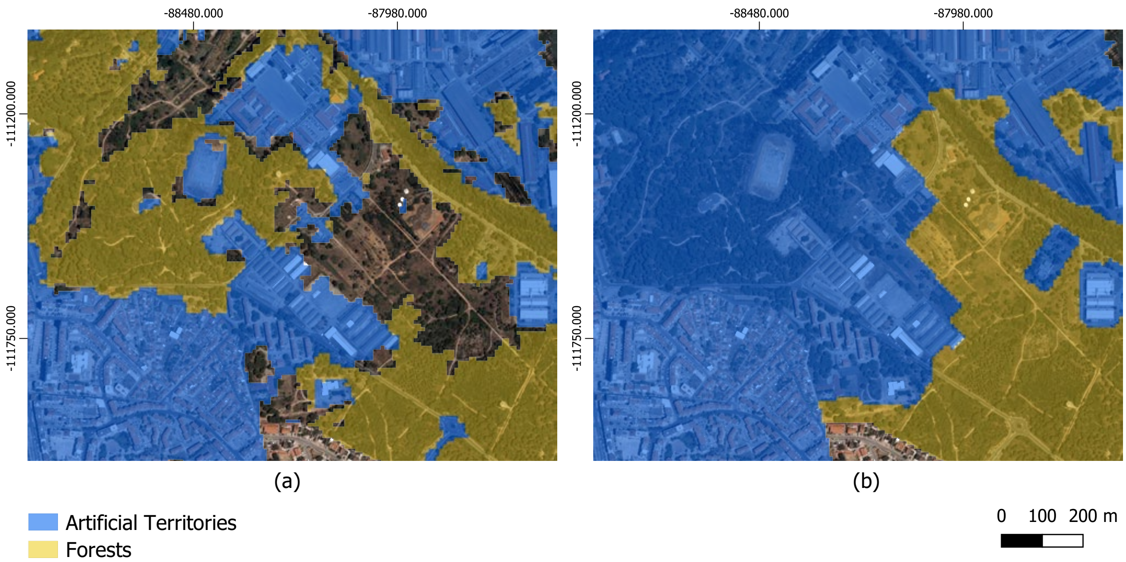

Figure 7.15: Classification examples of **OBIA_map**(a) and COS with ortophoto background. **OBIA_map** is able to identify classes **1. Artificial Territories** and **4. Forests** with higher accuracy than COS.

7.3.2 COSsim

The kappa value of the comparison between COSsim and **OBIA_map** was **0.5860**, considered a moderate agreement, and Table 7.12 presents the percentage of comission and omission errors for each class. Classes **2. Agriculture** and **3. Other Vegetation** had the highest amount of disagreement. As seen in the previous chapter, class **5. Bare and sparsely vegetated areas** had an extremely high percentage of omission errors. **1. Artificial Territories** was the class with the highest agreement.

	Comission Errors (%)	Omission Errors (%)
1. Artificial Territories	18,62	7,22
2. Agriculture	29,24	58,41
3. Other Vegetation	46,86	50,98
4. Forests	37,73	21,44
5. Bare and sparsely vegetated areas	10,73	49,11

Table 7.12: Percentage of **OBIA_map**'s comission and omission errors using COSsim

A detailed comprehensive analysis for each class was produced, with the support of the confusion matrix, presented in Table 7.13.

	True Class				
Predicted Class	1	2	3	4	5
1	34,84	2,29	3,41	0,55	1,72
2	0,58	6,36	1,70	0,15	0,20
3	1,31	5,60	11,79	3,28	0,21
4	0,75	0,98	7,01	14,58	0,09
5	0,07	0,07	0,13	0,00	2,30

Table 7.13: Area-based (in proportion) confusion matrix of **OBIA_map** using COSsim as reference.

7.3.2.1 Artificial Territories

The majority of errors in this class are, in fact true errors, as COSsim is able to delineate small houses and roads much more precisely than **OBIA_map**, likely due to the quality of the segmentation and its minimum area. Figure 7.16 and 7.17 present two of those cases.

Figure 7.16: Classification examples of **OBIA_map**(a) and COSsim with ortophoto background. COSsim is able to detect small houses and roads more precisely than **OBIA_map**

In addition, a substantial portion of errors are due to mismatched edges, which could be due to misalignment of the satellite images, as mentioned in the previous chapter. In addition, like with **PBIA_map**, it appears that **OBIA_map** has a tendency to overestimate

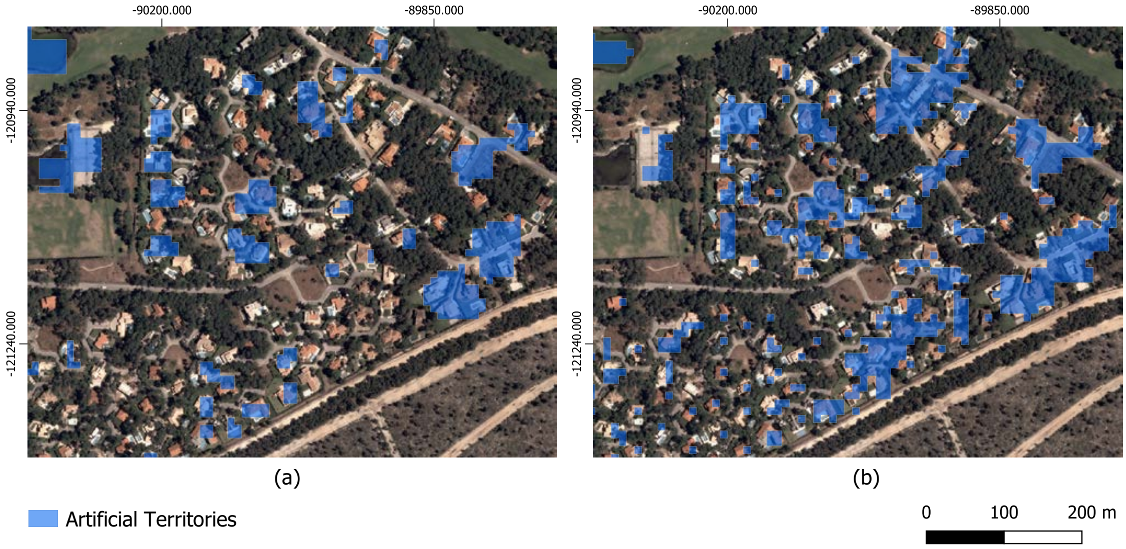

Figure 7.17: Classification examples of **OBIA_map**(a) and COSsim with ortophoto background. COSsim is able to detect the individual houses with higher precision than **OBIA_map**

the edges of this class, while COSsim seems to underestimate them, as can be observed in Figure 7.18

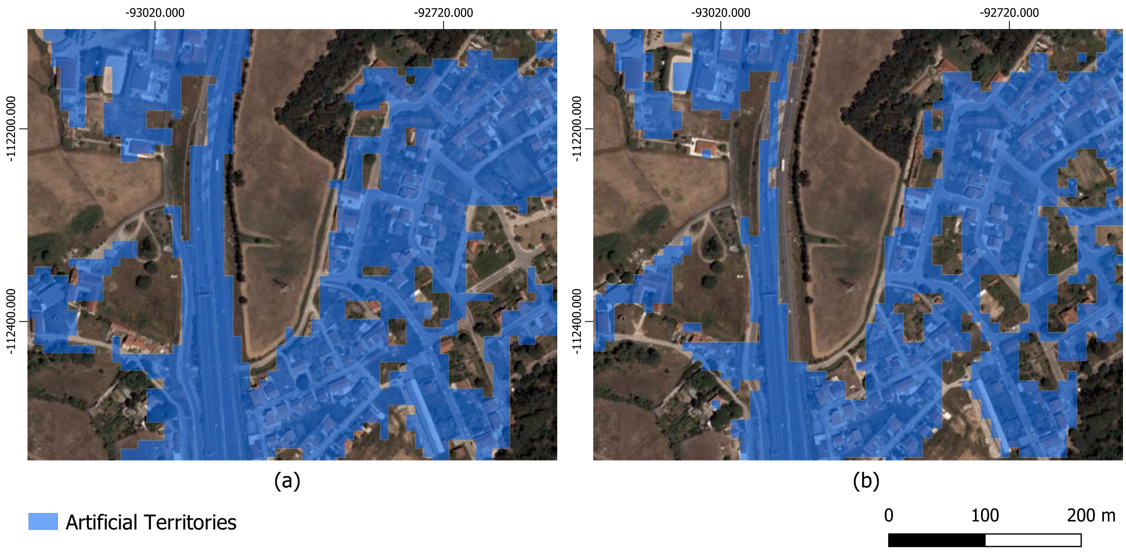

Figure 7.18: Classification examples of **OBIA_map**(a) and COSsim with ortophoto background. **OBIA_map** overestimates the edges of class **1. Artificial Territories**, while COSsim suffers from the opposite problem, and underestimates them.

Nonetheless, not all errors are true, as there are some inaccurate classifications in COSsim, such as in Figure 7.19, where a paved parking lot is classified as **5. Bare and sparsely vegetated areas**. **OBIA_map** is able to correctly classify this area as **1. Artificial Territories**.

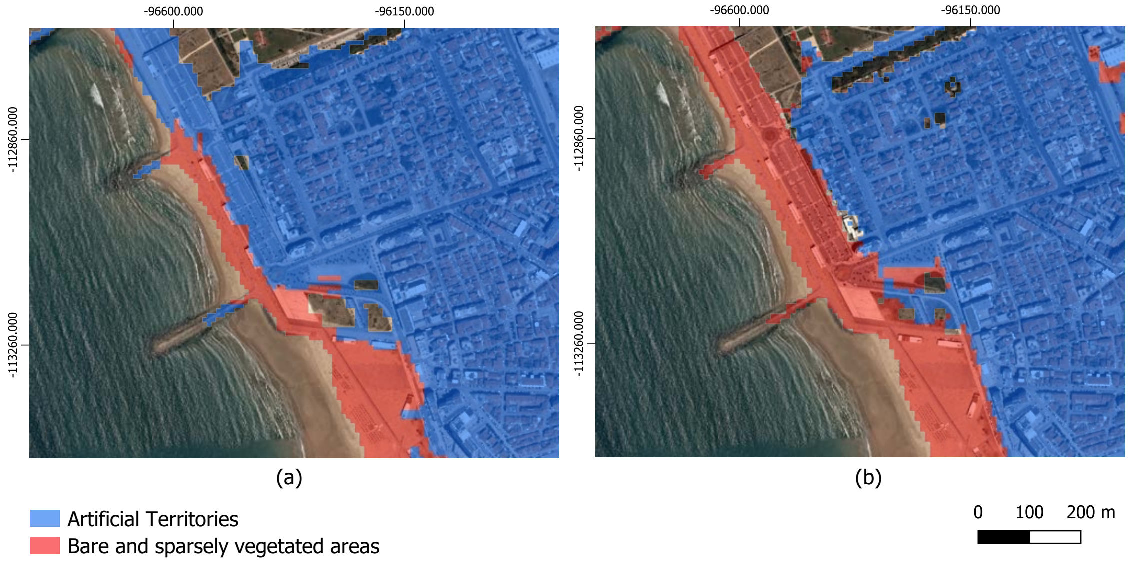

Figure 7.19: Classification examples of **OBIA_map**(a) and COSsim with ortophoto background. **OBIA_map** correctly identifies the parking lot as **1. Artificial Territories**, while COSsim identifies it as **5. Bare and sparsely vegetated areas**.

7.3.2.2 Agriculture

The biggest source of agriculture errors is confusion between this class and **3. Other Vegetation**. Again, it is hard to fully discern which map is correct, although visually COSsim appears to be more accurate.

7.3.2.3 Other Vegetation

A considerable amount of omission errors in class **3. Other Vegetation** occur due to the difference in categorization of the invasive forests, a topic detailed in the previous chapter.

In addition, errors arise from the fact that COSsim distinguishes more precisely between **3. Other Vegetation** and **4. Forests**, an example of which is present in Figure 7.20. Although this could be, again, a segmentation issue, Figure 7.21 shows that the algorithm was able to detect some differences and create multiple segments. Therefore, the problem is likely that the classifier cannot fully separate these classes, especially when the segments are not entirely homogeneous.

7.3.2.4 Forests

Most of the errors in class **4. Forests** seem to be true errors in **OBIA_map** (with exception of the invasive forests area), and are due to poor separation of this class and **Other Vegetation**, as mentioned before.

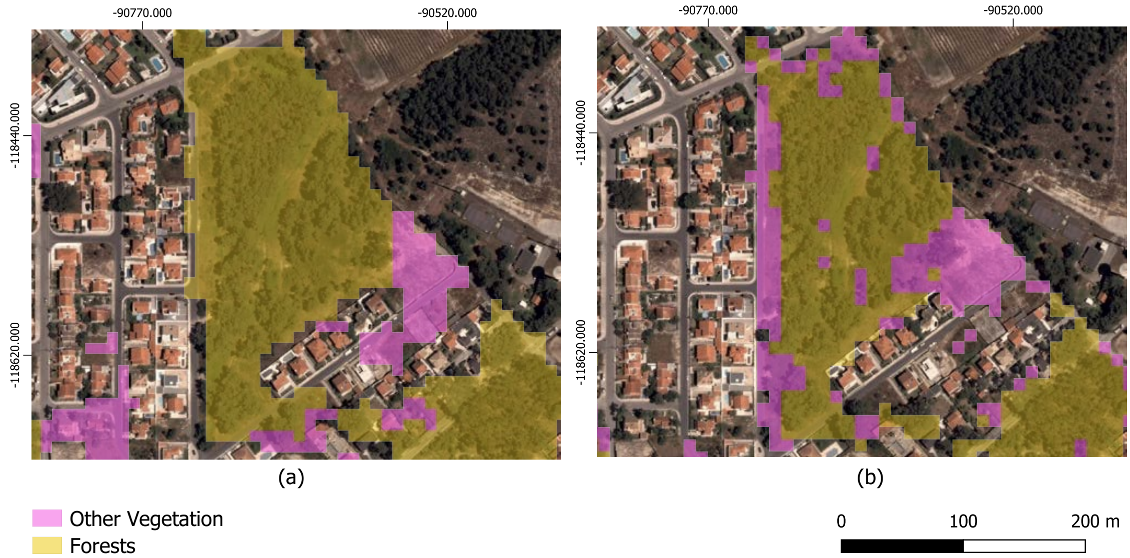

Figure 7.20: Classification examples of **OBIA_map**(a) and COSsim with ortophoto background. COSsim separates classes **3. Other Vegetation** and **4. Forests** with higher accuracy than **OBIA_map**.

Figure 7.21: Segmentation result of the area represented in Figure 7.20. The segments produced are mainly homogeneous, and correctly separate the areas with high density tree coverage and no coverage.

7.3.2.5 Bare and sparsely vegetated areas

As previously detailed, COSsim has some difficulty distinguishing between this class and **1. Artificial Territories**. Therefore, most of the errors in this class occur due better separation of these classes in **OBIA_map**, an example of which is represented in Figure 7.22.

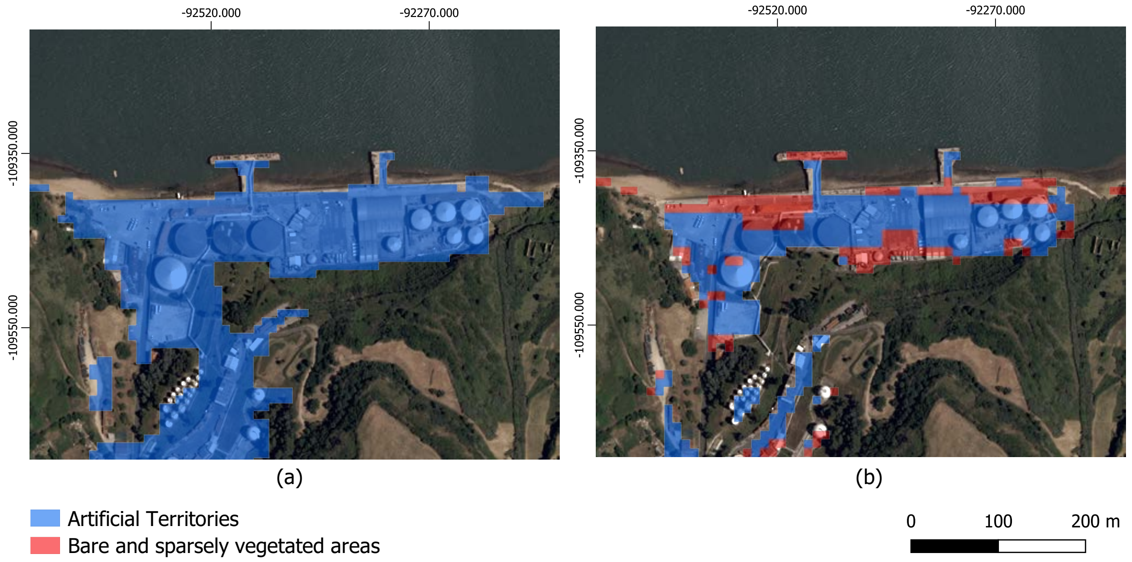

Figure 7.22: Classification examples of **OBIA_map**(a) and COSsim with ortophoto back ground. **OBIA_map** distinguishes classes **1. Artificial Territories** and **5. Bare and sparsely vegetated areas** with higher accuracy than COSsim.

7.3.3 Conclusions

OBIA_map has a similar level of moderate agreement with both COS and COSsim, with the latter being slightly higher.

Although class **1. Artificial Territories** is mostly well classified, with exceptions in areas where the structures are small and isolated. Even with the large amount of disagreement with COSsim, class **5. Bare and sparsely vegetated areas** also appears to be well classified. Classes **2. Agriculture** and **3. Other Vegetation** have the worst performances, mostly due to confusion between each other. Finally, class **4. Forests** has an acceptable performance, with some confusion with **3. Other Vegetation**.

7.4 Conclusions

Segmentation evaluation, specifically in remote sensing is a somewhat subjective topic, and even though OBIA approaches to LULC classification have been steadily increasing in number with extremely good results, it is still under-researched [13].

In consequence, selecting one segmentation as the optimal one proved to be an extremely difficult task. Although the pursued path of calculating homogeneity (WV) and heterogeneity (MI) indices definitely pointed in the right direction, their calculation and combination have some issues, which not only negated the possibility of following a completely automated method, but also made producing a meaningful manual analysis challenging, without resorting to visual inspection. It is clear that a balance between the two indices must be kept, but their relationship needs further investigation and research.

It is important to note that it is not possible to fully claim that the chosen segmentation is the optimal one for this area of study. An informed choice was made based on the analysis produced, but it is highly possible that different parameter combinations could produce a more accurate segmentation.

As for the classification step, XGB had a consistently superior performance, when compared with RF, and the combination of input data **S1+S2+T2** and XGB classifier obtained the best results. The addition of spectral indices generated a decrease in kappa in almost all experiments, while the textural features had mostly a slight positive effect. The inclusion of the 30th and 70th percentile lead to an increase in kappa for all experiments tested, with classes **4. Forests** and **3. Other Vegetation** improving the most. Finally, the incorporation of spatial geometric attributes deteriorated the model's results, probably due to the chosen classes being mostly land-cover classes, which are more closely related to the spectral properties of the objects.

Even though the manual test sets obtained high results, visual analysis of the map produced by the best model, **OBIA_map**, highlighted some issues: segments which are not well classified because they seem to contain multiple LULC classes; and segments which look to be homogeneous but are still not well classified. Although the former is obviously a direct consequence of segmentation quality, the latter is also likely a repercussion of that, due to the methodology chosen to collect the training and test sets. The correct acquiring of these sets lies on the premise of the segmentation being able to create homogeneous segments, as each of them was attributed their dominant class present in the constructed ground truth. If the segment contains a mixture of classes, and is used as a training sample, it will introduce errors in the model. The methodology chosen also lead to the small size of the training set, which possibly contributed to some errors.

The final map, **OBIA_map**, correctly identifies most of classes **1. Artificial Territories** and **5. Bare and sparsely vegetated areas**, but struggles to fully separate **3. Other Vegetation** from **2. Agriculture**, and **3. Other Vegetation** from **4. Forests**.

In conclusion, the application of a OBIA approach to this LULC classification problem was extremely challenging. The final results, although acceptable, are slightly unsatisfactory, especially when compared to the ones obtained in Chapter 6.

8

Conclusions

This chapter presents the final conclusions of this dissertation, highlighting its major findings, accomplishments and limitations of the research, as well referencing some possible future expansions.

8.1 Conclusions

Land Use and Land Cover (LULC) information plays an essential role in urban planning and sustainable city development. In Portugal, and specifically in the Almada municipality, the main LULC map is Carta de Uso e Ocupação do Solo (COS). The information provided by COS, although valuable, has some limitations in spatial and temporal resolution, due to the minimum mapping unit of 1 hectare and the 3 to 5 year release interval. These limitations lead to a map that cannot be used for consistent monitoring of several important spatial planning indices such as proportion of forest land or number of small isolated or illegal structures. As such, this dissertation proposed to study the applicability of satellite data and derived products for creating LULC maps in the region of Almada, with better spatial and temporal resolution.

After the state of the art research, it was decided that a comparative analysis of two common approaches to LULC classification, pixel-based (PBIA) and object-based (OBIA), should be produced. Both of these approaches were tested with several combinations of Sentinel-1, Sentinel-2, spectral indices and textural features, as well as two classifiers, XGB and RF, in order to achieve the best possible results.

In the beginning of this dissertation, it was anticipated that the OBIA methodology would produce better results than PBIA, due to its increasing popularity and excellent performance in other studies. This was not the case, as the segmentation step, a key point in this methodology, was extremely challenging. The lack of established research in unsupervised segmentation evaluation, specifically in remote sensing, lead to a considerable amount of difficulty assessing the quality of the segmentations produced and selecting the optimal one. Although the results of the classification models were high, subsequent visualization of the segments, highlighted misclassifications likely stemming from incorrect segmentation.

In general, the OBIA approach had a more difficult implementation, requiring a significant amount of manual analysis and, for this region of study and set of classes, did not produce the best results. The PBIA approach was considered the most successful in this research problem, as it required a lower amount of manual intervention and produced excellent results.

The experiments performed in both approaches highlighted the superior performance of the XGB in this type of problem, when compared to RF, as well as the benefit of including the 30th and 70th percentiles of the Sentinel-1 and Sentinel-2 bands in the classification features, in addition to the 50th. The addition of textural features also had mostly positive effects on the classification, integrating the best models for both approaches. On the other hand, the introduction of spectral indices lead to a reduction in classification kappa in almost all experiments.

Comparisons of models using the manual and semi-automatic ground truth showed that using COS (even a improved version) to obtain ground truth data, produced an inferior LULC map, with class **1. Artificial Territories** suffering the most deterioration. This is a significant finding, as a considerable amount of studies extract ground truth from existent LULC maps without mentioning any type of uncertainty in the data [22]. Although the lack of an accurate and complete ground truth was a challenge in the development of the dissertation, the manually collected ground truth proved to be extremely effective.

Comparing the final 2018 LULC maps obtained by the best classification models in the PBIA and OBIA experiments, **PBIA_map** and **OBIA_map**, it is clear that, although the agreement between the two maps is high, at around 83.08%, **PBIA_map** has a higher degree of accuracy. **PBIA_map** is able to precisely detect a greater amount of small **1. Artificial Territories**, which **OBIA_map** cannot distinguish. Furthermore, **OBIA_map** struggles slightly more with the identification of **4. Forests**. Despite this, both maps have some limitations in separating **2. Agriculture** and **3. Other Vegetation**.

Overall, the objective of this dissertation was reached successfully, as the PBIA results showed that extremely accurate LULC maps in Almada can be created, verified by visual analysis. Due to its increased spatial resolution, **PBIA_map** is able to distinguish objects which their current LULC map, COS, is not able to, such as small artificial structures and small urban vegetation. Even when compared to a map obtained with similar techniques and with a closer spatial resolution, COSsim, **PBIA_map** seems to perform a better delineation of classes **1. Artificial Territories**, **4. Forests** and **5. Bare and sparsely vegetated areas**. The limitation of this research work in separating **2. Agriculture** and **3. Other Vegetation**, although not ideal, is not especially relevant for the Almada city council, as their primary goal is to monitor urban growth.

8.2 Future work

This research works showed that the creation LULC maps for Almada, through the use of Sentinel-2 and Sentinel-1 and derived products is possible and can produce accurate products. However, future developments can be considered, both in the realm of real life usage, and research.

The work in this dissertation was optimized to produce LULC classification maps for the year 2018. Further work could be developed in order to expand on this research and create an application which the Almada city council could use to produce LULC classification maps with the desired frequency. Although a similar project with high spatial and temporal resolution is being developed by the DGT, COSsim, this map is not optimized specifically for the Almada area. By having an application tailored exactly to their municipality, the city council could have accurate LULC maps, with full control of the temporal frequency.

From a research point of view, there are numerous possible expansions to the work developed in this dissertation. One interesting path would be to study the effects of each feature on the classification, and possibly perform feature selection, to reduce the number of features in the models, and reduce the computational effort. Including more classes, specifically more land-use classes, would also be an interesting development, although in this case, the region of study would need to be increased substantially.

Finally, this dissertation's experiments showed that sampling the reference data available, COS, is not an ideal method of collecting ground truth. However, creating a manual ground truth is not feasible when escalating this approach to a bigger area, and as such, a comprehensive study of the effect of using the automatically extracted ground truth on each class' classification accuracy would be extremely beneficial, as it would help to understand which classes are the most negatively affected. This knowledge could then assist in creating a methodology combining both manual and automatically extracted ground truth, allowing greater areas (and possibly more classes) to be classified.

Bibliography

[1] A. Abdi. "Land cover and land use classification performance of machine learning algorithms in a boreal landscape using Sentinel-2 data". In: *GIScience Remote Sensing* 57 (Aug. 2019), pp. 1–20. DOI: 10.1080/15481603.2019.1650447 (cit. on p. 17).

[2] N. Baghdadi and M. Zribi. *Optical Remote Sensing of Land Surface: Techniques and Methods*. 1st. London/Oxford, GBR: ISTE Press - Elsevier, 2016. ISBN: 1785481029 (cit. on p. 2).

[3] H. Balzter et al. "Mapping CORINE Land Cover from Sentinel-1A SAR and SRTM Digital Elevation Model Data using Random Forests". In: *Remote Sensing* 7.11 (2015), pp. 14876–14898. ISSN: 2072-4292. DOI: 10.3390/rs71114876. URL: https://www.mdpi.com/2072-4292/7/11/14876 (cit. on p. 15).

[4] A. Banskota et al. "Forest Monitoring Using Landsat Time Series Data: A Review". In: *Canadian Journal of Remote Sensing* 40.5 (2014), pp. 362–384. DOI: 10.1080/07038992.2014.987376. eprint: https://doi.org/10.1080/07038992.2014.987376. URL: https://doi.org/10.1080/07038992.2014.987376 (cit. on p. 2).

[5] A. Bekkari et al. "SVM and Haralick Features for Classification of High Resolution Satellite Images from Urban Areas". In: vol. 7340. June 2012, pp. 17–26. ISBN: 978-3-642-31253-3. DOI: 10.1007/978-3-642-31254-0_3 (cit. on p. 21).

[6] A. Bekkari et al. "SVM and Haralick Features for Classification of High Resolution Satellite Images from Urban Areas". In: vol. 7340. June 2012, pp. 17–26. ISBN: 978-3-642-31253-3. DOI: 10.1007/978-3-642-31254-0_3 (cit. on p. 22).

[7] M. Belgiu and L. Drăguţ. "Random forest in remote sensing: A review of applications and future directions". In: *ISPRS Journal of Photogrammetry and Remote Sensing* 114 (2016), pp. 24–31. ISSN: 0924-2716. DOI: https://doi.org/10.1016/j.isprsjprs.2016.01.011. URL: https://www.sciencedirect.com/science/article/pii/S0924271616000265 (cit. on p. 24).

[8] C. M. Bishop. *Pattern Recognition and Machine Learning (Information Science and Statistics)*. Berlin, Heidelberg: Springer-Verlag, 2006. ISBN: 0387310738 (cit. on p. 6).

[9] S. Böck, M. Immitzer, and C. Atzberger. "On the Objectivity of the Objective Function—Problems with Unsupervised Segmentation Evaluation Based on Global Score and a Possible Remedy". In: *Remote Sensing* 9 (July 2017), p. 769. DOI: 10.3390/rs9080769 (cit. on pp. 23, 75).

[10] L. Breiman. "Random forests". In: *Machine learning* 45.1 (2001), pp. 5–32 (cit. on p. 7).

[11] M. Carreira-Perpiñán. "A review of mean-shift algorithms for clustering". In: (Mar. 2015) (cit. on p. 10).

[12] T. Chen and C. Guestrin. "XGBoost: A Scalable Tree Boosting System". In: Aug. 2016, pp. 785–794. DOI: 10.1145/2939672.2939785 (cit. on pp. 8, 21).

[13] Y. Chen et al. "Review on High Spatial Resolution Remote Sensing Image Segmentation Evaluation". In: *Photogrammetric Engineering Remote Sensing* 84 (Oct. 2018), pp. 629–646. DOI: 10.14358/PERS.84.10.629 (cit. on p. 97).

[14] Y. Cheng. "Mean shift, mode seeking, and clustering". In: *IEEE Transactions on Pattern Analysis and Machine Intelligence* 17.8 (1995), pp. 790–799. DOI: 10.1109/34.400568 (cit. on p. 10).

[15] N. Clerici, C. Calderón, and J. Posada. "Fusion of Sentinel-1A and Sentinel-2A data for land cover mapping: a case study in the lower Magdalena region, Colombia". In: *Journal of Maps* 13 (Nov. 2017), pp. 718–726. DOI: 10.1080/17445647.2017.1372316 (cit. on pp. 15, 18).

[16] D. Comaniciu and P. Meer. "Mean shift analysis and applications". In: *Proceedings of the seventh IEEE international conference on computer vision*. Vol. 2. IEEE. 1999, pp. 1197–1203 (cit. on p. 10).

[17] *COSsim 2020 technical specifications*. https://www.dgterritorio.gov.pt/sites/default/files/ficheiros-artigos/SMOS-ET-COSsim.pdf. Accessed: 2022-03-10 (cit. on p. 31).

[18] H. Deng et al. "Ensemble learning for the early prediction of neonatal jaundice with genetic features". In: *BMC Medical Informatics and Decision Making* 21 (Dec. 2021). DOI: 10.1186/s12911-021-01701-9 (cit. on p. 8).

[19] I. Dronova. "Object-Based Image Analysis in Wetland Research: A Review". In: *Remote Sensing* 7.5 (2015), pp. 6380–6413. ISSN: 2072-4292. DOI: 10.3390/rs70506380. URL: https://www.mdpi.com/2072-4292/7/5/6380 (cit. on p. 15).

[20] *Especificações Técnicas da Carta de Uso e Ocupação do Solo (COS) de Portugal Continental para 2018*. http://mapas.dgterritorio.pt/atom-dgt/pdf-cous/COS2018/ET-COS-2018_v1.pdf. Accessed on 2022-02-24 (cit. on p. 3).

[21] G. Espindola et al. “Parameter selection for region-growing image segmentation algorithms using spatial autocorrelation”. In: *International Journal of Remote Sensing - INT J REMOTE SENS* 27 (July 2006), pp. 3035–3040. DOI: 10.1080/01431160600617194 (cit. on pp. 23, 24, 45).

[22] G. M. Foody. “Assessing the accuracy of land cover change with imperfect ground reference data”. In: *Remote Sensing of Environment* 114.10 (2010), pp. 2271–2285. ISSN: 0034-4257. DOI: https://doi.org/10.1016/j.rse.2010.05.003. URL: https://www.sciencedirect.com/science/article/pii/S0034425710001434 (cit. on pp. 72, 100).

[23] P. Fu. “A time series analysis of urbanization induced land use and land cover change and its impact on land surface temperature with Landsat imagery”. In: *Remote Sensing of Environment* 175 (Mar. 2016), pp. 205–214 (cit. on p. 2).

[24] K. Fukunaga and L. D. Hostetler. “The estimation of the gradient of a density function, with applications in pattern recognition”. In: *IEEE Trans. Inf. Theory* 21 (1975), pp. 32–40 (cit. on p. 10).

[25] S. Georganos et al. “Normalization in Unsupervised Segmentation Parameter Optimization: A Solution Based on Local Regression Trend Analysis”. In: *Remote Sensing* 10.2 (2018). ISSN: 2072-4292. DOI: 10.3390/rs10020222. URL: https://www.mdpi.com/2072-4292/10/2/222 (cit. on pp. 23, 75).

[26] S. Georganos et al. “Very High Resolution Object-Based Land Use–Land Cover Urban Classification Using Extreme Gradient Boosting”. In: *IEEE Geoscience and Remote Sensing Letters* 15.4 (2018), pp. 607–611. DOI: 10.1109/LGRS.2018.2803259 (cit. on pp. 21, 24).

[27] P. O. Gislason, J. A. Benediktsson, and J. R. Sveinsson. “Random Forests for land cover classification”. In: *Pattern Recognition Letters* 27.4 (2006). Pattern Recognition in Remote Sensing (PRRS 2004), pp. 294–300. ISSN: 0167-8655. DOI: https://doi.org/10.1016/j.patrec.2005.08.011. URL: https://www.sciencedirect.com/science/article/pii/S0167865505002242 (cit. on p. 7).

[28] D. Goodin, K. Anibas, and M. Bezymennyi. “Mapping land cover and land use from object-based classification: An example from a complex agricultural landscape”. In: *International Journal of Remote Sensing* 36 (Sept. 2015), pp. 4702–4723. DOI: 10.1080/01431161.2015.1088674 (cit. on pp. 15, 18–20, 83).

[29] M. Grandini, E. Bagli, and G. Visani. “Metrics for Multi-Class Classification: an Overview”. In: (Aug. 2020) (cit. on p. 10).

[30] D. Gray, A. Burton-Johnson, and P. Fretwell. “Evidence for a lava lake on Mt. Michael volcano, Saunders Island (South Sandwich Islands) from Landsat, Sentinel-2 and ASTER satellite imagery”. In: *Journal of Volcanology and Geothermal Research* 379 (May 2019). DOI: 10.1016/j.jvolgeores.2019.05.002 (cit. on p. 2).

[31] R. Haralick, K. Shanmugam, and I. Dinstein. "Textural Features for Image Classification". In: *IEEE Trans Syst Man Cybern* SMC-3 (Jan. 1973), pp. 610–621 (cit. on pp. 13, 14, 22).

[32] C. He et al. "Improving the normalized difference built-up index to map urban built-up areas using a semiautomatic segmentation approach". In: *Remote Sensing Letters* 1 (Dec. 2010), pp. 213–221. DOI: 10.1080/01431161.2010.481681 (cit. on p. 12).

[33] H. Hidetake et al. "Evaluating multiple classifier system for the reduction of salt-and-pepper noise in the classification of very-high-resolution satellite images". In: *International Journal of Remote Sensing* 40 (Oct. 2018), pp. 1–16. DOI: 10.1080/01431161.2018.1528400 (cit. on pp. 7, 21).

[34] M. D. Hossain and D. Chen. "Segmentation for Object-Based Image Analysis (OBIA): A review of algorithms and challenges from remote sensing perspective". In: *ISPRS Journal of Photogrammetry and Remote Sensing* 150 (2019), pp. 115–134. ISSN: 0924-2716. DOI: https://doi.org/10.1016/j.isprsjprs.2019.02.009. URL: https://www.sciencedirect.com/science/article/pii/S0924271619300425 (cit. on pp. 10, 22).

[35] C. HUANG, L. DAVIS, and J. Townshend. "An assessment of support vector machines for land cover classié cation". In: *International Journal of Remote Sensing* 23 (Feb. 2002). DOI: 10.1080/01431160110040323 (cit. on p. 15).

[36] J. Jelének, V. Kopackova-Strnadova, and K. Farova. "Post-earthquake landslide distribution assessment using Sentinel-1 and -2 data: example of 2016 Mw 7,8 earthquake in New Zealand". In: vol. 2. Mar. 2018, p. 5174. DOI: 10.3390/ecrs-2-05174 (cit. on p. 2).

[37] Y. Jin et al. "Land-cover mapping using Random Forest classification and incorporating NDVI time-series and texture: a case study of central Shandong". In: *International Journal of Remote Sensing* 39 (Aug. 2018), pp. 1–21. DOI: 10.1080/01431161.2018.1490976 (cit. on p. 13).

[38] B. Johnson and Z. Xie. "Unsupervised image segmentation evaluation and refinement using a multi-scale approach. ISPRS Journal of Photogrammetry and Remote Sensing, 66(4), 473-483". In: *ISPRS Journal of Photogrammetry and Remote Sensing* 66 (July 2011), pp. 473–483. DOI: 10.1016/j.isprsjprs.2011.02.006 (cit. on p. 23).

[39] S. E. Jozdani, B. A. Johnson, and D. Chen. "Comparing Deep Neural Networks, Ensemble Classifiers, and Support Vector Machine Algorithms for Object-Based Urban Land Use/Land Cover Classification". In: *Remote Sensing* 11.14 (2019). ISSN: 2072-4292. DOI: 10.3390/rs11141713. URL: https://www.mdpi.com/2072-4292/11/14/1713 (cit. on p. 25).

[40] H. Kaul and S. Ingle. "Land Use Land Cover Classification and Change Detection Using High Resolution Temporal Satellite Data". In: *The Journal of Environment* 1 (Nov. 2012), pp. 146–152 (cit. on p. 1).

[41] F. J. Kriegler et al. "Preprocessing Transformations and Their Effects on Multispectral Recognition". In: 1969 (cit. on p. 12).

[42] P. Kupidura. "The Comparison of Different Methods of Texture Analysis for Their Efficacy for Land Use Classification in Satellite Imagery". In: *Remote Sensing* 11.10 (2019). ISSN: 2072-4292. DOI: 10.3390/rs11101233. URL: https://www.mdpi.com/2072-4292/11/10/1233 (cit. on pp. 13, 21, 22, 24, 37).

[43] E. Lambin et al. "The causes of land-use and land-cover change: Moving beyond the myths". In: *Global Environmental Change-Human and Policy Dimensions 11 (2001). - ISSN 0959-3780* 11 (Dec. 2001) (cit. on p. 1).

[44] M. Li et al. "A systematic comparison of different object-based classification techniques using high spatial resolution imagery in agricultural environments". In: *International Journal of Applied Earth Observation and Geoinformation* 49 (2016), pp. 87–98. ISSN: 0303-2434. DOI: https://doi.org/10.1016/j.jag.2016.01.011. URL: https://www.sciencedirect.com/science/article/pii/S0303243416300125 (cit. on p. 21).

[45] P. Lourenço et al. "Assessing the performance of different OBIA software approaches for mapping invasive alien plants along roads with remote sensing data". In: *International Journal of Applied Earth Observation and Geoinformation* 95 (2021), p. 102263. ISSN: 0303-2434. DOI: https://doi.org/10.1016/j.jag.2020.102263. URL: https://www.sciencedirect.com/science/article/pii/S0303243420309065 (cit. on p. 10).

[46] L. Ma et al. "A review of supervised object-based land-cover image classification". In: *ISPRS Journal of Photogrammetry and Remote Sensing* 130 (2017), pp. 277–293. ISSN: 0924-2716. DOI: https://doi.org/10.1016/j.isprsjprs.2017.06.001. URL: https://www.sciencedirect.com/science/article/pii/S092427161630661X (cit. on p. 21).

[47] A. Mercier et al. "Evaluation of Sentinel-1 and 2 Time Series for Land Cover Classification of Forest–Agriculture Mosaics in Temperate and Tropical Landscapes". In: *Remote Sensing* 11.8 (2019). ISSN: 2072-4292. DOI: 10.3390/rs11080979. URL: https://www.mdpi.com/2072-4292/11/8/979 (cit. on p. 7).

[48] J. Michel, D. Youssefi, and M. Grizonnet. "Stable Mean-Shift Algorithm and Its Application to the Segmentation of Arbitrarily Large Remote Sensing Images". In: *IEEE Transactions on Geoscience and Remote Sensing* 53.2 (2015), pp. 952–964. DOI: 10.1109/TGRS.2014.2330857 (cit. on p. 11).

[49] A. Neves et al. "Deteção de estruturas permanentes a partir de dados de séries temporais Sentinel 1 e 2". In: Sept. 2019 (cit. on p. 21).

[50] H. T. T. Nguyen et al. "Land Use/Land Cover Mapping Using Multitemporal Sentinel-2 Imagery and Four Classification Methods—A Case Study from Dak Nong, Vietnam". In: *Remote Sensing* 12.9 (2020). ISSN: 2072-4292. DOI: 10.3390/rs12091367. URL: https://www.mdpi.com/2072-4292/12/9/1367 (cit. on p. 16).

[51] K. Nogueira, O. Penatti, and J. dos Santos. "Towards Better Exploiting Convolutional Neural Networks for Remote Sensing Scene Classification". In: *Pattern Recognition* 61 (Feb. 2016). DOI: 10.1016/j.patcog.2016.07.001 (cit. on p. 24).

[52] *Orfeo Toolbox - Feature Extraction*. https://www.orfeo-toolbox.org/CookBook/recipes/featextract.html. Accessed on 2022-03-24 (cit. on p. 38).

[53] F. Pacifici, M. Chini, and W. Emery. "A neural network approach using multi-scale textural metrics from very high-resolution panchromatic imagery for urban land-use classification". In: *Remote Sensing of Environment* 113 (June 2009), pp. 1276–1292. DOI: 10.1016/j.rse.2009.02.014 (cit. on p. 22).

[54] M. Pal. "Random forest classifier for remote sensing classification". In: *International Journal of Remote Sensing* 26.1 (2005), pp. 217–222. DOI: 10.1080/01431160412331269698. eprint: https://doi.org/10.1080/01431160412331269698. URL: https://doi.org/10.1080/01431160412331269698 (cit. on p. 21).

[55] V. Pathak and O. Dikshit. "A new approach for finding an appropriate combination of texture parameters for classification". In: *Geocarto International* 25.4 (2010), pp. 295–313. DOI: 10.1080/10106040903576195. eprint: https://doi.org/10.1080/10106040903576195. URL: https://doi.org/10.1080/10106040903576195 (cit. on p. 22).

[56] T.-N. Phan and M. Kappas. "Comparison of Random Forest, k-Nearest Neighbor, and Support Vector Machine Classifiers for Land Cover Classification Using Sentinel-2 Imagery". In: *Sensors* 18 (Dec. 2017), p. 18. DOI: 10.3390/s18010018 (cit. on p. 17).

[57] D. Phiri and J. Morgenroth. "Developments in Landsat Land Cover Classification Methods: A Review". In: *Remote Sensing* 9.9 (2017). ISSN: 2072-4292. DOI: 10.3390/rs9090967. URL: https://www.mdpi.com/2072-4292/9/9/967 (cit. on pp. 15, 18).

[58] D. Phiri et al. "Sentinel-2 Data for Land Cover/Use Mapping: A Review". In: *Remote Sensing* 12 (July 2020), p. 2291. DOI: 10.3390/rs12142291 (cit. on pp. 1, 2, 6, 15).

[59] D. D. Polsby and R. D. Popper. "The Third Criterion: Compactness as a Procedural Safeguard against Partisan Gerrymandering". In: *Yale Law Policy Review* 9.2 (1991), pp. 301–353. ISSN: 07408048. URL: http://www.jstor.org/stable/40239359 (cit. on p. 46).

[60] S. S. Rwanga, J. M. Ndambuki, et al. "Accuracy assessment of land use/land cover classification using remote sensing and GIS". In: *International Journal of Geosciences* 8.04 (2017), p. 611 (cit. on p. 10).

[61] A. Sánchez-Espinosa and C. Schröder. "Land use and land cover mapping in wetlands one step closer to the ground: Sentinel-2 versus landsat 8". In: *Journal of Environmental Management* 247 (2019), pp. 484–498. ISSN: 0301-4797. DOI: https://doi.org/10.1016/j.jenvman.2019.06.084. URL: https://www.sciencedirect.com/science/article/pii/S0301479719308850 (cit. on p. 6).

[62] A. Sánchez-Espinosa and C. Schröder. "Land use and land cover mapping in wetlands one step closer to the ground: Sentinel-2 versus landsat 8". In: *Journal of environmental management* 247 (Oct. 2019), pp. 484–498. DOI: 10.1016/j.jenvman.2019.06.084 (cit. on p. 19).

[63] M. Sheykhmousa et al. "Support Vector Machine Versus Random Forest for Remote Sensing Image Classification: A Meta-Analysis and Systematic Review". In: *IEEE Journal of Selected Topics in Applied Earth Observations and Remote Sensing* 13 (2020), pp. 6308–6325. DOI: 10.1109/JSTARS.2020.3026724 (cit. on p. 24).

[64] H. Song, Y. Kim, and Y. Kim. "A Patch-Based Light Convolutional Neural Network for Land-Cover Mapping Using Landsat-8 Images". In: *Remote Sensing* 11 (Jan. 2019), p. 114. DOI: 10.3390/rs11020114 (cit. on p. 24).

[65] P. K. Srivastava et al. "Selection of classification techniques for land use/land cover change investigation". In: *Advances in Space Research* 50.9 (2012), pp. 1250–1265. ISSN: 0273-1177. DOI: https://doi.org/10.1016/j.asr.2012.06.032. URL: https://www.sciencedirect.com/science/article/pii/S0273117712004218 (cit. on p. 6).

[66] F. Sun et al. "Efficiency of Extreme Gradient Boosting for Imbalanced Land Cover Classification Using an Extended Margin and Disagreement Performance". In: *ISPRS International Journal of Geo-Information* 8.7 (2019). ISSN: 2220-9964. DOI: 10.3390/ijgi8070315. URL: https://www.mdpi.com/2220-9964/8/7/315 (cit. on pp. 7, 21).

[67] S. Talukdar et al. "Land-Use Land-Cover Classification by Machine Learning Classifiers for Satellite Observations—A Review". In: *Remote Sensing* 12.7 (2020). ISSN: 2072-4292. DOI: 10.3390/rs12071135. URL: https://www.mdpi.com/2072-4292/12/7/1135 (cit. on pp. 10, 15, 21).

[68] A. Tassi and M. Vizzari. "Object-Oriented LULC Classification in Google Earth Engine Combining SNIC, GLCM, and Machine Learning Algorithms". In: *Remote Sensing* 12 (Nov. 2020), p. 3776. DOI: 10.3390/rs12223776 (cit. on p. 21).

[69] P. A. Tavares et al. "Integration of Sentinel-1 and Sentinel-2 for Classification and LULC Mapping in the Urban Area of Belém, Eastern Brazilian Amazon". In: *Sensors* 19.5 (2019). ISSN: 1424-8220. DOI: 10.3390/s19051140. URL: https://www.mdpi.com/1424-8220/19/5/1140 (cit. on pp. 16–18, 24).

[70] H. Thunig et al. "Land use/land cover classification for applied urban planning - The challenge of automation". In: *2011 Joint Urban Remote Sensing Event, JURSE 2011 - Proceedings* (Apr. 2011). DOI: 10.1109/JURSE.2011.5764762 (cit. on p. 1).

[71] K. Van Tricht et al. "Synergistic Use of Radar Sentinel-1 and Optical Sentinel-2 Imagery for Crop Mapping: A Case Study for Belgium". In: *Remote Sensing* 10.10 (2018). ISSN: 2072-4292. DOI: 10.3390/rs10101642. URL: https://www.mdpi.com/2072-4292/10/10/1642 (cit. on p. 17).

[72] O. Varga et al. "Validation of Visually Interpreted Corine Land Cover Classes with Spectral Values of Satellite Images and Machine Learning". In: *Remote Sensing* 13 (Feb. 2021), p. 857. DOI: 10.3390/rs13050857 (cit. on p. 60).

[73] Y. Zha, J. Gao, and S. Ni. "Use of normalized difference built-up index in automatically mapping urban areas from TM imagery". In: *International Journal of Remote Sensing - INT J REMOTE SENS* 24 (Feb. 2003), pp. 583–594. DOI: 10.1080/01431160304987 (cit. on p. 12).

[74] C. Zhang et al. "An object-based convolutional neural network (OCNN) for urban land use classification". In: *Remote Sensing of Environment* 216 (Oct. 2018), pp. 57–70. DOI: 10.1016/j.rse.2018.06.034 (cit. on p. 24).

[75] C. Zhang et al. "Joint Deep Learning for land cover and land use classification". In: *Remote Sensing of Environment* 221 (Feb. 2019), pp. 173–187. DOI: 10.1016/j.rse.2018.11.014 (cit. on p. 16).

[76] H. Zhang, J. Fritts, and S. Goldman. "Image segmentation evaluation: A survey of unsupervised methods". In: *Computer Vision and Image Understanding* 110 (May 2008), pp. 260–280. DOI: 10.1016/j.cviu.2007.08.003 (cit. on pp. 22–24).

A

LULC Maps Produced

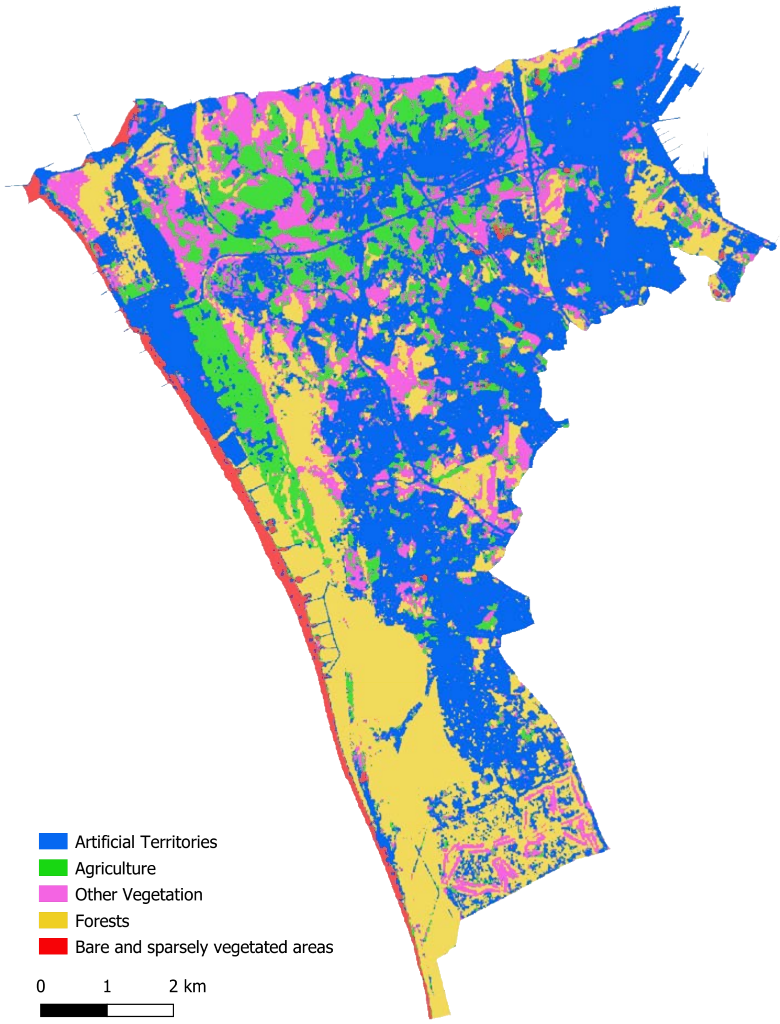

Figure A.1: **PBIA_map**: LULC map created by the best classifier of the PBIA approach.

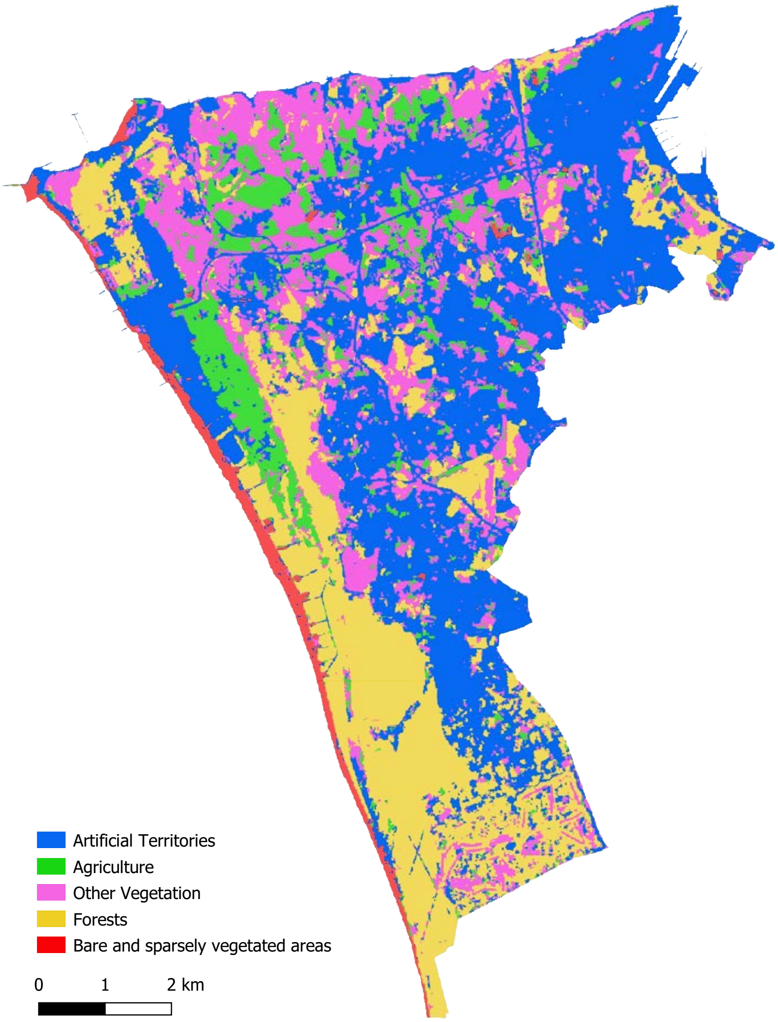

Figure A.2: **OBIA_map**: LULC map created by the best classifier of the OBIA approach.

⟨2022⟩ Inês Oliveira REMOTE SENSING FOR LAND USE/LAND COVER MAPPING IN ALMADA

NOVA SCHOOL OF SCIENCE & TECHNOLOGY